

ABSTRACT

Title of thesis: UNDERSTANDING THE INFLUENCE OF WIND AND SLOPE ON FLAMES IN WILDLAND FIRES

Evan Timothy Sluder, Masters of Science, 2019

Thesis directed by: Professor Michael J. Gollner
Department of Fire Protection Engineering

Wildland fire spread is typically described as a function of fuel, weather, and topography. An understanding of how these parameters are interrelated can help to close the gap on our understanding of the flame spread process. Fire spread over steep slopes is unique because the flame dramatically transitions from a detached, “plume” mode to an attached “boundary layer” mode at what appears to be a critical angle. The change in flame shape significantly increases the rate of spread by increasing the length and magnitude of heating ahead of the burning region. This attachment behavior has been observed in the literature, however the correlation between fire intensity, slope, wind, and flame shape is not yet well described or in a form which allows for prediction of fire behavior.

A series of experiments using stationary gas burners have been undertaken to describe the behavior of a steady flame at multiple slopes under both wind and non-wind conditions. A stationary gas burner has been used to emulate flames under various fire intensities, burner aspect ratios, slopes, and wind conditions. A small-scale apparatus was first used to image hot gases using a shadowgraph tech-

nique coupled with downstream temperature measurements. Later a larger-scale apparatus was used with downstream temperature measurements to determine instantaneous downstream heating lengths. Both steady and time-dependent analysis of the attachment process is presented, along with its relation to fire spread.

Based on the observed trends from these relationships non-dimensional parameters are introduced to relate the effects of inclination, wind, fire size and aspect ratio to the length of the heating region ahead of the burner. It is proposed that this value may be useful as a simple way to incorporate these effects in a wildland fire spread model.

UNDERSTANDING THE INFLUENCE OF WIND AND SLOPE
ON FLAMES IN WILDLAND FIRES

by

Evan Timothy Sluder

Thesis submitted to the Faculty of the Graduate School of the
University of Maryland, College Park in partial fulfillment
of the requirements for the degree of
Masters of Science
2019

Advisory Committee:
Professor Michael J. Gollner, Chair/Advisor
Professor Arnaud C. Trouvé
Dr. Mark A. Finney
Dr. Torben P. Grumstrup

© Copyright by
Evan Timothy Sluder
2019

Acknowledgments

I would like to thank the many people who have helped me in the completion of this thesis. In particular I owe a big thank you to my advisor, Professor Michael Gollner. Thank you for taking me in as an undergraduate and giving me the opportunity to work on countless research projects with many wonderful people who have shaped me as a researcher, and a person. Thank you for your time, advice, and friendship during my time in the Gollner Lab Group.

I would like to thank Dr. Torben Grumstrup who also served as an advisor and mentor during my time at the Rocky Mountain Research Station in Missoula. Without the constant motivation, advice, technical support, and friendship from Dr. Grumstrup this work would have not been possible. It is also important to note that without Dr. Grumstrup's supervision I probably would have been blinded by a friggen laser beam while attempting to take PIV data.

I was also very fortunate to have the opportunity to be advised by Dr. Mark Finney, who's intuition and ingenuity guided this project and led to the design and development of the experimental apparatus in Missoula. His knowledge and curiosity in regards to wildland fire are an inspiration and were crucial to the completion of this work. I am very thankful for all of the thought provoking discussions and recommendations throughout my time in Missoula.

I am very thankful for the diligent work of Michael Heck, a fellow Masters student and friend also completing a masters thesis on fire spread. Mike worked tediously to collect data for this work that was crucial to its completion. Mike

also worked constantly while in Missoula to provide anything I may have needed or forgotten before my return to Maryland.

I was lucky to work with Xingyu Ren who took the time during the early stages of my analysis to assist with data analysis and my MATLAB education. I am also thankful for Xingyu's wonderful company during late nights of work throughout my Masters work.

I am especially grateful for all of the technical support at the Rocky Mountain Research Station. Randy Pryhorocki and Josh Deering for their masterful work in constructing reliable and resilient experimental apparatus. Andrew Gorris, John Bergroos, Chelsea Phillips, and Cyle Wold for their diligent and careful work instrumenting and maintaining each experimental apparatus.

I am extremely grateful for Alison White, whose unwavering encouragement and support throughout the completion of this work made it all possible. I cannot thank you enough for all the time and effort you put into supporting me when I needed it most.

Lastly I would like to thank my parents for their love and support throughout my entire education. Their unwavering encouragement and belief in my abilities throughout my undergraduate and graduate education has motivated me and pushed me far beyond what I originally thought I was capable of. I am far more appreciative of what they have done for me throughout my life than I will ever be able to express.

Table of Contents

List of Tables	vi
List of Figures	vii
List of Abbreviations	xiii
1 Introduction	1
1.1 The Wildland Fire Problem	1
1.2 Modeling Wildland Fire Spread	2
1.3 Inclined Flame Spread	5
1.4 Flames in a Forced Flow	6
1.5 Research Overview	7
2 Literature Review	9
2.1 Flame Spread	9
2.2 Wildland Fire Spread	11
2.2.1 Inclined Flames	12
2.2.2 Wind-Driven Flames	15
3 Experimental Methodology	18
3.1 Overview	18
3.2 Small-Scale Inclined Table	19
3.3 Large-Scale Inclined Table	25
3.4 Thermocouples	28
4 Small-Scale Tilt Table Results	33
4.1 Shadowgraph Images	33
4.2 Small-Scale Tilt Table Temperature Measurements	38
5 Large-Scale Tilt Table Results	45
5.1 Experimental Outline	45
5.1.1 Initial Results: Incline	45
5.1.1.1 Raw Temperature Profile Averages: Incline	47

5.2	Instantaneous Temperature Measurements and Attachment Length . . .	53
5.3	Average Attachment Lengths and PDFs: Incline	57
5.3.1	Initial Results: Forced Flow	61
5.3.1.1	Raw Temperature Profile Averages: Forced Flow . . .	61
5.3.1.2	Instantaneous Attachment Lengths and PDFs: Forced Flow	66
5.3.1.3	Average Attachment Lengths and Correlations: Forced Flow	67
5.3.2	Inclined and Forced Flow	73
5.3.2.1	Raw Temperature Profile Averages: Combination . . .	73
5.3.2.2	Instantaneous Temperature Measurements and PDFs: Combination	75
5.3.3	Average Attachment Length Correlations: Combination	79
6	Conclusions and Future Work	95
6.1	Conclusions	95
6.2	Future Work	97
A.1	Attachment Length PDFs	100
A.2	Small Scale Average Temperature Profiles	106
A.3	Large Scale Average Temperature Profiles: Incline	108
A.4	Large Scale Average Temperature Profiles: Forced Flow	113
A.5	Large Scale Average Temperature Profiles:Inclined and Forced Flow .	116
	Bibliography	120

List of Tables

5.1	Different Test Conditions for each angle of incline	46
-----	---	----

List of Figures

2.1	Flame-spread rates against reported flame spread rate for small scale fires are shown from Gollner et al [25], Pizzo et al. [26], Drysdale and Macmillan [14] and Xie and DesJardin [27]. Figure from [15].	14
3.1	Small scale 9.2 cm \times 50.2 cm perforated propane fueled gas burner mounted in the middle of a 122 cm \times 122 cm ceramic fiberboard surface.	21
3.2	Air cooled LED light source with focus used to create shadowgraph images.	22
3.3	View from perspective of camera collecting shadowgraph images, tilted burner and retroreflective screen	23
3.4	Side view of the large scale sand burner at 6° with only the right-most partitioned section of the burner flowing fuel giving a 50 kW fire . . .	26
3.5	Schematic side view of the large scale sand burner. Not drawn to scale.	27
3.6	View of large scale sand burner as well as hydraulic lift inside wind tunnel oriented at 0° with a forced flow and only the right-most partitioned section of the burner flowing fuel resulting in a 50 kW fire . .	28
3.7	Mounted thermocouples with a bracket and foam padding to prevent air leakage from below.	30
4.1	Image sequence showing inclination of a premixed flame and the resulting attachment (dotted line) with the location of the burner (solid line). Figure by Torben Grumstrup	34
4.2	Shadowgraph image showing a 9.88 kW diffusion flame at 0° with helium inlets downstream	36
4.3	Image sequence of the inclination of a 9.88 kW diffusion flame and the impact on helium inlets downstream.	37
4.4	Average temperature profiles recorded downstream of a 7.6 kW fire from 9.2 \times 50.2 cm burner	40
4.5	Average temperature profiles recorded downstream of a 7.6 kW fire from 9.2 \times 50.2 cm burner	41
4.6	Average temperature profiles recorded downstream of a 7.6 kW fire from 9.2 \times 50.2 cm burner	42

4.7	Average temperature profiles recorded downstream of a 9.88 kW fire from 9.2×50.2 cm burner	43
4.8	Average temperature profiles recorded downstream of a 12.16 kW fire from 9.2×50.2 cm burner	44
5.1	Average temperature profiles recorded downstream of a 76 kW fire from a $15.24 \text{ cm} \times 183 \text{ cm}$ burner	48
5.2	Average temperature Profiles recorded downstream of a 152 kW fire from a $15.24 \text{ cm} \times 183 \text{ cm}$ burner	49
5.3	Average temperature Profiles recorded downstream of a 228 kW fire from a $15.24 \text{ cm} \times 183 \text{ cm}$ burner	50
5.4	Average temperature profiles recorded downstream of 12 fires with varying heat-release rate per unit area on an 18° incline. Legend displays the aspect ratio and the fire heat-release rate for each test.	51
5.5	Instantaneous temperature profiles in 25 Hz incitements vs average temperature profile for a 152 kW fire from a $15.24 \text{ cm} \times 183 \text{ cm}$ burner at a 30° incline	54
5.6	Measured attachment length versus time for a 72 kW fire from a $15.24 \text{ cm} \times 183 \text{ cm}$ burner at 30°	55
5.7	Flame detachment probability versus attachment length for a 72 kW fire from a $15.24 \text{ cm} \times 183 \text{ cm}$ burner at 30° fit with a probability distribution function (PDF).	56
5.8	PDF comparison for a 228 kW fire from a $15.24 \text{ cm} \times 183 \text{ cm}$ burner at 4 inclines	58
5.9	Incline histogram comparison with no forced flow at an 18° incline. Legend displays the aspect ratio and the fire heat-release rate for each test.	59
5.10	$\dot{Q}g \sin(\theta)$ (kW m/s^2) versus mean attachment length (cm) for the inclined table with no forced flow. The legend displays each angle of incline and fire size considered. Each condition contains four different aspect ratios.	60
5.11	152 kW fire from a $30.48 \text{ cm} \times 183 \text{ cm}$ burner with varying forced flow while at the horizontal (0°)	62
5.12	228 kW fire from a $45.72 \text{ cm} \times 183 \text{ cm}$ burner with varying forced flow while at the horizontal (0°)	63
5.13	Temperature profiles for all aspect ratios and heat-release rates under the influence of a 0.304 m/s forced flow. Legend displays the aspect ratio and the fire heat-release rate for each test.	64
5.14	Temperature profiles for all aspect ratios and heat-release rates under the influence of a 0.762 m/s forced flow. Legend displays the aspect ratio and the fire heat-release rate for each test.	65
5.15	PDFs of the attachment lengths for multiple aspect ratios and heat-release rates are shown for a 0.304 m/s wind speed. Legend displays the aspect ratio and the fire heat-release rate for each test.	67

5.16	PDFs at all aspect ratios and fire heat-release rates for a 0.762 m/s velocity. Legend displays the aspect ratio and the fire heat-release rate for each test.	68
5.17	$\dot{Q}u_{measured}$ (kW m/s) versus mean attachment length (cm) for a 0.304 m/s forced flow. The legend displays each fire size considered. Each fire size contains four different aspect ratios.	69
5.18	$\dot{Q}''u_{measured}$ (kW/m ² m/s) versus mean attachment length (cm) for a 0.304 m/s forced flow. The legend displays each fire size considered. Each condition contains four different aspect ratios.	70
5.19	$\dot{Q}u_{measured}$ (kW m/s) versus mean attachment length (cm) for a 0.762 m/s forced flow. The legend displays each fire size considered. Each condition contains four different aspect ratios.	71
5.20	$\dot{Q}''u_{measured}$ (kW/m ² m/s) versus mean attachment length (cm) for a 0.762 m/s forced flow. The legend displays each fire size considered. Each condition contains four different aspect ratios.	72
5.21	Average temperature profiles for a 72 kW fire with a 0.304 m/s forced flow and an aspect ratio of 12	74
5.22	Average temperature profiles for a 152 kW fire with a 0.304 m/s forced flow and an aspect ratio of 12	75
5.23	PDFs of attachment lengths at 12° for all aspect ratios and heat-release rates with a 0.304 m/s forced flow. Legend displays the aspect ratio and the fire heat-release rate for each test.	76
5.24	PDFs of attachment lengths for a 72 kW fire with an aspect ratio of 12 under a 0.304 m/s forced flow	77
5.25	PDFs of attachment lengths for all aspect ratios and fire heat-release rates tested under a 0.304 m/s forced flow. Legend displays the aspect ratio and the fire heat-release rate for each test.	78
5.26	PDF of attachment lengths for a 228 kW fire with an aspect ratio of 12 under a 0.304 m/s forced flow	79
5.27	PDFs of attachment lengths for a 228 kW fire with a burner aspect ratio of 12 under a forced flow of 0.762 m/s.	80
5.28	$\dot{Q}g \sin(\theta)$ (kW m/s ²) versus mean attachment length (cm) for 0.304 m/s forced flow and inclination from 6° to 30°. The legend displays each angle of incline and fire size considered. Each condition contains four different aspect ratios.	81
5.29	$\dot{Q}g \sin(\theta)$ (kW m/s ²) versus mean attachment length (cm) with 0.726 m/s forced flow and inclination from 6° to 30°. The legend displays each angle of incline and fire size considered. Each condition contains four different aspect ratios.	82
5.30	$\dot{Q}u_{measured}$ (kW m/s) versus mean attachment length (cm) for 0.304 m/s forced flow and inclination from 6° to 30°. The legend displays each angle of incline and fire size considered. Each condition contains four different aspect ratios.	83

5.31	$\dot{Q}g \sin(\theta)u_{measured}$ (kW m ² /s ³) versus mean attachment length (cm) for 0.304 m/s forced flow, inclined from 6° to 30°. The legend displays each angle of incline and fire size considered. Each condition contains four different aspect ratios.	84
5.32	$\dot{Q}g \sin(\theta)u_{measured}$ (kW m ² /s ³) versus mean attachment length (cm) for 0.762 m/s forced flow and inclination from 6° to 30°. The legend displays each angle of incline and fire size considered. Each condition contains four different aspect ratios.	85
5.33	$\dot{Q}g \sin(\theta)u_{measured}$ (kW m ² /s ³) versus mean attachment length (cm) for a burner aspect ratio of 12, 0.304 m/s forced flow and inclination from 6° to 30°. The legend displays each angle of incline and fire size considered.	86
5.34	$\dot{Q}g \sin(\theta)u_{measured}$ (kW m ² /s ³) versus mean attachment length (cm) for a burner aspect ratio of 3, 0.304 m/s forced flow and inclination from 6° to 30°. The legend displays each angle of incline and fire size considered.	87
5.35	Re^* versus mean attachment length (m) for 0.304 m/s and 0.762 m/s forced flow with inclinations from 6° to 30°. The legend displays each angle of incline and fire size considered, each condition contains four different aspect ratios.	90
5.36	Re^* versus mean attachment length (m) correlation for 0 m/s, 0.304 m/s and 0.762 m/s forced flow with inclinations from 6° to 30°. The legend displays each angle of incline and fire size considered. Each condition contains four different aspect ratios.	91
5.37	Re^* versus mean attachment length normalized by the length of the leading edge plus the mean attachment length. Correlation for 0 m/s, 0.304 m/s and 0.762 m/s forced flow with inclinations from 6° to 30°. The legend displays each angle of incline and fire size considered, each condition contains four different aspect ratios.	92
5.38	Re^* versus mean attachment length (m) correlation for 0 m/s, 0.304 m/s and 0.762 m/s forced flow with inclinations from 6° to 30°. The legend displays each angle of incline and fire size considered, each condition contains four different aspect ratios.	93
1	45 cm × 183 cm burner (aspect ratio of 4) with a 152 kW fire at 18° and no forced flow	100
2	45 cm × 183 cm burner (aspect ratio of 4) with a 228 kW fire at 24° and no forced flow	101
3	45 cm × 183 cm burner (aspect ratio of 4) with a 72 kW fire at 30° and no forced flow	101
4	15 cm × 183 cm burner (aspect ratio of 12) with a 72 kW fire at 6° and with a 0.304 m/s forced flow	102
5	61 cm × 183 cm burner (aspect ratio of 3) with a 72 kW fire at 6° and with a 0.304 m/s forced flow	102

6	15 cm × 183 cm burner (aspect ratio of 12) with a 152 kW fire at 30° and with a 0.304 m/s forced flow	103
7	15 cm × 183 cm burner (aspect ratio of 12) with a 152 kW fire at 0° and with a 0.762 m/s forced flow	103
8	30 cm × 183 cm burner (aspect ratio of 6) with a 152 kW fire at 0° and with a 0.762 m/s forced flow	104
9	15 cm × 183 cm burner (aspect ratio of 12) with a 152 kW fire at 18° and with a 0.762 m/s forced flow	104
10	61 cm × 183 cm burner (aspect ratio of 3) with a 228 kW fire at 30° and with a 0.762 m/s forced flow	105
11	Average temperature profiles recorded downstream of a 7.6 kW fire from 9.2 × 50.2 cm burner	106
12	Average temperature profiles recorded downstream of a 9.88 kW fire from 9.2 × 50.2 cm burner	107
13	Average temperature profiles recorded downstream of a 12.16 kW fire from 9.2 × 50.2 cm burner	107
14	Average temperature profiles recorded downstream of a 76 kW fire from a 15.24 cm × 183 cm burner	108
15	Average temperature Profiles recorded downstream of a 152 kW fire from a 15.24 cm × 183 cm burner	109
16	Average temperature Profiles recorded downstream of a 228 kW fire from a 15.24 cm × 183 cm burner	109
17	Average temperature profiles recorded downstream of 12 fires with varying heat-release rate per unit area on an 18° incline. Legend displays the aspect ratio, and the fire heat-release rate for each test. .	110
18	Average temperature profiles recorded downstream of 12 fires with varying heat-release rate per unit area on an 24° incline. Legend displays the aspect ratio, and the fire heat-release rate for each test. .	110
19	Average temperature profiles recorded downstream of 12 fires with varying heat-release rate per unit area on an 24° incline. Legend displays the aspect ratio, and the fire heat-release rate for each test. .	111
20	Average temperature profiles recorded downstream of 12 fires with varying heat-release rate per unit area on an 30° incline. Legend displays the aspect ratio, and the fire heat-release rate for each test. .	111
21	Average temperature profiles recorded downstream of 12 fires with varying heat-release rate per unit area on an 30° incline. Legend displays the aspect ratio, and the fire heat-release rate for each test. .	112
22	152 kW fire from a 30.48 cm × 183 cm burner with varying forced flow while at the horizontal (0°)	113
23	228 kW fire from a 45.72 cm × 183 cm burner with varying forced flow while at the horizontal (0°)	114
24	Temperature profiles for all aspect ratios and heat-release rates under the influence of a 0.304 m/s forced flow. Legend displays the aspect ratio, and the fire heat-release rate for each test.	114

25	Temperature profiles for all aspect ratios and heat-release rates under the influence of a 0.762 m/s forced flow. Legend displays the aspect ratio, and the fire heat-release rate for each test.	115
26	Average temperature profiles for a 72 kW fire with a 0.304 m/s forced flow and an aspect ratio of 12	116
27	Average temperature profiles for a 228 kW fire with a 0.304 m/s forced flow and an aspect ratio of 12	117
28	Average temperature profiles for a 72 kW fire with a 0.762 m/s forced flow and an aspect ratio of 12	117
29	Average temperature profiles for a 72 kW fire with a 0.762 m/s forced flow and an aspect ratio of 12	118
30	Average temperature profiles for a 228 kW fire with a 0.762 m/s forced flow and an aspect ratio of 12	118
31	Average temperature profiles for a 228 kW fire with a 0.762 m/s forced flow and an aspect ratio of 12	119

Nomenclature

c_p	Specific Heat (J/kg K)
Fr	Froude Number (-)
g	Acceleration due to gravity (m^2/s)
Gr	Grashof Number (-)
h	Convective Heat Transfer Coefficient (W/m ² K)
k	Thermal Conductivity (W/mK)
L	Length (m)
\dot{Q}''	Heat-Release Rate per Unit Area (kW/m ²)
Q	Heat Release Rate (kW)
Re	Reynolds Number (-)
Ri	Richardson Number (-)
t	Time (s)
T	Temperature (°C)
u	Velocity (m/s)
V	Velocity (m/s)
x	Length (m)

Greek symbols

β	Coefficient of Thermal Expansion
δ	Thickness (m)
Δ	Difference (-)
ρ	Density (kg/m ³)
Θ	Angle (°)
ν	Kinematic viscosity (m ² /s)

Subscripts

0	Initial Value
b	burner
ig	ignition
p	Pynolysis
upstream	Upstream Location of Velocity Measurement
flame or f	Flame
therm	Thermal

Abbreviations

DAQ	Data Acquisition
HRR	Heat-Release Rate
HRRPUA	Heat-Release Rate Per Unit Area
NPT	National Pipe Thread
PIV	Particle Image Velocimetry
SLPM	Standard Litres Per Minute
USFS	United States Forest Service
WUI	Wildland-Urban Interface

Chapter 1: Introduction

1.1 The Wildland Fire Problem

The 2017 and 2018 wildland fire seasons were two of the most devastating on record in the United States. The Forest Service (USFS), California Department of Forest and Fire Protection (Calfire), and other fire fighting agencies struggled to control large and intense fires across the western United States. To give an example, the 2017 fire season saw 12,306 structures destroyed by wildland fire, 8,065 of which were residences [1]. There are a number of reasons why there is an increase in destruction from wildland fire across the western United States and the world. Fire seasons in the United States are on average 78 days longer than they were in the 1970s [2]. Longer fire seasons create a higher probability for hot, dry, windy days which are a recipe for a devastating fire. Despite longer fire seasons the number of wildland fires has decreased or remained constant since 1985; USFS suppression costs have gone from around \$100 million in 1985 to a record \$2.6 billion in 2018, which was more than 50 percent of the USFS annual budget [1]. When the USFS has to spend more than 50 percent of the annual budget on fire suppression alone, management and research efforts fall to the wayside. New techniques in fire manage-

ment and better understanding of wildland fire behavior are crucial for combating increasing fire seasons and larger fires that are the new normal.

1.2 Modeling Wildland Fire Spread

The scale of the wildland fire problem in the United States necessitates the use of technology and tools that can aid in decision making and management. During a wildland fire, fire managers have to determine how to best utilize firefighting resources to preserve life, property, and environmental resources. Models that can predict fire behavior are useful in these scenarios as they are able to give insight into wildland fire spread based on its controlling mechanisms, namely fuel, weather, and topography. While fire modeling has proven useful for wildland fire management, it still faces several challenges. A small time window is available for results to be useful on an active fire. Conditions in the wildland fire environment change very rapidly and require models to provide results in real time. The time sensitivity of a spreading wildland fire necessitates operational models keep computational costs low. Input for these models is also sometimes lacking, with unknowns in fuel and weather conditions adding to uncertainty in predictions.

A lack of understanding related to the physical mechanisms governing wildland fire spread is another challenge that limits the accuracy of modeling in wildland fire. Operational wildland fire models in the U.S. are all empirically based, relying on observations from laboratory and field experiments to predict flame spread rates. Despite the lack of physical understanding in these models, they are still useful

to fire managers. As stated by Finney et al. “An operationally valid model may not correctly describe the process or phenomena; it need only identify a pattern of behavior that is useful in some way.” [41]. Among the existing, more physically-based models, they have been found to lack a common formulation of the physical and chemical processes that influence fire spread [4, 5].

The Rothermel model is an empirical rate of spread model that underlies all U.S. operational fire systems and has proven very useful in fire management, representing current operational modeling capabilities. This model was the first of its kind when published in 1972, describing fire spread in terms of a semi-empirical model for a wide variety of fuels and conditions. Development of the model was primarily based on careful testing of homogeneous, dead fuel beds in a wind tunnel at the USFS Missoula Fire Sciences Laboratory [6]. The different measured spread rates and flame behavior lead to Rothermel developing his equation for wildland fire spread rates. While the Rothermel model was a major advancement at the time, it poses some major limitations due to the assumptions taken in its development. The model is one dimensional, assumes fuels are homogeneous, considers laboratory scale flames, and assumes burning and spread rates are steady state. It is well known that none of these characteristics are true for wildland fires. Wildland fire is a three-dimensional problem, burning through many types of fuel beds at many different scales, and is rarely in a steady state. Despite this the Rothermel model is still used today due to its practicality, the lack of an alternative, and the difficulty in creating a new physically-based flame spread model that is useful in the field. An improved physical understanding of fire is necessary in order to begin to make this

transition. Important phenomena to include in a new physically-based flame spread model would include the ignition of live vs. dead fuels, the influence of changing wind and slope on spread rate, the proportion of convective and radiative heating, and the impact of discrete fuel particles on spread. This study will focus on one of these aspects, the influence of wind and slope on fire behavior and the interaction of flames with the downstream surface.

Development of physical models often requires careful measurements of the phenomena to develop understanding and eventually a theory. Wildland fire, however is a difficult phenomena to measure. Constant variations in weather, wind direction, fuel properties, scale of the fire, and accessibility make taking careful measurements difficult. Attempts to take measurements on active wildland fires often fail due to the misplacement of instrumentation, unexpected fire behavior, or poor timing. Spreading fires have long been studied in the laboratory and do represent some aspects of large-scale fire behavior, however they are still difficult to take detailed measurements on as fires constantly move and require significant effort to set up each time. Alternatively, in this study stationary burners are used to isolate certain flame characteristics by giving a “snapshot” of a spreading fire under various conditions. These stationary fires can be carefully observed and instrumented to allow for the development and understanding of the physical mechanisms that control their behavior [7–13]. This physical understanding can then be validated through measurements collected during instrumented field-scale fires previously discussed.

The transition from the Rothermel model to a new, operational, physically-based flame spread model is well beyond the scope of this study. Measurements and

analysis conducted in this study, however, will aid in this future transition through improved understanding of fundamental fire behavior under different inclinations and wind-driven conditions.

1.3 Inclined Flame Spread

Both the magnitude of the heat flux ahead of a burning region and the distance over which this heat flux is applied are important parameters in determining rates of flame spread. When fires occur over an inclined surface, they tend to angle towards the downstream (higher elevation) surface, increasing both radiative and convective heating of unburned fuels, decreasing the time to ignition. The process by which flames angle or bend over inclined surfaces is therefore of particular interest.

When fires occur on an incline, the geometry between the vertical buoyant motion of hot gases and the angled slope causes an effective ‘blockage’, limiting entrainment on one end of the flame. This causes the flame to bend towards the surface, and eventually ‘attach’ resembling a boundary-layer flow. As the flame approaches the surface it increases heat transfer both due to increased convection, due to the flame’s proximity to the surface, and radiation, due to a favorable view factor between the flame and downstream fuels. The degree to which the flame angle changes is a function of the buoyancy of the fire and the momentum of the wind acting on the fire, effectively generated by this buoyancy and the sloped geometry.

In inclined scenarios, a threshold of attachment has often been observed where entrainment from the inclined side of the fire is effectively completely obstructed,

causing the flame to lay flat on the surface, significantly enhancing convective and radiative heating. Previous studies [14–17], have observed this phenomena in various geometries, sometimes terming it the ‘trench’ effect when sidewalls are installed. While the flame geometry and spread rate has been studied in these configurations, very little is presented in terms of thermal measurements downstream of the flame, which are necessary to more quantitatively model flame spread.

1.4 Flames in a Forced Flow

Similar to inclined surfaces, when fires are acted on by a concurrent flow they tend to angle toward the downstream surface, increasing radiative and convective heating to unburned fuels and decreasing the time to ignition. As in the inclined scenario, the magnitude of heat flux and the distance over which this heat flux is applied are affected by the geometry of the flame and remain important parameters in determining rates of flame spread. The process by which flames angle or bend in a concurrent flow are also of particular interest.

When fires occur on a level surface in a concurrent flow, the momentum of the concurrent flow interacts with the vertical motion of the buoyant plume, pushing it toward the downstream unburned fuels. Flames in a concurrent flow do not have the same “attachment” mechanism that the inclined scenario appears to have, rather a smoother transition is observed in flame behavior as the concurrent flow velocity is increased. As in the inclined scenario, as the flame approaches the surface it increases heat transfer due to increased convection and the flame’s proximity to the

surface. Heat transfer is also increased from radiation, due to a favorable view factor between the flame and downstream fuels. The degree to which the angle changes is a function of the buoyancy of the fire and the momentum of the wind acting on the fire. Differences in the way flames respond to the wind generated in a concurrent flow and by buoyancy in an inclined scenario will be studied here.

1.5 Research Overview

In this study, two separate experimental set ups are used to take qualitative and quantitative measurements downstream of a propane-fueled gas burner array. First, 25 high-frequency thermocouples are used to characterize downstream heating and attachment from a $9.2 \text{ cm} \times 50.2 \text{ cm}$ inclined gas burner. A shadowgraph imaging technique was also used to visualize the behavior of the buoyant plume downstream of the gas burner. Next, a much larger adjustable-size burner is used, up to $61 \times 183 \text{ cm}$, placed within a wind tunnel for combined slope and wind experiments. An array of 60 high-frequency thermocouples are used to characterize downstream heating and attachment of this larger inclined gas burner.

Since most wildland fuels which drive flame spread are very thin, often $< 1 \text{ mm}$ in diameter, fluctuations in convective heating from flames becomes important when describing ignition of fuels [3, 5, 18]. High frequency thermocouples in each experimental set up provide an instantaneous temperature profile down the center line of the flame. These temperature profiles are useful for determining flame location for a variety of heat-release rates, aspect ratios, and incline angles. As the

flame location varies with time it is then plotted as a probability distribution and compared to other tests in order to determine the effect of each varied parameter. Shadowgraph data in the small set ups are also used in order to confirm and compare observations collected using high frequency thermocouples at a larger scale.

Chapter 2: Literature Review

2.1 Flame Spread

Fundamentally, flame spread is the result of sufficient heat input from an existing flame into a solid or liquid fuel, liberating flammable vapors from the fuel surface. These fuel vapors mix with oxidizer from the ambient environment to form a flammable mixture; with sufficient energy input these vapors will then ignite and either self extinguish or begin a feedback loop that results in the fuel surface continually releasing sufficient vapors to sustain this reaction, i.e. flame spread [15]. In most fires, including wildland fires, flames occur as a diffusion flame, where fuel vapors and ambient oxidizer meet in a thin flame sheet to react. The size of the resulting flames are then mostly determined by the rate at which the fuel vapor is emitted from the surface of the fuel, and somewhat by rates of downstream mixing. The fuel diffusion rate is a function of the fuel and the heat flux acting on the surface of the fuel.

The rate of fire spread is then determined by the interaction of forward reaching flames with local unburnt fuel [19]. This interaction occurs when a heat flux is imposed on the unburned fuel, driven by one or more heat-transfer mechanisms.

The spread rate is then defined by the rate at which the combustion or pyrolysis zone moves across a fuel surface [15].

The process of fire spread has been studied experimentally, theoretically, and through the use of numerical models, although the exact fire spread process in wild-land fires is still not fully understood. Fundamentally, flame spread can be described as an energy balance across the fuel front,

$$V_p \rho \Delta h = \dot{q}'' \quad (2.1)$$

where V_p is the flame spread rate, ρ is the density of the fuel bed and Δh is the difference in thermal enthalpy between the burning and unburnt fuel [15,19]. Williams [19] has called this the fundamental equation of fire spread. If steady state and a constant ignition temperature T_{ig} are assumed, and phase changes are neglected this equation can be simplified,

$$V_p = \frac{\dot{q}_f''}{\rho c_p (T_{ig} - T_0)} \quad (2.2)$$

The thermal enthalpy Δh can be represented as the specific heat capacity $c_p \Delta T$, or energy to increase the temperature of a material 1°C multiplied by the difference in temperature for ignition from ambient. Since all variables in the denominator of equation 2.2 are properties of the fuel, it is shown that the heat flux to the unburnt fuel \dot{q}_f'' is one of the most important quantities for determining flame spread [15]. The heat flux to the unburnt fuel is influenced by the geometry of the flame and the ambient conditions, which will later be discussed in more detail.

2.2 Wildland Fire Spread

Wildland fires have gained increased national attention as several recent events have occurred in the western US at a scale and with a destructive force rarely seen in history. These fires have become a challenge to manage with current techniques and technology, highlighting the need for further research. As Finney et al. point out in their review “there is no current verifiable physical theory of flame spread to allow for precise predictions needed to properly manage wildland fire spread” [5]. Without the ability to make reliable predictions of wildland fire behavior, improved management of wildland fire will remain an uphill battle in the United States and elsewhere around the world.

Wildland fire spread often behaves differently than flame spread in the built environment. One important difference is the lack of a continuous fuel surface. Wildland fires are dominated by heat transfer between discrete fuel particles; this process of heat exchange is not completely understood, especially at fuel particle scales [5]. As flame spread can be thought of as a series of ignitions, understanding the physical processes behind the ignition of these fine fuel particles, including the heat transfer that drives this ignition process is important.

Until recently it was mostly assumed that wildland flame spread was dominated by radiative heat transfer [18]. Cohen and Finney proposed that fine wildland fuels can be exposed to high radiant heat fluxes without igniting due to favorable convective cooling. This is significant as radiant heat transfer has received much more attention in the wildland fire research community and models generally assume

a radiative-dominated spread behavior. If convective heat transfer is the driving force behind flame spread in wildland fuels, work must be done to understand and confirm this.

Wildland fire spread is also described as more complex than fire spread in the built environment due to the constantly evolving wildland fire environment. Forest fuels are complex and extremely variable. While fuel variability is not explicitly considered in this study, a focus directly on heating conditions should be translatable in the future to many different fuel configurations. In comparison to fuels and weather, topography is often a more fixed variable to consider in wildland fire. Topography is relatively constant in wildland fire timescales and changes only in space with elevation, steepness of slope, and land features.

Different conditions during a wildland fire may cause rapid flame spread and are of particular interest when it comes to predicting fire behavior. Understanding rapid flame spread anomalies, especially those that occur over short spatial or time scales, can prevent firefighters from being caught off guard while working a fire, and assist in the design of communities, evacuation plans or management strategies, where this type of behavior can be anticipated. Two known anomalies known to cause rapid flame spread are changes in slope and wind.

2.2.1 Inclined Flames

In wildland fire it is known that rapid flame spread up a slope, sometimes called a fire “eruption” can be caused by flame attachment on steep slopes [20–24].

Through experimental methods Moriandini et al. as well as Dold and Zinoviev found that the flow field surrounding the burning region changes as a result of the degree of incline, which would cause the flame to interact with the downstream surface [20,22]. The flame interaction with the downstream surface, or “flame attachment” causes enhanced preheating of the unburned fuels and more rapid flame spread.

Morandini et al. used particle image velocimetry to observe the fluid dynamic effects of a flame spreading up an inclined surface [20]. They found that there is an inversion of the local wind in front of the flame front as incline increases. They also observed the presence of significant convective heating as the incline increases and the flame attaches to the downstream slope [20]. Dold et. al also studied slope as a condition for the “eruptive spread” of wildland fires, or dramatic increase in spread rate and fire behavior. Flow attachment at the vegetation surface and ahead of the fire line was found to increase the spread rate [22].

Flow attachment ahead of the burning region has also been observed and studied in the built environment, most famously the Kings Cross Fire, which gained attention when 31 people perished and 100 more were injured due to rapid flame spread up a “trench” in a London Tube escalator [14]. Drysdale and Macmillian [14] studied this flame attachment in a trench by adding sidewalls and restricting entrainment; it was noticed that flames attach much more readily in this scenario. Figure 2.1 shows the relationship between inclination angle and spread rate from previous small scale studies that omit the use of sidewalls. From this figure it is obvious that inclination angle drastically alters the modes of heating which drives flame spread.

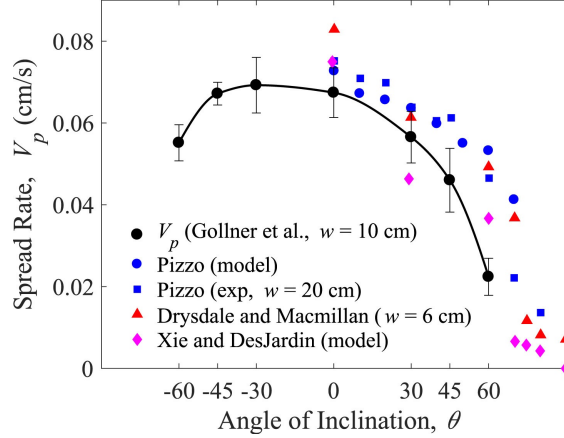


Figure 2.1: Flame-spread rates against reported flame spread rate for small scale fires are shown from Gollner et al [25], Pizzo et al. [26], Drysdale and Macmillan [14] and Xie and DesJardin [27]. Figure from [15].

Gollner et al. [25] investigated the effects of inclination angle on flame spread over a PMMA slab, the results of which are shown in Figure 2.1. It was found that the maximum flame spread rate occurred in a near-vertical orientation, with the increase in flame spread rate attributed to buoyancy-induced flows modifying the heat-flux profiles ahead of the flame front. This is similar to previous results, also shown, by Quintiere, Pizzo, Drysdale and Macmillan and Xie and DesJardin [14, 26, 27, 42]. Fernandez-Pello and Hirano [28] also found that the degree to which hot combustion gases interact with unburnt fuel plays a large role in the rate of flame spread. The rate of spread is then determined by the amount of time unburnt fuel takes to reach its pyrolysis temperature. While extensive research has been done in the vertical orientation under natural entrainment conditions [15, 29–31], less work has been performed on flame behavior at intermediate angles. A thorough

review of flame spread in inclined and forced-flow configurations is also available in Gollner et al. [15].

Mao, Fernandez-Pello, and Pagni completed an analysis for mixed, forced and free convective combustion on a flat fuel surface of arbitrary inclination in order to describe gas flow [32]. Mao et al. introduce a mixed-convection parameter $(Re_x^n + Gr_x^m)^{1/2n}$ in the governing equations describing the mixed, free, and forced combustion of a fuel surface [32]. It is found that with this parameter they are able to provide solutions that are uniformly valid over the entire range of mixed-flow intensities [32].

2.2.2 Wind-Driven Flames

Concurrent flows have an impact on flame spread similar to the inclined scenario. Incoming winds compete with buoyant forces in the plume and either cause the flow to attach to the surface or detach. The major difference between wind-driven flows and the inclined case is that the flow in the wind-driven case is no longer driven by the fire itself. As wind speeds are increased, flames are forced closer to the fuel surface causing preheating of the unburned fuels and more rapid rates of flame spread. In contrast to the inclined scenario, the flame-spread rate increases nearly linearly with increasing flow velocity for smaller-scale flame spread experiments, until blow off extinction starts to occur [15, 33–36]. This is in contrast to the inclined scenario, where flame spread rates increase drastically after a threshold inclination [14].

The impact of wind on flame spread behavior downstream in a wildland fire scenario has been previously studied by Tang et al., who measured downstream heat fluxes of a flame in a concurrent flow [7]. In this study, it was determined that heat fluxes varied significantly downstream under different wind velocities. Low wind velocities showed similar characteristics to flames on low inclines where flames detached and did not interact with the surface [7]. High wind cases showed similarities to steeply inclined flames where the flame is attached to the downstream surface [7]. In this study Tang et al. also related the peak heat flux to the location at which the flame detaches from the surface, where the Richardson number,

$$Ri = g\beta(T_f - T_\infty)x/U^2 \quad (2.3)$$

approached unity. Here, β is the coefficient of thermal expansion, x the downstream distance from the burner and U the ambient wind speed. As the ratio of the Grashof to Reynolds number squared, a unity Richardson number essentially represented a balance between buoyant and forced-convective flows [7]. This transition appeared as an inflection point and was also found to have a linear relationship with the attachment length of the flame, which will be considered in this study.

Other representations of the ratio between wind-driven inertial forces and flame-generated buoyant forces have also been proposed for wildland fires. At the field scale, Byram's Energy Criterion (or Byram's number) has been proposed to relate the flow of kinetic energy in the atmosphere due to the wind field to the rate of conversion of thermal energy to kinetic energy in the convection column [43]. This

ratio is reduced to

$$N_c = \frac{2Ig}{\rho_\infty c_{p,\infty} T_\infty U_\infty^3} \quad (2.4)$$

where I is the fireline intensity (kW/m) and U_∞ represents an average wind speed. Originally this criterion was used to describe fires which “blow up” or tend to be more erratic. Rothermel later used this formulation to define wind-driven scenarios, where $N_c < 1$ [44]. This was also later applied to grass fires [45]. This formulation will be considered later in this study.

Chapter 3: Experimental Methodology

3.1 Overview

The phenomena of flame attachment is well known, but studies have fallen short on explaining the physics that determine when the flame detaches from the surface and attachment length for different flame heat-release rates and shapes under different wind and slope conditions. A series of experiments were conducted in order to investigate this phenomena. Two separate experimental set ups were utilized, investigating flame behavior in a forced flow and inclined scenario. Each experiment utilized a gas-fed propane sand burner which allowed for consistent and repeatable fire conditions, decoupled from changes in burning rate.

The first experiment was a small-scale set up that focused solely on the inclined scenario. This experimental set up was used to collect qualitative images of the flame as well as to record temperature measurements downstream of the flame in order to identify and visualize flame attachment. From this experimental set up a basic understanding of downstream flame and plume behavior as well as heating was obtained. This understanding led to the development of a more sophisticated experimental set up that allowed for more in depth analysis of flame behavior. The second experimental set up was a large-scale inclinable burner that was built

with the intention to systematically investigate more variables influencing the flame. This experimental set up allowed for variation of inclination, burner aspect ratio, concurrent wind speed, heat release rate, and side-air entrainment. Entrainment was varied through the use of ceramic fiberboard sidewalls attached to either side of the tilt table. In this chapter, each of these experimental set ups and the process of data collection will be described in depth.

3.2 Small-Scale Inclined Table

The first inclinable burner was constructed with the intention to study how an inclined surface impacted flame and plume behavior downstream of a burning region. In the design of this experimental set up, a propane gas-fed sand burner was chosen to represent the flame. Sand burners are a common choice in flame spread research because of their consistent and repeatable flame and low experimental cost. Propane was the fuel of choice for these experiments because it is affordable, readily available for many experiments, adaptive for future large scale experiments, and similar in temperature to flames seen outside the laboratory, as diffusion flames all generally have a similar temperature range. Therefore the flame temperatures generated by propane should be similar to those observed in wildland fires. The burner in the small-scale tilt table had an outlet area of $9.2 \text{ cm} \times 50.2 \text{ cm}$, designed with an aspect ratio to roughly represent a spreading line fire.

During troubleshooting it was observed that the sand burner had a fuel flow gradient across the surface that caused an asymmetrical flame downstream. This was

a concern because it would influence temperature measurements down the center line of the flame. In order to prevent this, a porous sheet of sintered metal was added to the sand burner to develop a plenum box which equalized the pressure in the burner before it passed through the sand. Multiple sheets of varying porosity were tested using a U-tube manometer. Once the sheet of metal was added to the burner an even flow was observed.

Different burner dimensions were considered; however, a second experimental set up was constructed with the ability to adjust to different burner sizes so the feature was never implemented on the small-scale set up. The burner was mounted in the center of a 122×122 cm ceramic fiberboard surface on an inclinable table. As stated, the surface of this table was constructed from approximately 2 cm thick pieces of ceramic fiber board so that the surface of the table will not influence the behavior of the flame and will behave like a nearly adiabatic surface. The surface has the ability to tilt up to 45° above the horizontal, with angle resolution at 1° . The completed burner and tilt table are shown in Figure 3.1.

In order to observe the heating of the downstream surface, two separate methods were used to collect qualitative and quantitative measurements of the flame and plume behavior. The first was shadowgraph imaging of the heated gases downstream of the burner surface. A retroreflective shadowgraph set up as described in [37] was used to visualize imaged spacial variation in gas density around the burner as observed from the side. This density variation is caused by variation in temperature which will show the location of the heated plume and the extent of downstream surface being heated [11]. In order to collect shadowgraph images a retroreflective sheet,



Figure 3.1: Small scale $9.2 \text{ cm} \times 50.2 \text{ cm}$ perforated propane fueled gas burner mounted in the middle of a $122 \text{ cm} \times 122 \text{ cm}$ ceramic fiberboard surface.

a camera, an LED light source, and an 80/20 support with a milled camera mount were needed. An approximately $3 \text{ m} \times 3 \text{ m}$ retroreflective screen was mounted flat vertically against a metal frame approximately 12 m away from a Vision Research Phantom V10 high speed camera. An air cooled LED light source was mounted next to the camera and pointed perpendicularly toward the lens shown in Figure 3.2. A clear lens filter was mounted to the front of the camera with a rod mirror angled at 45 degrees mounted in the center. The LED light source beam is focused on the center of the mirror in order to allow for a coincident illumination of the burner, a method developed in [37] to prevent a double shadow in the shadowgraph image. The full shadowgraph set up is shown in Figure 3.3 and includes a camera, a cooled LED, retro-reflective screen, and the burn table. It is important to note



Figure 3.2: Air cooled LED light source with focus used to create shadowgraph images.

in Figure 3.3 the Vision Research Phantom V10 used to collect shadowgraph data is not shown, a different camera was mounted on the set up at this time. During the data collection process it was apparent that the illuminated soot from the flame was visible in the shadowgraph images and prevented some visualization of plume behavior near the flame. In order to more clearly see this behavior an air inlet was added to the burner to create a partially premixed flame in order to better visualize plume behavior. A propane flow rate of 6.6 standard litres per minute and an air flow rate of 57 standard liters per minute [10].

After collecting a series of shadow graph images and video further investigation into the entraining air downstream of the flame was desired. To investigate this flow upstream of the burner tracers were created using four helium jets mounted to the bottom of the inclinable table [10]. These helium jets were visible because



Figure 3.3: View from perspective of camera collecting shadowgraph images, tilted burner and retroreflective screen

the difference in density between the ambient air and helium made them visible on the shadowgraph images. While taking shadow graph images and video, ambient lighting was turned off and high-speed video was taken for 10 to 15 second increments. Ventilation located above the burn table was kept low in order to prevent disturbances in the flame.

With the qualitative understanding given by the shadowgraph images, a quantitative measurement to further the understanding of the visual data was desired. In order to obtain this understanding, gas temperatures were measured downstream of the burner using a linear array of 21 K-type $25 \mu m$ wire diameter thermocouples. The thermocouples were mounted 5 mm above the table surface down the center line of the burner in order to measure heating that fuels would experience in a wildland fire setting. It is known that in wildland fire much of the spread rate is dominated by

fine fuels [18]; these fine fuels are generally found above the surface at intermediate heights. When scaled down to the size of this tilt table, it was determined that 5 mm was a reasonable height. Thermocouples were mounted along the center-line of the downstream surface, as this region would be most characteristic of the flame due to symmetry without influence of edge effects.

Temperature data from the thermocouples was recorded by a National Instruments DAQ system at 500 Hz on each channel [11]. Temperature data was recorded for 90 s at a time to ensure a reliable average of flame location while also recording instantaneous fluctuations in flame location. For each test, the table was inclined from the horizontal and the flame was allowed to normalize for a full minute before the DAQ system began logging temperature measurements. After the system had stopped recording the table was returned to a horizontal position and allowed to cool for a full minute before beginning the next test. This was done to ensure that any residual heat on the table or hysteresis effects did not influence the measurements.

While taking temperature measurements for extended periods of time, ambient fluctuations in the laboratory were found to influence flame behavior, occasionally causing one side of the flame to attach or detach, due to presumably complex flows surrounding the table. Efforts were taken to minimize these ambient flows, including using smoke matches which served as flow tracers to visualize ambient flows before experiments. The variable speed ventilation fan used to exhaust combustion products was also kept on the lowest setting during testing to prevent unnecessary disturbances. These steps were standard procedure for both shadowgraph and temperature data.

3.3 Large-Scale Inclined Table

As in the small-scale experimental set up, a propane fed sand burner is mounted flush between two nearly adiabatic inclinable surfaces and is instrumented with a linear array of thermocouples down the center line. To expand the capabilities of the first experimental set up the scale of the experiment is increased and the experiment is designed to observe how different characteristics of the burning region and the ambient environment alter flame behavior.

The size of the sand burner was increased to a total outlet area of $61 \text{ cm} \times 183 \text{ cm}$, which is partitioned into four equal $15.25 \text{ cm} \times 183 \text{ cm}$ sections. These sections give the capability of four different burner sizes with different aspect ratios. This allows the variation of not only aspect ratio of the burning region, but also the heat-release rate per unit area for uniform flow rates. The burner is partitioned perpendicular to the stream-wise direction giving burning regions that emulate line fires, these partitions are shown in Figures 3.5 and 3.6. To flow fuel from each burner individually each section was fitted with a separately fed fuel supply. An OMEGA FMA-2612A mass flow controller was used to create flow rates of propane from 0 to 200 standard litres per minute (slpm). Due to the size of the fires and high flow rates of propane, an approximately 90 liter propane cylinder was used. Originally, high flow rates of propane cooled the propane tank to a point that tank pressure became too low to maintain desired flow rates. The Wrap-It-Heat Model TRX-16 electric heater was later implemented to prevent tank pressure drop due to cooling.



Figure 3.4: Side view of the large scale sand burner at 6° with only the right-most partitioned section of the burner flowing fuel giving a 50 kW fire

From the mass flow controller, the flow is partitioned into each burner. Four ball valves are used to vary the flow to each section of the burner. Approximately 1.27 cm NPT pipe with 0.1 cm diameter holes drilled every 2.5 cm is mounted at the bottom of each section of the sand burner, 15 cm on center. Each pipe is buried below 15 cm of sand in order to allow for the diffusion of fuel throughout the entire burner area. In order to disperse the flow and prevent sand from clogging the piping, the drilled holes are pointed down and the piping is sheathed in woven fiberglass.

Due to the size and weight of the burner, inclination of the tilt table was challenging. A hydraulic lift was attached to the downstream side of the table and was manually pumped in order to increase the angle of the burner. The length of the set up limited the angle of incline to 30° above the horizontal, this was determined acceptable as the flame was fully attached before 30° in each scenario.

The surface of the inclined table, as previously described, is made from a nearly adiabatic ceramic insulation material, one 61 cm × 183 cm piece is placed upstream of the burner while two 122 cm × 91.5 cm pieces are pushed together on the downstream side of the burner. Two separate pieces of insulation are used on the downstream side to allow for thermocouples to be mounted down the center line of the downstream side between the two pieces. The burner surface was completed by the addition of a 76 cm × 183 cm metal sheet mounted on the front of the table to assist in the development of the boundary layer upstream of the burner, shown in Figure 3.5. These surfaces combined to form the 320 cm × 183 cm inclinable surface

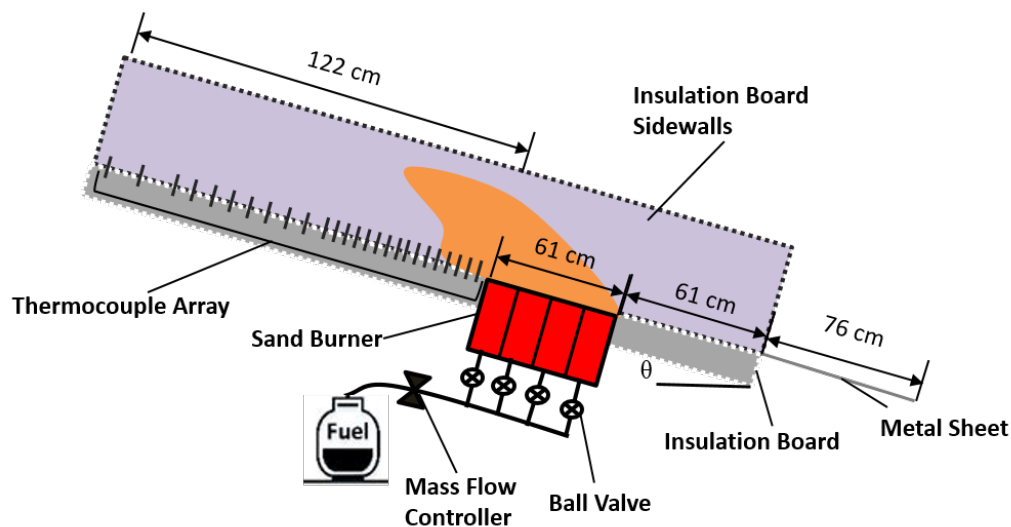


Figure 3.5: Schematic side view of the large scale sand burner. Not drawn to scale.

that was then placed inside the 3 m × 3 m laminar flow wind tunnel located at the U.S. Forest Service, Missoula Fire Science Laboratory in Missoula, Montana. The wind tunnel is capable of wind speeds up to 3.6 m/s, with humidity and temperature control. Wind speeds utilized in this study varied from 0 – 0.762 m/s. Figure 3.5

shows a view of the inclined burner in use inside the wind tunnel under the influence of a forced flow.



Figure 3.6: View of large scale sand burner as well as hydraulic lift inside wind tunnel oriented at 0° with a forced flow and only the right-most partitioned section of the burner flowing fuel resulting in a 50 kW fire

3.4 Thermocouples

Thermocouples used along the downstream surface were created by welding 50 μm K-type thermocouple wire with a thermocouple bead welded in the center between two thicker-gauged thermocouple wires. This worked effectively for preserving the finer thermocouple wire, but posed issues in consistent temperature measurements. When thermocouples were welded, the small gauge wire tended to bow either up or down between the thicker gauge wire. This bow in the wire amounted to a 2 - 4 mm height difference between thermocouples, which sometimes caused a signif-

ificant difference in temperature readings. To prevent this, each thermocouple was carefully made and adjusted so that heights were relatively uniform.

Video measurements of the flame and flame attachment lengths were not possible in this experimental apparatus. Due to the size and length of the flames, structural members of the tunnel prevented a full uninterrupted image of the flame. Video of flame length may be possible in the future with careful measurements of the position of the burner in relation to the structural members of the tunnel. A track to mount a camera above the tilt table was mounted to the ceiling of the wind tunnel with the intention of taking high speed video from above the flame, although these tests were not completed.

Numerous issues were encountered with the fine-gauge thermocouples that had to be overcome. Examination of the thermocouples after high flow-rate tests revealed significant soot build up within the first 10 cm after the burner's downstream edge. Soot build up affects both the absolute and time accuracy of temperature measurements. In order to remove the soot from thermocouples, attempts were made to manually remove soot using butane torches and hand tools but were unsuccessful. Instead, installation of an air inlet to the gas burner, similar to the one on the small-scale tilt table allowed for a partially premixed flame to heat and effectively clean soot off the thermocouples directly downstream of the burner. This was used to consistently clean thermocouples after consecutive high flow rate tests. Another issue encountered involved ambient air entraining through mounted thermocouples at the bottom of the bed. In high fuel flow rate cases, air was entering a fuel rich environment from the thermocouple mount penetrating the burn bed surface, re-

acting with available fuel, and causing an increase in temperature. In low flow rate cases a fuel lean environment resulted in cooling of the thermocouples. In order to prevent the leakage of air through the bottom of the bed a two part solution was necessary. It was found that the fires were so large, and burning for so long, that the insulation board used for the table surface was warping under the heat. In order to fix this the insulation surface was doubled in thickness from 1.27 cm 2.54 cm. It was also noticed that holes that had been made in the insulation for thermocouples were deteriorating at the edges. In order to prevent this from happening with the new table surface, metal brackets were added with foam insulation in order to eliminate the need to manipulate the insulation. Figure 3.7 shows thermocouples mounted after the alterations.

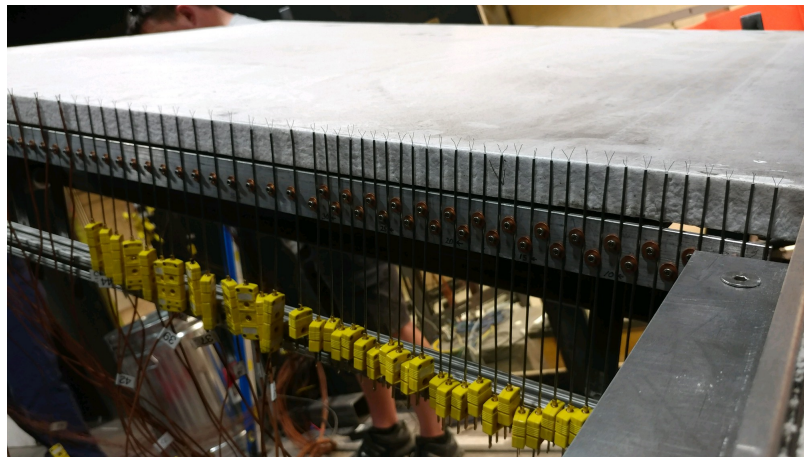


Figure 3.7: Mounted thermocouples with a bracket and foam padding to prevent air leakage from below.

Thermocouples were ultimately used in order to determine the location of the flame for both time-averaged and instantaneous temperature profiles, therefore the response capabilities of the thermocouples was considered. Downstream heating was

not evaluated in this study, therefore radiation corrections are not used throughout the study. If necessary, these could be conducted in the future.

As time-dependent measurements are important, the time-response of the thermocouples is critical. The manufacturer (Omega) suggests the exposed 50 *m* thermocouple has a response time of 0.02 s [38]. The response time of a thermocouples is defined as the time required to reach 63.2% of an instantaneous temperature change. Thermocouple measurements were initially recorded at a rate of 500 Hz, however during data analysis the sampling frequency was stepped down to 100 Hz. While the thermocouples do not respond at this higher frequency, capturing a higher sampling rate is used in order to avoid losing any signal and to capture flame behavior occurring on shorter timescales.

In order to ensure that the rate at which samples were recorded is reasonable for flame location measurements, movements of the flame are evaluated using a MATLAB script developed to detect the location where the flame detaches from the surface, described in more detail in Chapter 6. As the location of where the flame detaches is tracked down the length of the bed, flame structures can be tracked down the array of thermocouples mounted near the surface of the insulation board. Through manual tracking of these flame structures, flame pulsations are seen to fluctuate downstream at a frequency between 1.3 and 5 Hz over the various inclinations and forced flow wind speeds tested in this study.

Previously, Finney et al. observed a fluctuating flame presence using an alternating temperature signal with temperatures varying from ambient to nearly 1200°C, the average frequency of fluctuations was determined using a level crossing

of 350°C [3]. Frequencies of temperature fluctuations are between 1 and 8 Hz, which are on the same scale as the frequencies observed in this study [3]. These frequencies indicate that the 50m thermocouples used are more than capable of recording these flame location fluctuations.

In order to determine what error may be expected in determining the location of the flame due to the transit time of the flame pulsations, the expected velocity of the flame is calculated. In order to estimate the velocity v_{therm} at which heated gases will propagate down the array of thermocouples, a known velocity $u_{measured}$ in the wind tunnel is taken and then multiplied to account for the increase in speed due to thermal expansion from heating by the fire. The maximum tested wind speed (1.26 m/s) is multiplied by the estimated change in temperature in the flame divided by the ambient temperature in the tunnel,

$$v_{therm} = \frac{\Delta T}{T} u_{measured} \quad (3.1)$$

The difference in temperature, ΔT is considered to be 600°C as the flame will propagate through the burning region but will go through multiple temperature gradients as it goes down the burn bed, meaning the temperature change will not be from ambient to flame temperature at the thermocouples. Ambient temperatures in the wind tunnel are known to be around 25°C. A velocity of 2.52 m/s is determined to be an expected maximum velocity of the heated flow in the tunnel. If the response time on each thermocouple is considered to be 0.02 seconds, the flow will have moved 5 cm in this time. Therefore the estimates of location are assumed to have a maximum possible error of $\pm 5cm$, or about 13% of the length of the tested region.

Chapter 4: Small-Scale Tilt Table Results

4.1 Shadowgraph Images

As mentioned in Chapter 3, a retroreflective shadowgraph technique was used to visualize heated gases downstream of the propane burner at angles of 0° , 10° , 20° , and 30° in order to gain insight on plume attachment and downstream heating. A sequence of images taken at these angles of inclination are shown in Figure 4.1. The inclination of the surface was shown to have a dramatic effect on plume behavior. As explained in [10] shadowgraph “images” or shadowgrams show a composite average of the plume through it’s total width. Despite the fact that this overall average will include portions of the flame experiencing edge effects, the width of the burner will ensure that the majority of the phenomena shown in the shadowgrams will come from flame without of the influence of the edge effects [10]. In Figure 4.1 the plumes’ interaction with the downstream surface is visible. In order to view the interaction of the plume with the downstream surface, the burner is marked with a solid white line, and the length of the table in contact with the plume is marked with a dotted white line in Figure 4.1.

Plume or flame “attachment” can be defined as the length at which the plume or flame interacts with the downstream surface. In Figure 4.1 the “attachment” is

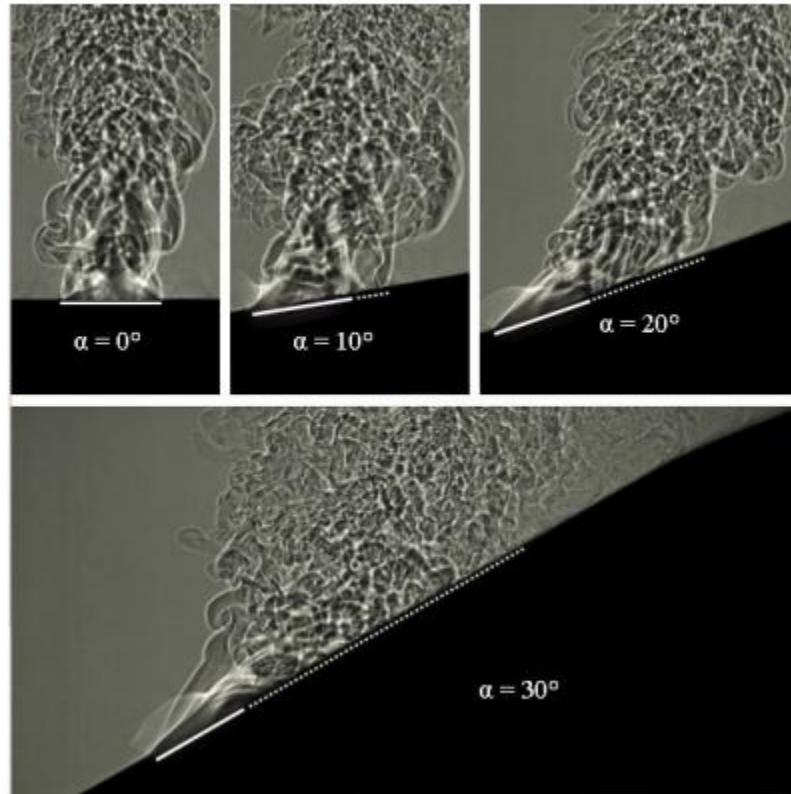


Figure 4.1: Image sequence showing inclination of a premixed flame and the resulting attachment (dotted line) with the location of the burner (solid line). Figure by Torben Grumstrup

shown with the dotted white line. Starting from the horizontal (0°) case, the plume rises vertically above the burner and has no interaction with the surface. When the angle is increased from 10° to 20° , the plume begins to lean to the up slope side of the table. When the plume leans to the up slope side it also begins to interact with the inclined surface. For the 10° case shown in Figure 4.1, the plume attaches to the surface downstream of the burner for a few cm before detaching. In the 20° case the plume stays attached to the surface downstream of the burner for almost three times as long before then also detaching from the surface. The length for which the

plume is attached to the surface before detaching is the previously mentioned “attachment length”. The “attachment length” gives insight on downstream heating, as the presence of the flame generated plume near the surface denotes high amounts of heating. The 30° case shows a third scenario which is essentially complete attachment to the downstream surface, although there is a detachment point of the plume, there are still heated gases visible downstream of the indicated detachment point, which was not visible in the past two inclines.

Aside from its interaction with the surface, a change in plume behavior is also noted as the angle of inclination is increased in Figure 4.1. As the angle increases from 0° to 20° the plume can be seen angling toward the inclined surface. This angling of the plume or “plume tilt” may be the result of a difference in entrainment between the uphill and downhill sides of the flame [10]. In the 0° case the plume is vertically oriented and is experiencing equal entrainment from each side of the flame [20]. Since a vertical plume is a result of uniform symmetric entrainment, it makes sense that plume tilt would be a result of asymmetric entrainment for either sides of the flame [10]. This asymmetry has been previously observed in both laboratory and field experiments [10, 14, 20, 22]. As the angle of incline is increased, the proximity of the vertical plume to the uphill surface shrinks, leaving less room for entrainment from the uphill side. As the entrainment from the uphill side is limited, increased entrainment to sustain combustion occurs from the downhill side of the flame. This feedback loop will eventually cause complete attachment to the uphill surface as a result of the buoyant plume and the momentum from the entrainment on the downhill side of the flame.

In order to investigate plume behavior and the influence of entrainment on the uphill side of the plume, four helium inlets were introduced into the downstream (uphill) side of the burning region to act as tracers in the shadowgrams. Helium was able to be used as a tracer in shadowgrams due to its low density ($0.179\text{kg}/\text{m}^3$) in comparison to ambient air ($1.225\text{kg}/\text{m}^3$). These inlets are shown in Figure 4.2 with the table at the horizontal or a 0° case. The inlets are located at 16.3, 26.5, 36.7, and 46.8 cm downstream of the burner.

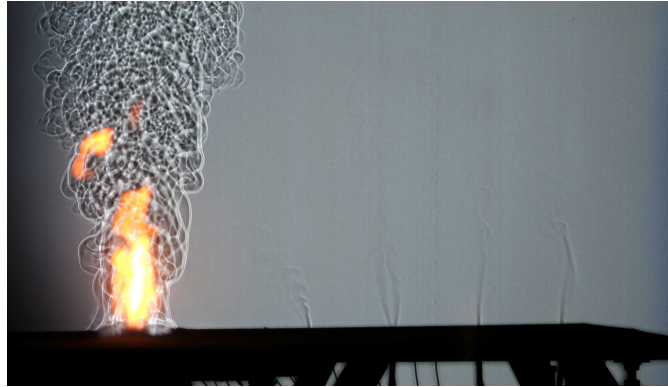


Figure 4.2: Shadowgraph image showing a 9.88 kW diffusion flame at 0° with helium inlets downstream

Figure 4.2 shows that the three right most inlets are not impacted by flows caused by entrainment to the fire at this distance; although the helium inlet closest to the flame at 16.3 cm shows a slight bend toward the flame indicating entrainment at this distance. The inclinable surface was tilted from the horizontal at 5° increments in order to observe flow interaction with each helium inlet as the plume began to interact with the surface and cause attachment. Figure 4.3 shows different inclines

from 5° to 30° , the distinguishable helium flows are traced in a dotted white line to make their direction more obvious.

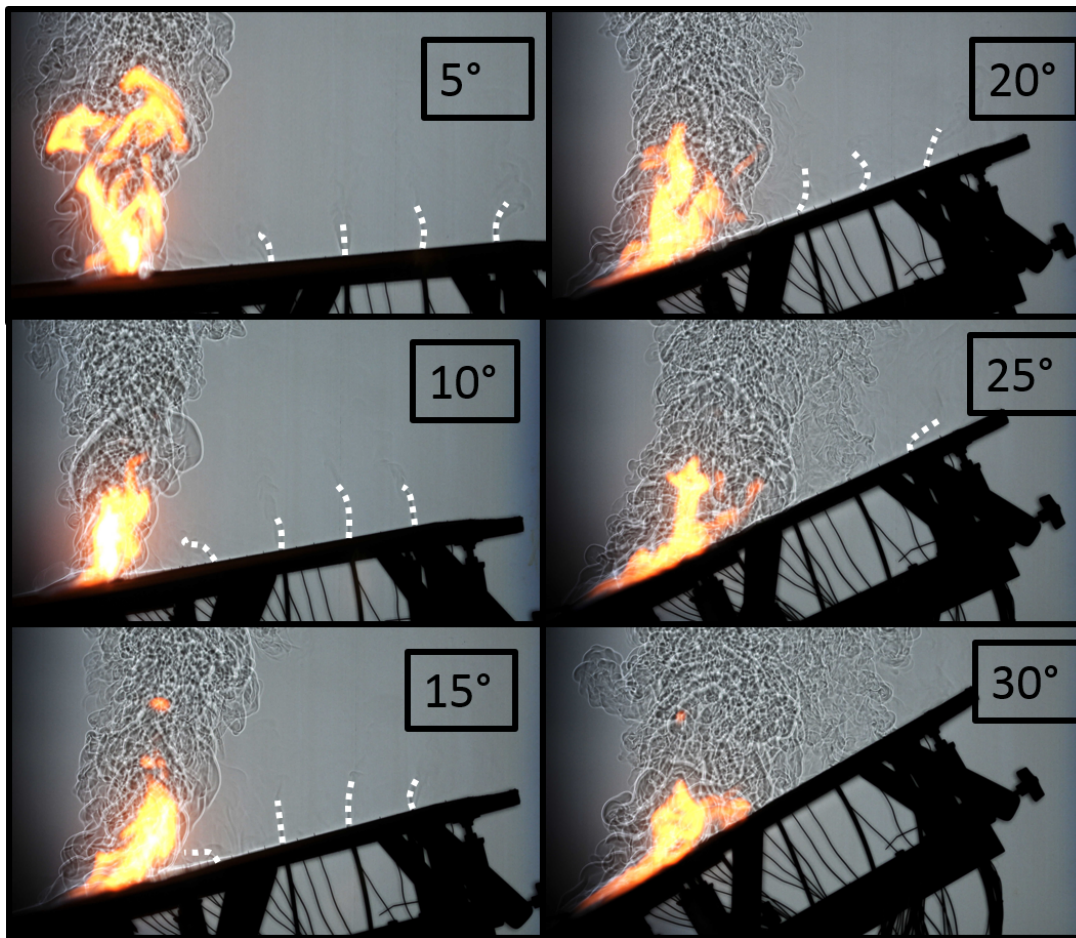


Figure 4.3: Image sequence of the inclination of a 9.88 kW diffusion flame and the impact on helium inlets downstream.

The helium flows in Figure 4.3 shed some light on the dynamics surrounding the heated plume despite being very simple observations. In the 5° , 10° and 15° cases, the closest helium inlet at 16.3 cm can be seen bent toward the flame indicating local entrainment to the flame; the inlets further away are still almost completely vertical in these three cases. Although between the 10° and 15° cases there is a subtle

change in bend toward the flame, to away from the flame in the three right most helium inlets. The 20° case shows different behavior of the inlets when significant flame attachment has occurred. The first inlet at 16.3 cm is no longer visible but the other inlets are shown bending away from the flame. In this case it seems that the local entrainment has been overcome by the buoyant plume, preventing entrainment flow near the surface on the downstream side. In the 25° case this behavior continues with only the 46.8 cm helium inlet visible, bent almost at a 90° angle away from the flame. In the 30° case the plume is completely attached to the surface and none of the inlets are visible. Above the 15° case it is apparent that near the surface of the bed downstream there is no entrainment.

4.2 Small-Scale Tilt Table Temperature Measurements

Tests were conducted on the small tilt table after the shadowgraph images to measure temperature downstream of the burning region between 12° and 30° to investigate the observed plume behavior in shadowgrams. Temperature measurements were not taken while recording shadowgrams, ambient conditions could be slightly varied between results. In order to closely observe the behavior of the flame and plume, the angle of incline was increased from 12° to 28° in 1° or 2° increments while recording temperature data. These angles were chosen because in shadowgrams and previous studies [12,39], threshold flame attachment often occurs between these angles of incline. As well as incline, fuel flow rates were varied; 5.1, 6.5, and 8 standard litres per minute of propane were used to view the impact of heat release rate on the

downstream temperatures. These flow rates would generate fires with heat-release rates of 7.6, 9.88, and 12.16 kW respectively. It is anticipated that large fire sizes will cause higher downstream temperatures, and may cause flame attachment at lower degrees of incline.

During experiments the inclinable table would be initially horizontal at 0° while the fire heat-release rate was adjusted. Once a steady flame was developed the table was tilted to the desired incline and allowed to normalize for 60 seconds. Once the flame had reached a steady state, temperature measurements were recorded for 90 seconds. The lowest heat-release rate of 7.6 kW is shown in Figure 4.4. Each temperature profile and degree of incline is a separate test. To avoid influence between tests, the surface of the table and thermocouples were allowed to cool between tests. From the 7.6 kW test a noticeable transition in downstream temperature occurs between 16° and 18° . Recorded temperatures rise from around 300°C to above 800°C for the surface directly downstream of the burner. Temperatures at 18° and above then follow a similar trend until about 10 cm when higher inclines have a slower temperature decay.

Recorded temperatures rise from around 300°C to above 800°C for the surface directly downstream of the burner. Temperatures at 18° and above then follow a similar trend until about 10 cm when higher inclines have a slower temperature decay. It was found that the temperature decay is more visible on a log-log scale. Figure 4.5 shows the temperature profiles for this test on a log-log scale.

The log-log scale clearly shows the difference between flames that are attached and detached from the surface. It also highlights where temperatures begin to drop

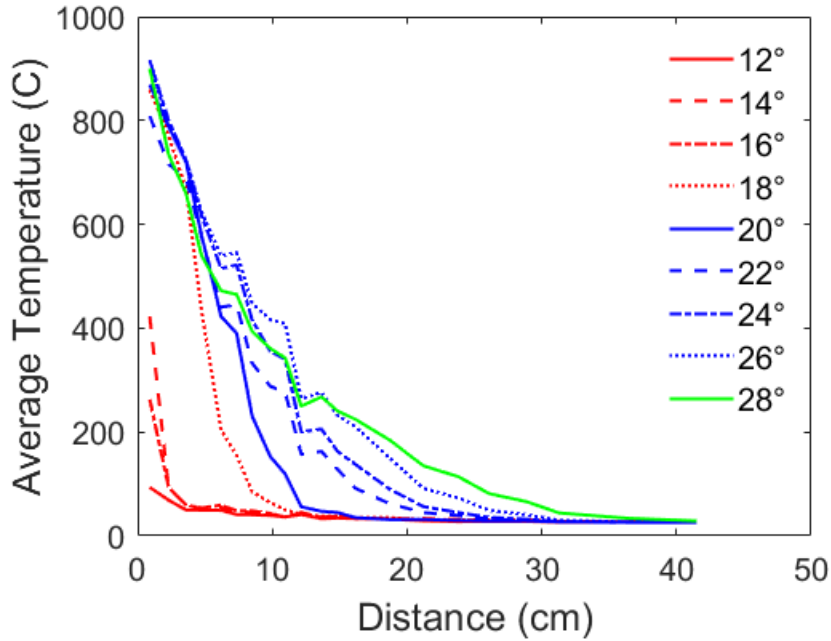


Figure 4.4: Average temperature profiles recorded downstream of a 7.6 kW fire from 9.2×50.2 cm burner

off as hot gases detach from the downstream surface, log-log plots are used to show the remaining tests, temperature profiles plotted on a normal scale are shown in Appendix 6.2. In order to view the transition of flame attachment more closely, temperature data is taken at 1° increments from 12° to 20° . The high resolution test is visible in Figure 4.6. The high resolution test gives a flame attachment threshold between 16° and 17° which is consistent with the previous experiment.

The high resolution test gives a flame attachment threshold between 16° and 17° which is consistent with the previous experiment. An interesting trend visible in the high resolution test is the increase in temperature downstream of the flame before the threshold attachment behavior occurs. There is a clear increase in temperature from 12° through 16° before the flame behavior changes and attaches to

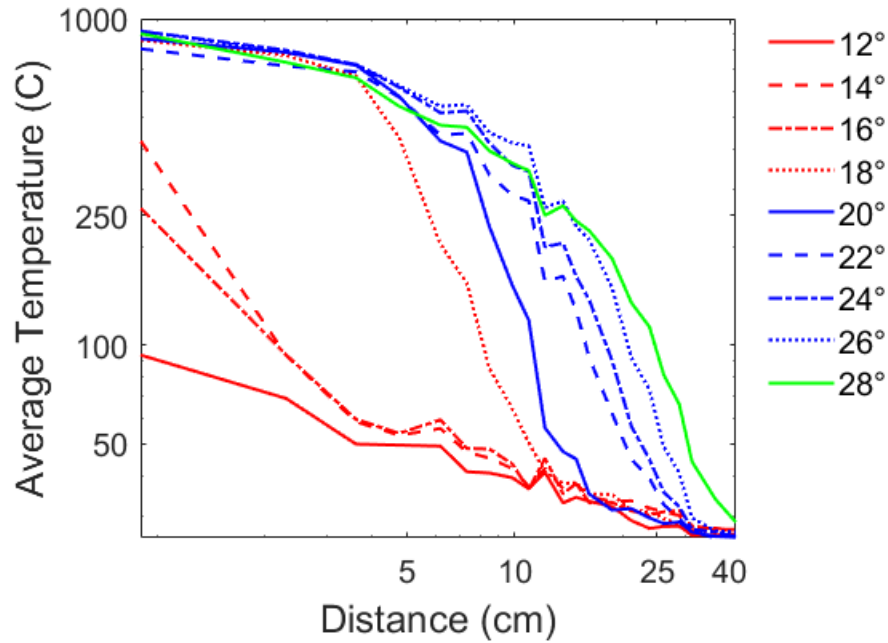


Figure 4.5: Average temperature profiles recorded downstream of a 7.6 kW fire from 9.2×50.2 cm burner

the downstream surface which is clearly visible in the 17° temperature profile. This temperature increase is most likely due to the proximity of the flame and plume approaching the downstream surface. Two larger fire heat-release rates were also considered to observe the impact of fire heat release rate on the downstream temperatures. Fire heat-release rates of 9.88 and 12.16 kW are shown in Figures 4.7, and 4.8. The 9.88 kW test is of particular interest due to the shadowgrams available for comparison with the helium tracers.

When heat-release rate is increased to 9.88 kW there are some visible impacts on the temperature profile for each angle of incline. The most meaningful difference observed at a the 9.88 kW flow-rate is the behavior of the 16° case. Compared to the 16° case in Figure 4.6 there is a clear extension in downstream flame presence.

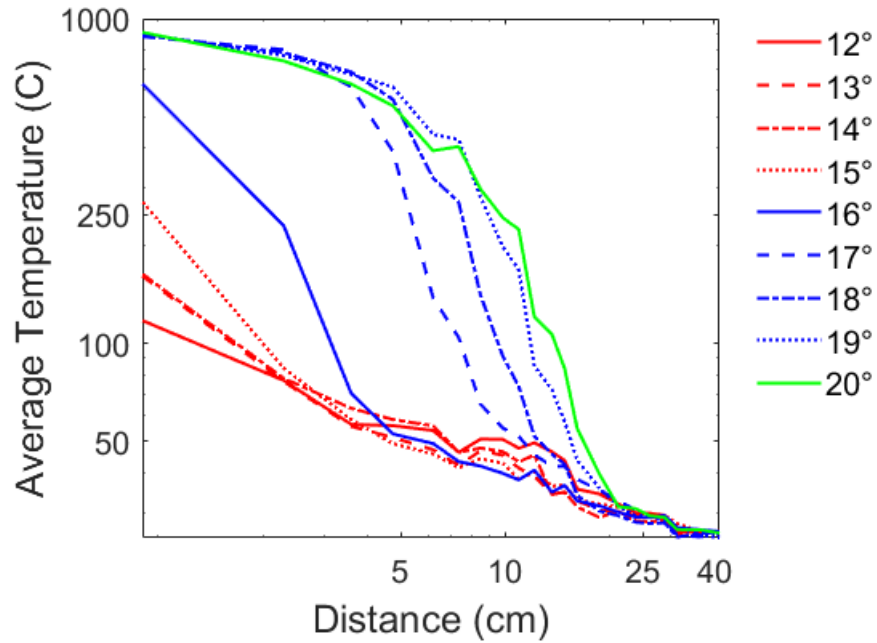


Figure 4.6: Average temperature profiles recorded downstream of a 7.6 kW fire from 9.2×50.2 cm burner

In 4.6 the 16° case shows a steep decline in temperature immediately, while in 4.7 there is a period of constant temperature between multiple thermocouples indicating attachment.

In comparison to the shadowgrams in Section 4.1, Figure 4.3 for a 9.88 kW fire shows the first helium inlet bent towards the flame at an incline of 15° , and covered by the plume at an incline of 20° . Flame and plume interaction with the inlets are not clear after this case. Temperature measurements in Figure 4.7 agree with this observed behavior. For a 14° incline it appears that the flame is still detached in Figure 4.7 indicating that there should be entrainment upstream of the flame as seen with the helium tracer in Figure 4.3. When inclined at 20° temperature measurements indicate significant heating past 15 cm. The shadowgrams show attachment

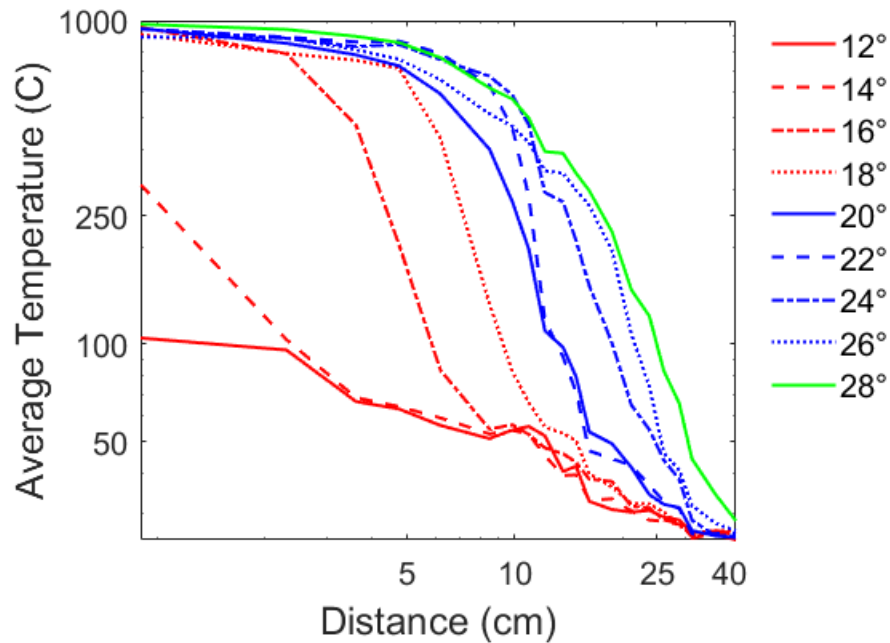


Figure 4.7: Average temperature profiles recorded downstream of a 9.88 kW fire from 9.2×50.2 cm burner up to at least the first inlet located at 16.3 cm but well before the second inlet at 26.5 cm.

For the 25° incline it is observed by looking under the tilt table that the heated plume extends near the second inlet at 26.5 cm, but the flame extends a noticeably shorter distance. The thermocouples data observes heating in this case that has already begun to decline, indicating that the extension of the plume still generates significant temperature increase downstream but does not generate the same amount of heat as the flame. The trend in the extension of temperature profiles continues in the 12.16 kW case and is shown in figure 4.8.

In this case the 14° case becomes attached for few cm before detaching. There is an obvious difference in the heating experienced in the 14° case between the 7.6

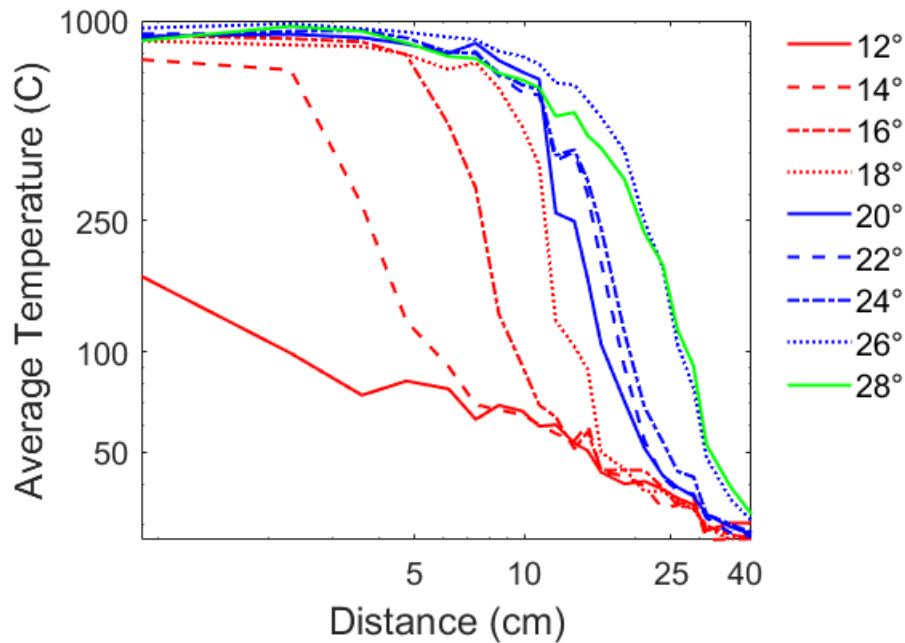


Figure 4.8: Average temperature profiles recorded downstream of a 12.16 kW fire from 9.2×50.2 cm burner

kW and 12.16 kW cases. This shows that fire heat-release rate has an impact of the flames propensity to attach to the downstream surface. The fire heat-release rate also alters the shape of the average temperature profiles downstream of the burner. The decay in temperature behaves differently; there is a more significant high temperature plateau before the temperature decays. This seems to indicate more substantial flame attachment to the downstream surface than in the lower flow rate tests.

These small scale tests show influence of angle, incline and heat-release rate. A large scale experimental apparatus was developed to systematically observe the impacts of heat-release rate, incline, concurrent flows, aspect ratio, and heat release per unit area on a scale closer to what would be observed in a wildland fire.

Chapter 5: Large-Scale Tilt Table Results

5.1 Experimental Outline

This study considered 3 different fuel flow rates and four different burner sizes. These 12 different fire conditions were tested at angles between 0° - 30° and wind speeds between 0 m/s - 0.762 m/s. Different burner dimensions created variable aspect ratios which were calculated by dividing the length of the burner by the width of the burner. To alter the aspect ratio the burner depth is varied. Table 5.1 presents a summary of all reported conditions. Some tested conditions are not presented because they did not exhibit downstream heating, occurring at low slopes and wind speeds where the nearly vertical fire does not interact with sensors on the downstream surface. In order to simplify the analysis, the inclined and forced flow cases will first be considered individually.

5.1.1 Initial Results: Incline

To compare to the small tilt table tests, raw temperature profiles were considered in order to observe overall trends in behavior. After raw temperature profiles,

Table 5.1: Different Test Conditions for each angle of incline

<i>Incline</i> ($^{\circ}$)	Heat Release Rates (kW)	Wind Speed (m/s)	Burner Width (cm)	Aspect Ratios (L_b/W_b)
0	72,152,228	0.304, 0.508, 0.726, 1.016, 1.27 m/s	15.24, 30.48, 45.72, 60.96	12, 6, 4, 3
6	72,152,228	0.304, 0.726	15.24, 30.48, 45.72, 60.96	12, 6, 4, 3
12	72,152,228	0, 0.304, 0.726	15.24, 30.48, 45.72, 60.96	12, 6, 4, 3
18	72,152,228	0, 0.304, 0.726	15.24, 30.48, 45.72, 60.96	12, 6, 4, 3
24	72,152,228	0, 0.304, 0.726	15.24, 30.48, 45.72, 60.96	12, 6, 4, 3
30	72,152,228	0, 0.304, 0.726	15.24, 30.48, 45.72, 60.96	12, 6, 4, 3

instantaneous temperature measurements were considered, and a method to determine attachment length was developed. Average attachment lengths are then used to develop understanding of flame behavior under the considered conditions.

5.1.1.1 Raw Temperature Profile Averages: Incline

Raw temperature profiles were measured using the same method as the small tilt table. A linear array of 60 thermocouples described in chapter 3 was used to measure temperatures 120 cm downstream of the burning region. Temperature profiles are considered for four different angles of incline at three different heat release rates with no forced flow. Log-log scales are shown in presented graphs to clearly distinguish temperature profiles downstream. Temperature profiles from the smallest fire heat-release rate considered are shown in Figure 5.1, which used a fuel flow-rate of 50 SLPM or a 76 kW fire.

Although there is significantly less angle resolution than could be achieved on the small tilt table, similar trends are observed. Downstream temperatures indicate that the flame is not attached to the surface in the 12° case. It seems that partial attachment occurs in the 18° case as temperatures close to 1000°C are recorded until they decrease drastically after about 5 cm downstream of the burner. Results from the 24° and 30° angles indicate complete attachment as temperatures near 1000°C are measured about 10 cm downstream of the burner. Temperature readings then slowly decay for the 24° and 30° cases down the rest of the downstream surface. No obvious point of detachment is observed for these cases. To observe the impact of fire

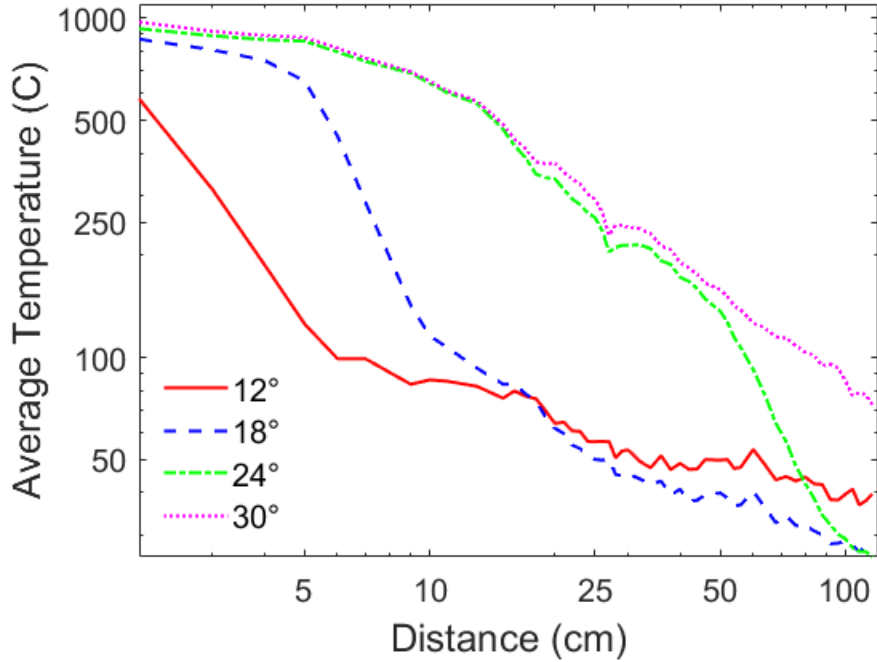


Figure 5.1: Average temperature profiles recorded downstream of a 76 kW fire from a 15.24 cm × 183 cm burner

heat-release rate on the downstream temperatures, as in the previous experimental set up, two other fire heat-release rates were also considered. Figures 5.2 and 5.3 show fuel flow rates of 100 and 150 SLPM, or 152 and 228 kW fires respectively.

The effects of increased flow-rates are observed again as they were with the smaller tilt table. The most obvious impact of the increase in flow rate is a different downstream temperature profile for the 18° case. A peak temperature of about 1000°C is observed more consistently and further downstream along the array of thermocouples. Downstream temperature profiles continue this extension of high temperatures for the 24° and 30° cases. Downstream temperatures read close to 1000°C at 11 cm in the 18° case before beginning to decay, more than twice the distance seen with the 76 kW fire. The 228 kW fire shows a continuation of this trend,

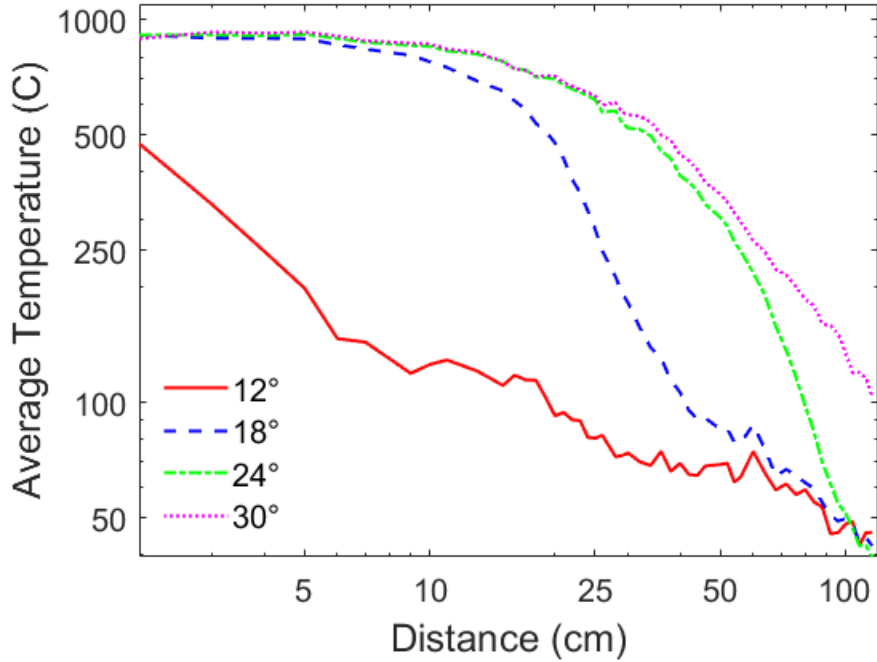


Figure 5.2: Average temperature Profiles recorded downstream of a 152 kW fire from a 15.24 cm × 183 cm burner

with temperatures near 1000°C measured at further distances with a temperature decay that is slower.

It is apparent from these experiments that the fire heat-release rate is a major driver in downstream heating for steeper slopes (e.g. the 18° to 30° cases), although the 12° case is not significantly impacted by HRR. Steeper slopes tend to lead to significant flame attachment where the flame almost completely rests along the surface and the extended distance with higher heat-release rate is seen in longer flame lengths. For unattached flames, the flames tend to detach early enough that little effect is seen in the attachment distance with fire heat-release rate. It is likely that the combination of entrainment upstream of the fire and plume tilt toward the downstream surface is not influential enough to cause flame attachment. This is an

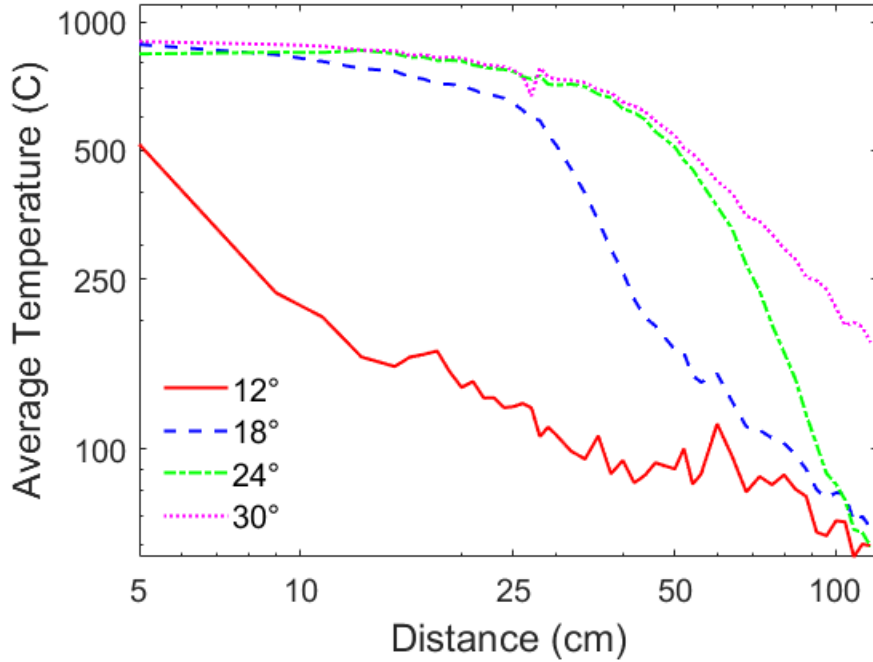


Figure 5.3: Average temperature Profiles recorded downstream of a 228 kW fire from a 15.24 cm × 183 cm burner

important observation, as understanding transition between these two regimes will become important for understanding rates of spread which are driven by forward heating. Unfortunately the limited number of angles being tested restrict the resolution of the experiments. Future tests on more angles between 12° and 18° would help describe this threshold behavior further. Still, the length of the attachment region and general flame behavior can be closely studied for the angles the were tested.

To further investigate the influence of heat-release rate, multiple heat-release rates were studied using average temperature profiles at a constant degree of incline. Three flow rates of propane were used to create three heat-release rate conditions; coupled with variation in the aspect ratio, 12 heat-release rates per unit area (\dot{Q}'')

conditions are produced. The 12 different cases for a 18° slope are shown in Figure 5.4.

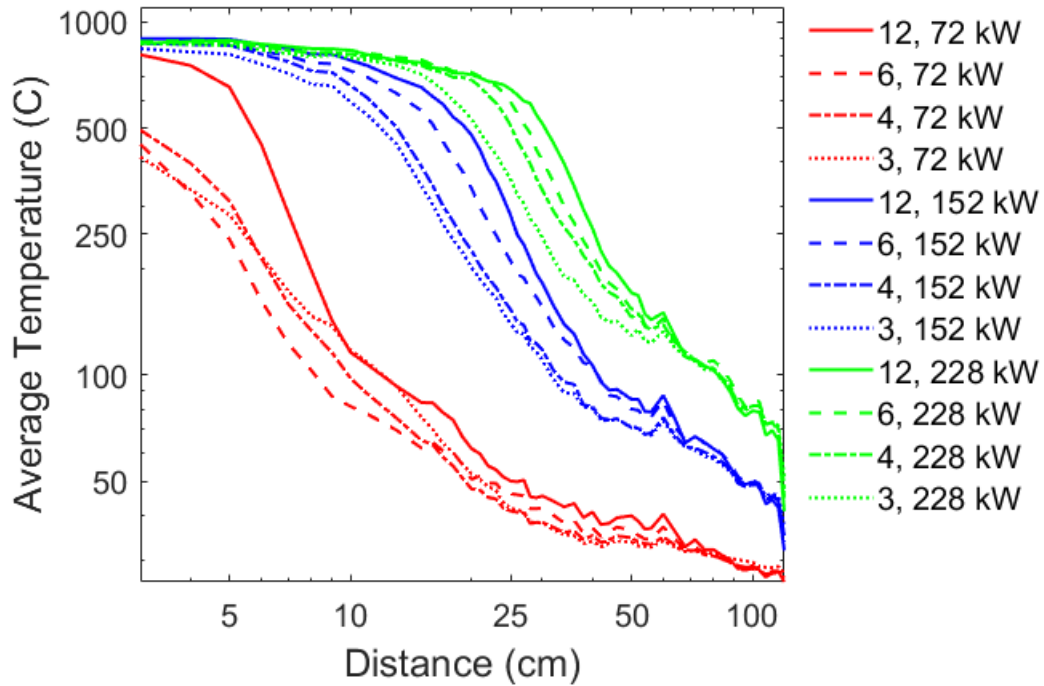


Figure 5.4: Average temperature profiles recorded downstream of 12 fires with varying heat-release rate per unit area on an 18° incline. Legend displays the aspect ratio and the fire heat-release rate for each test.

The 18° case was used to observe the impact of altering the aspect ratio and fire heat-release rate because it lies near a threshold for attachment and showed significant variation with different in fire heat-release rates in Figures 5.1, 5.2, and 5.3. In Figure 5.4 it is shown again that the overall flow rate of fuel, or heat release rate has a significant impact on downstream heating. The temperature profiles for the 24°, and 30° cases are shown in Appendix 6.2, the 12° case was not considered because of the lack of downstream heating recorded by the thermocouples. It seems

that threshold behavior of the flame is impacted in this case by the fire heat-release rate. The 72 kW fire shows a flame that is unattached from the surface, with no temperatures downstream near the 1000°C maximum temperature threshold observed with other fire heat-release rates. At the larger fire heat-release rates, a different temperature profile is observed with an extended length of thermocouples recording near 1000°C, typical of what was seen by an attached flame.

It is important to note that when the aspect ratio of the burner is changed the heat-release per unit area of the burning region is also changed. The aspect ratio is shown to have less of an impact than the change in overall heat-release rate or flow rate for the fire in Figure 5.4. Most cases only show a shift in the temperature profile downstream by a few cm, although in the unattached case it is shown that the largest aspect ratio in the 72 kW fire has a brief region of temperatures near 1000°C, which may indicate the presence of a flame (i.e. attachment at that point). It seems that most temperature profiles for each flow-rate follow the same trend, with some small variation near the detachment threshold.

Average temperature profiles show that in inclined fires without the influence of a forced flow, inclination and overall heat release rate are the controlling components of downstream temperature. Detachment of the flame is still not easily determined from the average temperature curve as the decrease in temperature with distance seems to be gradual. Instantaneous temperature profiles are thus considered in order to more carefully distinguish flame attachment and detachment behavior.

5.2 Instantaneous Temperature Measurements and Attachment Length

Average temperature profiles describe overall flame behavior but they do not clearly define the detachment location of the flame. As detachment eventually results in a drastic change in heating and thus flame spread behavior, this location needs to be captured. Instantaneous temperature profiles were considered in an attempt to investigate flame detachment. Since thermocouple measurements were recorded at 500 Hz, there were ample time steps to observe time varying flame behavior. Instantaneous temperature measurements were found to show clear flame structures propagating down the array of thermocouples. It was observed that there is a significant difference between the average temperature profile and the instantaneous temperature profile measured by the thermocouples at each time step. Figure 5.5 shows an example of how the instantaneous temperature profile can vary from the average.

If only the average temperature profile is considered to represent downstream heating, it is obvious that some aspects fire behavior are ignored. Average temperature profiles ignore instantaneous flame structures that could influence flame spread and the heating of downstream fuels. For example, it is known that intermittent heating can impact the rate of spread and ignition times in different fuels [41]. The instantaneous temperature curves show clear temperature dropoffs that propagate down the length of the fuel bed, shown in Figure 5.5. These temperature drop offs could give some insight on attachment of the flame.

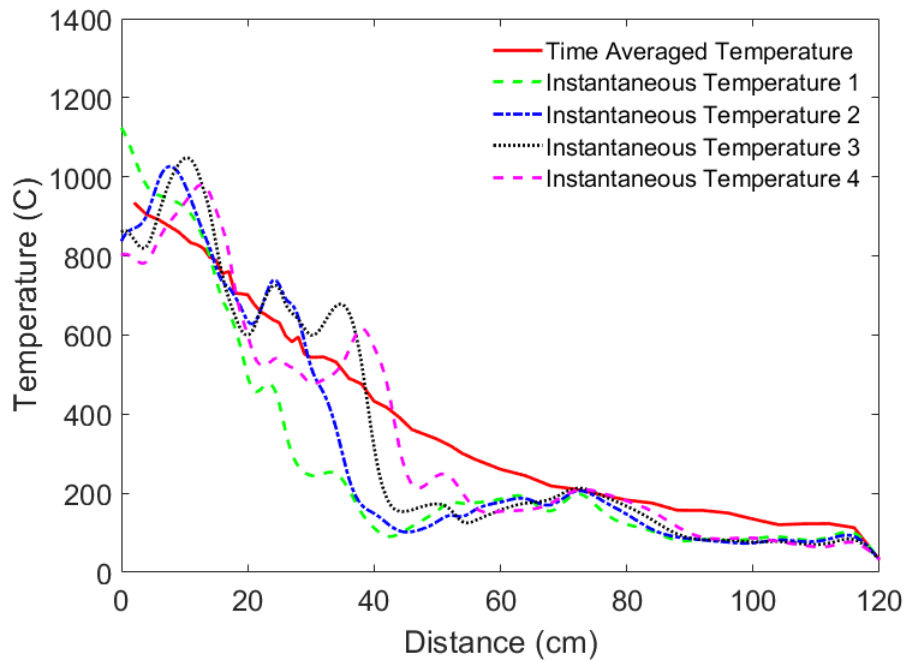


Figure 5.5: Instantaneous temperature profiles in 25 Hz incitements vs average temperature profile for a 152 kW fire from a 15.24 cm \times 183 cm burner at a 30° incline

To quantify these prominent drops in temperature, a MATLAB script was written to analyze the instantaneous temperature data and identify the locations of significant temperature change. The abrupt change in temperature is likely to occur due to the presence of cool ambient air entraining on the downstream side of the flame as the flame detaches from the surface. If this is the case, then the steep change in temperature shows the location of the detachment point of the flame or the hot plume. Since no established temperature threshold exists for flame or plume detachment, an empirically-determined temperature change per unit length threshold of 44 K/cm is used to identify the point where the flame detaches. This

temperature threshold was determined through a trial-and-error method using many different instantaneous temperature profiles. The distance from the edge of the downstream side of the burner to this point is considered to be the attachment length in this study. To further improve this threshold method, a temperature range (300 to 650°C) was implemented to prevent the threshold from marking detachment outside of reasonable temperatures where the flame or heated plume would be present. Attachment points were then determined for the different conditions considered in this study. These attachment lengths show significant variability in flame location.

The variability in flame location for a 30° case with a 72 kW fire with 15,000 recorded time steps, or 30 s (half a test), is shown in Figure 5.6.

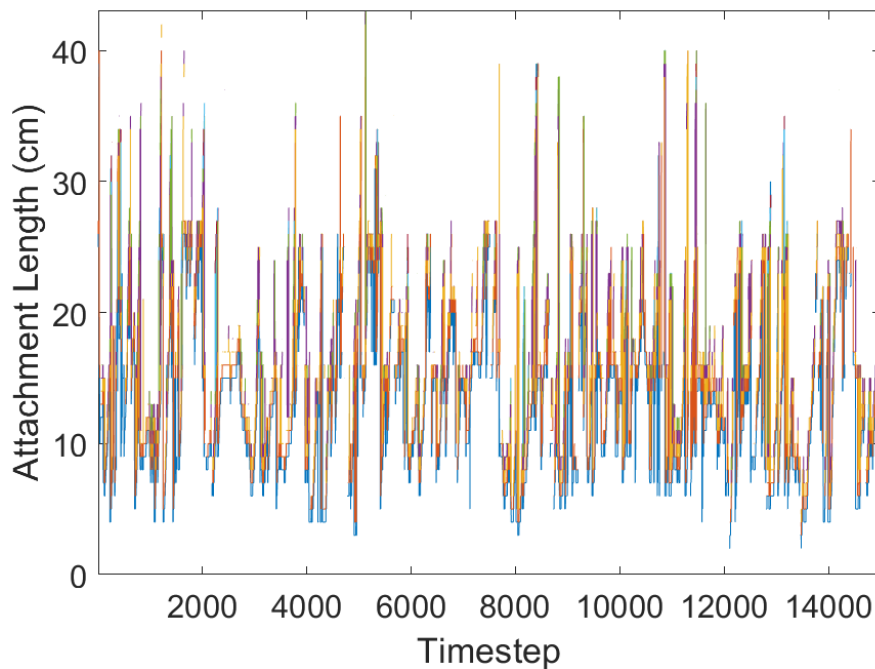


Figure 5.6: Measured attachment length versus time for a 72 kW fire from a 15.24 cm × 183 cm burner at 30°

Change in the flame location highlights the importance of understanding intermittent heating, and how not only considering the average data but also the instantaneous flame behavior could give more insight into downstream heating. It was discovered that if these attachment lengths were compiled and binned, a log-normal fit appropriately represented the data as shown in Figure 5.7.

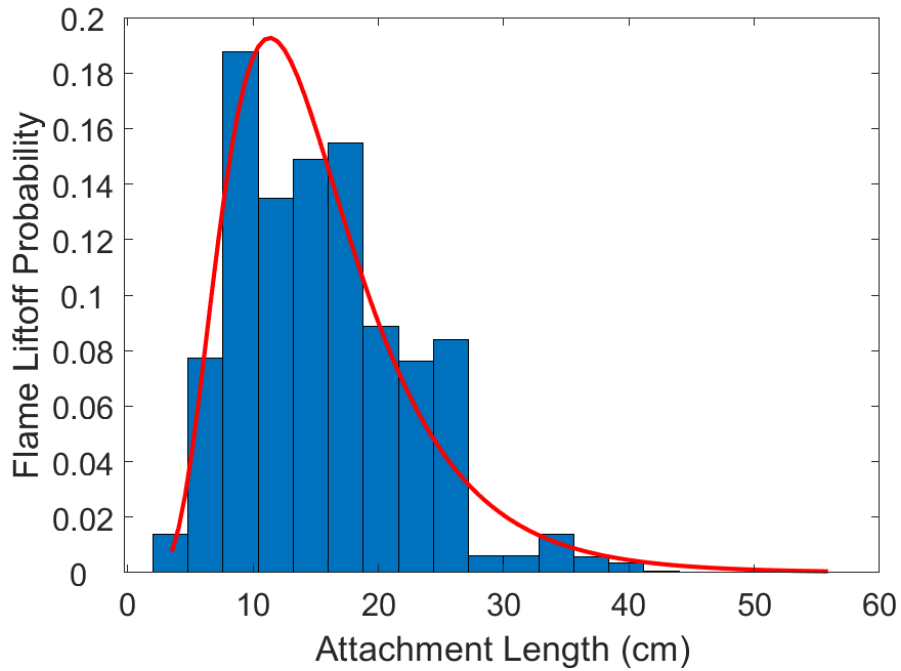


Figure 5.7: Flame detachment probability versus attachment length for a 72 kW fire from a 15.24 cm \times 183 cm burner at 30° fit with a probability distribution function (PDF).

These log normal fits can then be used as a tool to investigate and compare flame location under different aspect ratios, angles, and heat release rates for different inclines and wind speeds. Figure 5.7 shows what an average fit looks like for these binned attachment lengths, more examples are shown in Appendix 6.2. It was determined through trial and error that 15 bins worked well for these tests

and represented the spread of the measured attachment lengths. The frequency of measured attachment lengths at each attachment length are normalized by the total number of measured attachment lengths to show the probability of detachment at each location downstream, or probability distribution function (PDF). These PDFs show the variability of the flame location, moving back and forth down the burn bed depending on the conditions.

5.3 Average Attachment Lengths and PDFs: Incline

With the PDFs as a visual tool, large amounts of attachment length data can be compared in order to observe how flame location changes with variable conditions without just using a simple average. The PDFs are used to give a rough shape to the flame attachment location; it is known that the log normal fit will not be a perfect representation for each flame, although it will be useful for showing flame attachment lengths for different conditions and how it varies based on ambient conditions.

PDFs are used to observe the change in flame behavior for different angles of incline with a uniform flow-rate and a constant aspect ratio. Similar to the average temperature profiles previously presented, a threshold behavior is observed using the PDFs shown in Figure 5.8.

Transition in flame behavior occurs between 12° and 18° , the attachment length extends significantly from a mean location below 10 cm to a mean location at around 30 cm. The 12° case shows a high probability of an attachment length below 10 cm, with no extension downstream. After the flame starts to tran-

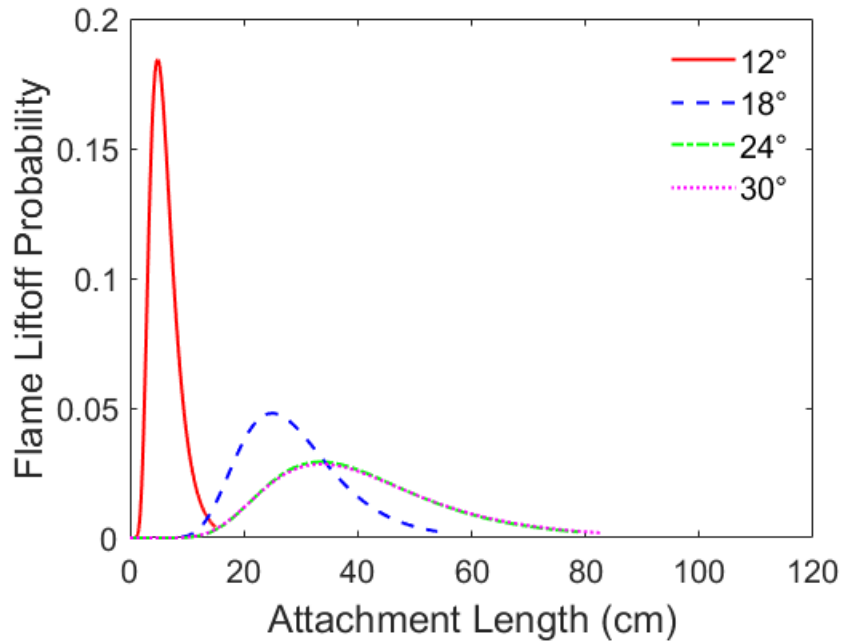


Figure 5.8: PDF comparison for a 228 kW fire from a 15.24 cm \times 183 cm burner at 4 inclines

sition in the 18° case, the mean flame location moves forward, hence the probability of the attachment length extends over a much broader area. This shows that as flame attachment increases, the variability does as well. The flame may therefore be separating and breaking off into smaller flames as it extends downstream, causing significant fluctuations in temperature as flame presence varies rapidly.

An incline of 18° is then considered for multiple flow rates similar to the average temperature profile analysis. Figure 5.9 shows how flame detachment location varies as the aspect ratio and fire heat-release rate are varied. Figure 5.9 shows similar results to the average temperature profiles, unattached flames for the 72 kW fire show a high probability of the flame detaching below 10 cm. As the fire heat-release rate is increased to 152 kW, the flame attaches and the variance in the location of

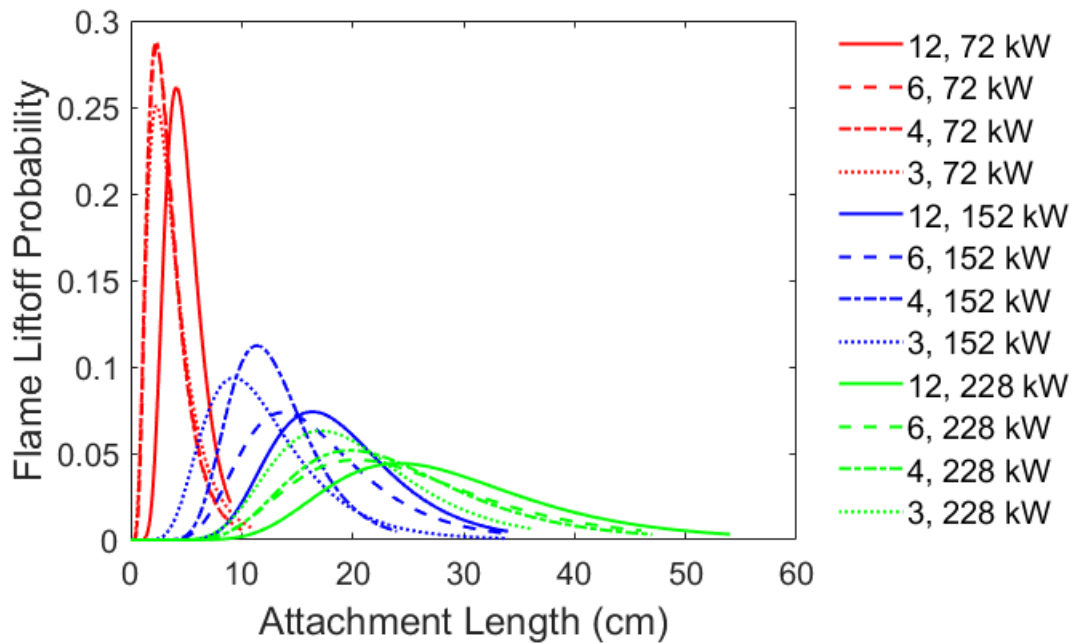


Figure 5.9: Incline histogram comparison with no forced flow at an 18° incline.

Legend displays the aspect ratio and the fire heat-release rate for each test.

flame detachment increases. The attachment variance continues to increase for the 228 kW test, although it is important to note that the PDFs also transpose down the length of the bed as the fire heat-release rate increases. Although variation in flame detachment is high for the 228 kW test there are no detachment points measured below 10 cm.

The peak of each PDF is taken as the average attachment length for each test and is used to get a characteristic flame location for each condition. In order to determine the most influential parameters, attachment length is plotted against each varied condition on the large tilt table to determine a correlation. Development of a correlation is important, because a relationship between relevant quantities such as fire heat-release rate, slope, aspect ratio, etc. could be useful for predicting the

extent of downstream heating and therefore flame spread rates. It was found that angle of incline and overall heat release rate give the best linear fit. Figure 5.10 shows the best fit possible with the tested parameters.

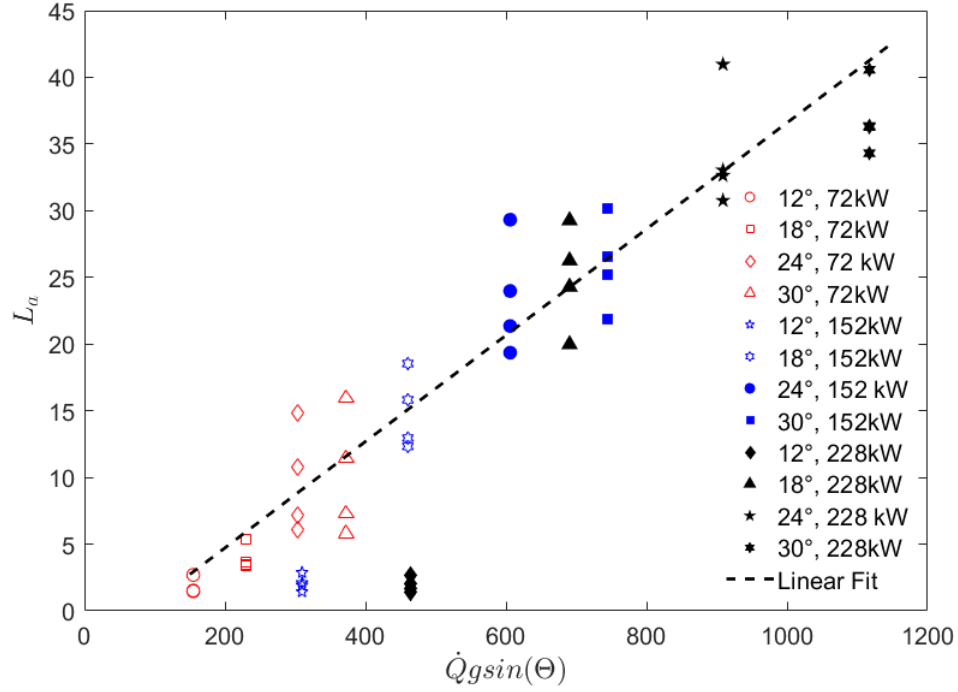


Figure 5.10: $\dot{Q}g\sin(\theta)$ (kW m/s²) versus mean attachment length (cm) for the inclined table with no forced flow. The legend displays each angle of incline and fire size considered. Each condition contains four different aspect ratios.

In Figure 5.10 the average attachment length L_a is plotted against the overall heat release rate \dot{Q} multiplied by the vertical component of gravity $g\sin(\theta)$. The vertical component of gravity takes into account the angle of incline and is a good representation of the influence of buoyancy. A strong linear relationship is shown for inclines varying from 18° to 30° given by the equation,

$$L_a = 0.03984\dot{Q}g\sin(\theta) - 3.245, \quad (5.1)$$

presented in cm. When these points are fit an R-squared value of 0.9 is found. These angles are considered because these are all tests where some degree of flame attachment occurs. The 12° case shows a different trend. As the heat-release rate and angle increase the attachment length remains relatively unaffected. This correlation demonstrates that there are two separate regimes that occur between the attached and unattached flame. Wind-driven flames on a flat surface are now considered to compare how flame attachment varies for buoyancy-driven versus forced-flow driven conditions.

5.3.1 Initial Results: Forced Flow

Flames under the influence of a forced flow at 0° incline are analyzed using the same methods used for the inclined conditions in order to compare the downstream temperature profiles and flame locations.

5.3.1.1 Raw Temperature Profile Averages: Forced Flow

Before considering the average temperature profiles for forced flow conditions, it is important to note that experiments with the forced flow of 0.304 m/s and 0.762 m/s were run in one sequence of experiments and all other wind speeds were tested independently in a separate sequence of experiments. The wind tunnel in Missoula underwent repairs in-between these two test series which may cause small discrepancies in the data due to a change in the conditions. Results from different test sequences are compared because limited conditions were available where uniform

flow rates were used for all wind speeds. Two such conditions were a 152 kW fire with a 30.48 cm \times 183 cm burner, shown in Figure 5.11, and a 228 kW fire with a 45.72 cm \times 183 cm burner, shown in Figure 5.12.

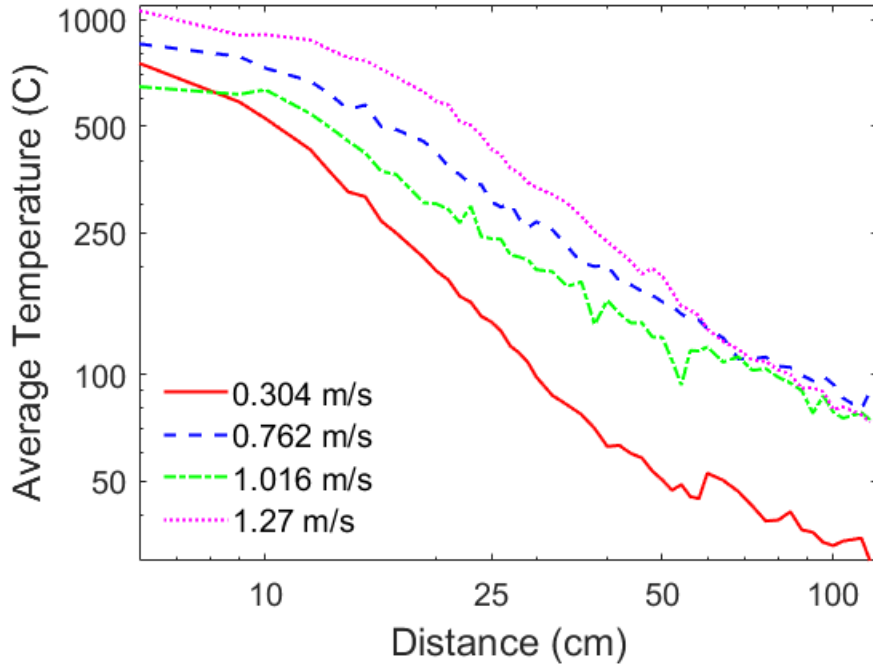


Figure 5.11: 152 kW fire from a 30.48 cm \times 183 cm burner with varying forced flow while at the horizontal (0°)

In Figure 5.11 most temperature profiles seem to gradually decay in temperature, showing less of a plateau of flame presence and attachment than the inclined temperature profiles. It seems that the flame is bent towards the surface and then gradually detaches, detaching at a proportionally slower rate for each wind speed. Although there is an anomaly with the 0.762 m/s wind speed, it appears to have higher rates of downstream heating than the 1.016 m/s wind speed. This anomaly occurs again with the 45.72 cm \times 183 cm burner and 228 kW fire shown in Figure 5.12.

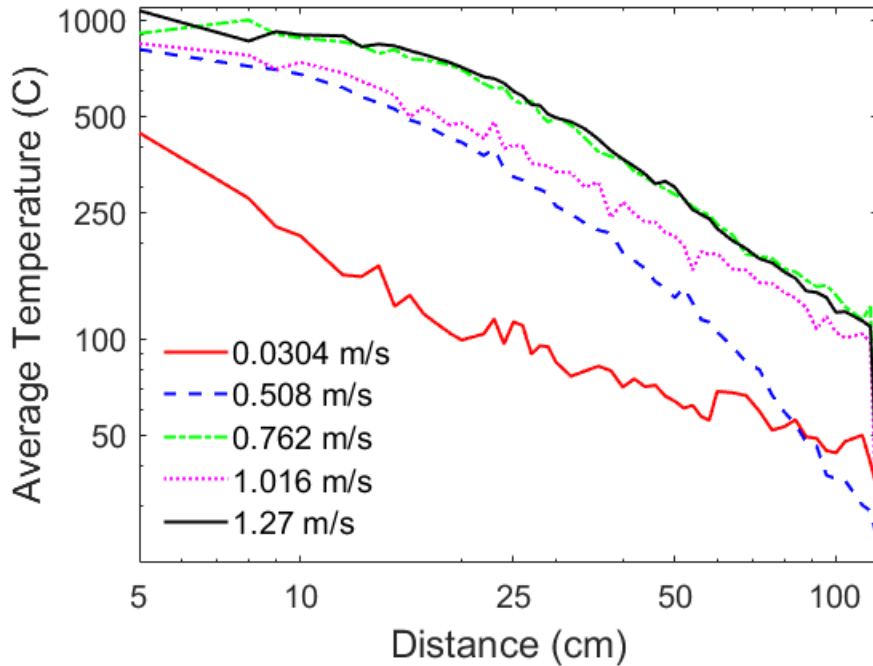


Figure 5.12: 228 kW fire from a 45.72 cm × 183 cm burner with varying forced flow while at the horizontal (0°)

It seems unlikely that the 0.762 m/s wind speed induces some kind of critical heating, especially since the fastest wind speed tested of 1.27 m/s shows a increase in temperature. It is likely that this anomaly can be attributed to changes made to the wind tunnel, or thermocouples and does not represent a physical phenomena. These tests should be repeated in future work to clarify this data.

In contrast to the gradual decline in temperature for each wind speed in Figure 5.11, Figure 5.12 shows attachment behavior as previously observed in the inclined scenarios. The 0.304 m/s test shows separation from the other temperatures that indicates it is unattached. This is interesting because the 0.304 m/s test in Figure 5.11 is less distinguishable from the other wind speeds. The parameters altered between these two tests are the aspect ratio and fire heat-release rate. It seems that

the tests in Figure 5.11 behave more like unattached flames while Figure 5.12 show a threshold behavior between the 0.304 m/s wind speed and the 0.762 m/s wind speed. Since both heat release rate and aspect ratio were varied between these two tests, its not possible to tell what impacted the downstream fire behavior.

More tests near this flame attachment threshold were completed to investigate the impact of aspect ratio, Figure 5.13 shows the 0.304 m/s wind speed for all flow rates and aspect ratios considered. The 0.304 m/s tests show there is a relationship

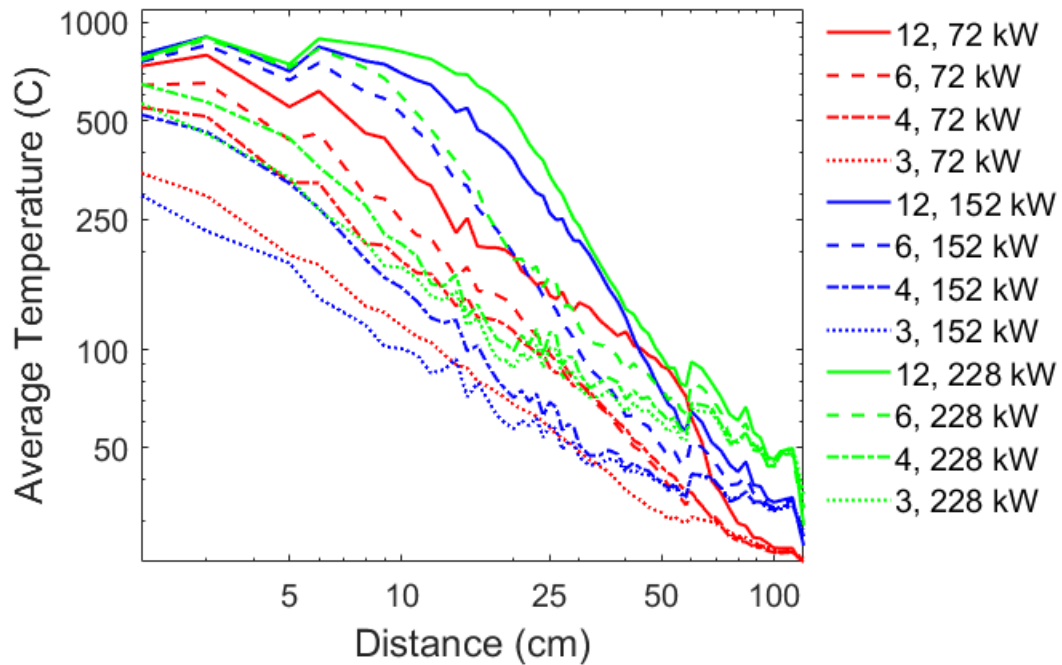


Figure 5.13: Temperature profiles for all aspect ratios and heat-release rates under the influence of a 0.304 m/s forced flow. Legend displays the aspect ratio and the fire heat-release rate for each test.

between flow-rate, aspect ratio, and the downstream temperature profile. Rather than all of the temperature curves being grouped by the overall heat-release rate, temperature curves appear to be grouped by the aspect ratio here. This indicates

the dynamics of flames around the attachment threshold are influenced by altering the aspect more than attached flames are. For comparison the same temperature profiles are plotted for the 0.762 m/s forced flow in Figure 5.14.

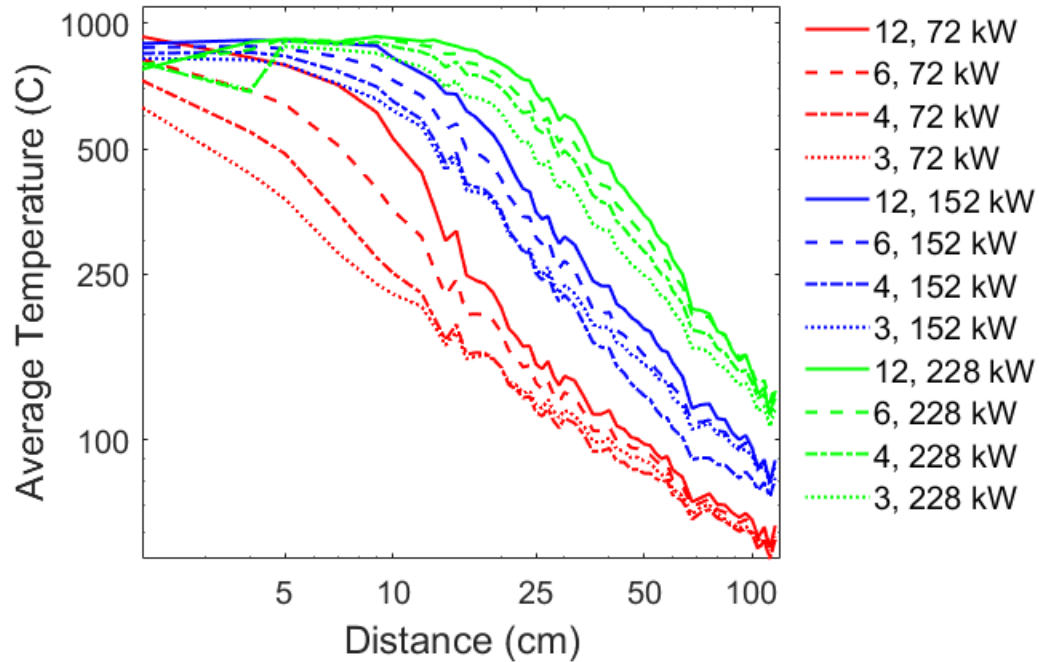


Figure 5.14: Temperature profiles for all aspect ratios and heat-release rates under the influence of a 0.762 m/s forced flow. Legend displays the aspect ratio and the fire heat-release rate for each test.

The 0.762 m/s wind speed reveals how the relationship with the downstream temperature and aspect ratio changes when the flame is attached. Each temperature profile is now grouped by the overall heat-release rate of the fire and shows very little dependence on aspect ratio. This transition in fire behavior is important to understand, as fire heat-release rate seems to drive flame attachment length in Figure 5.14, but plays a less significant role near the flame attachment threshold as seen in Figure 5.13.

5.3.1.2 Instantaneous Attachment Lengths and PDFs: Forced Flow

Flame location and attachment length are determined using the instantaneous temperature measurements as in the inclined section. Wind speeds of 0.304 m/s and 0.762 m/s are compared since conditions for these two tests are known to be the same because they were conducted during the same test sequence. Figure 5.15 shows the influence of aspect ratio near the attachment threshold shown in Figure 5.13 with average temperature profiles, but with the PDFs determined using measured instantaneous flame attachment. PDFs give insight into how the flame locations are impacted by the change in aspect ratio near the threshold for attachment. Figure 5.15 shows the first instance where larger flame attachment and variance has not been directly dependant upon flow-rate alone in this study.

The PDFs in Figure 5.15 are grouped primarily by aspect ratio, a 152 kW fire from a 60.96 cm \times 183 cm burner has less probability of flame attachment downstream than a 72 kW fire from a 30.48 cm \times 183 cm burner and a 72 kW fire 15.24 cm \times 183 cm burner. This is counter-intuitive as it would be expected that more downstream heating would be present with a fire twice the size in a uniform forced flow. It is proposed that flame dynamics near the threshold for attachment are influenced by aspect ratio more than by overall heat-release rate. Larger aspect ratios seem to encourage flame attachment which drives downstream heating, Figure 5.15 displays how smaller fires heat-release rates can have more flame presence and more heating downstream than large fires if they are attached to the surface. A larger aspect ratio creates a thinner burning region which decreases the buoyant

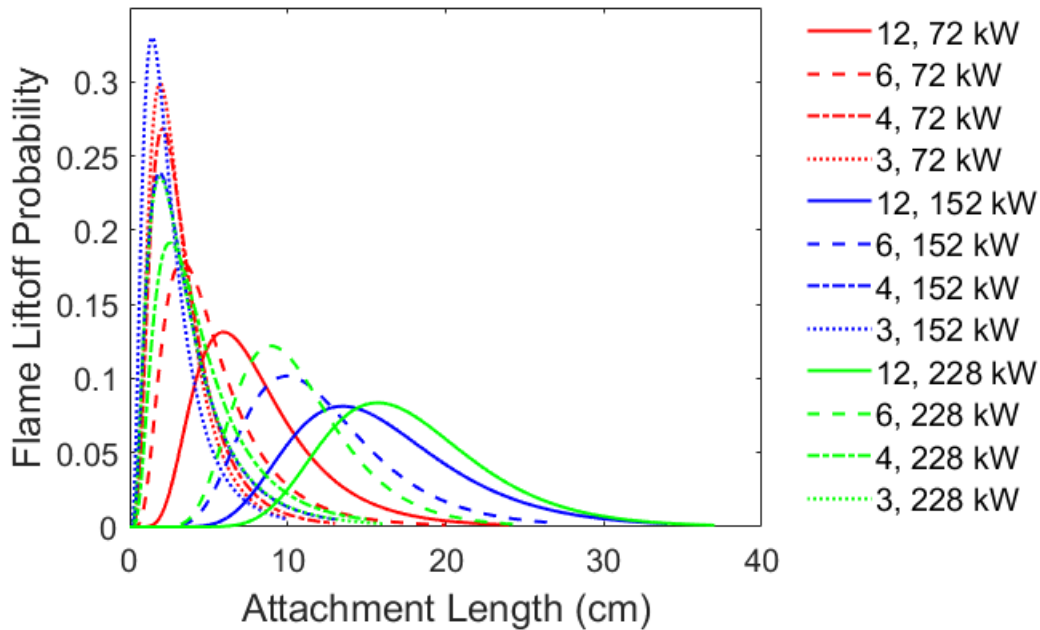


Figure 5.15: PDFs of the attachment lengths for multiple aspect ratios and heat-release rates are shown for a 0.304 m/s wind speed. Legend displays the aspect ratio and the fire heat-release rate for each test.

strength encountered by a forced flow perpendicular to the width of the burner, this would lessen the momentum necessary in a forced flow to cause the flame to be pushed toward the downstream surface. Figure 5.16 shows how the flame behavior returns to expected trends when considered flames are attached to the surface and are no longer near the threshold for attachment. Each flame is then grouped by the overall fire heat-release rate in terms of flame detachment probability.

5.3.1.3 Average Attachment Lengths and Correlations: Forced Flow

In this section correlations were taken between relevant parameters and the average attachment lengths from the 0.304 m/s and 0.762 m/s forced flows. It is

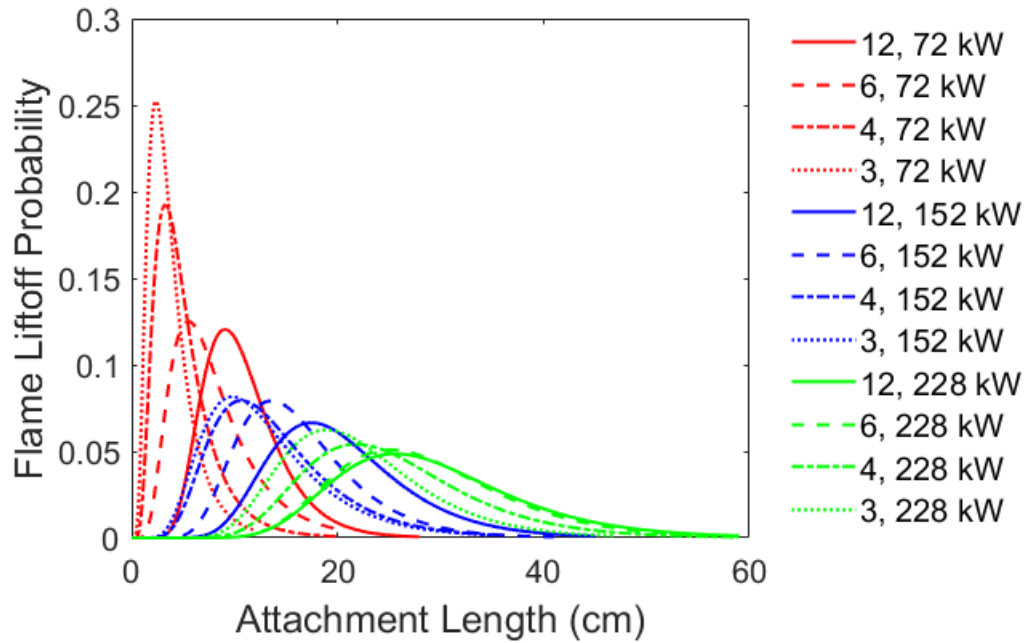


Figure 5.16: PDFs at all aspect ratios and fire heat-release rates for a 0.762 m/s velocity. Legend displays the aspect ratio and the fire heat-release rate for each test.

expected that the 0.762 m/s test will show a stronger relationship with the overall heat release rate of the fire than the 0.304 m/s test. Figure 5.17 shows all average attachment lengths L_a measured with a 0.304 m/s forced flow plotted against the upstream velocity $u_{upstream}$ measured 30 cm ahead of the burner 5 mm above the surface of the table using a hot-wire anemometer multiplied by the overall heat release rate \dot{Q} . There is no trend in this data; four different data points are shown for each measured velocity and overall heat-release rate, each of these points is from a different aspect ratio. There is significant variation shown between each aspect ratio for these tests, and the variation does not appear to be uniform. This plot contributes to the proposed idea that threshold behavior is not driven by overall heat-release rate near the attachment threshold, but by the change in aspect ratio.

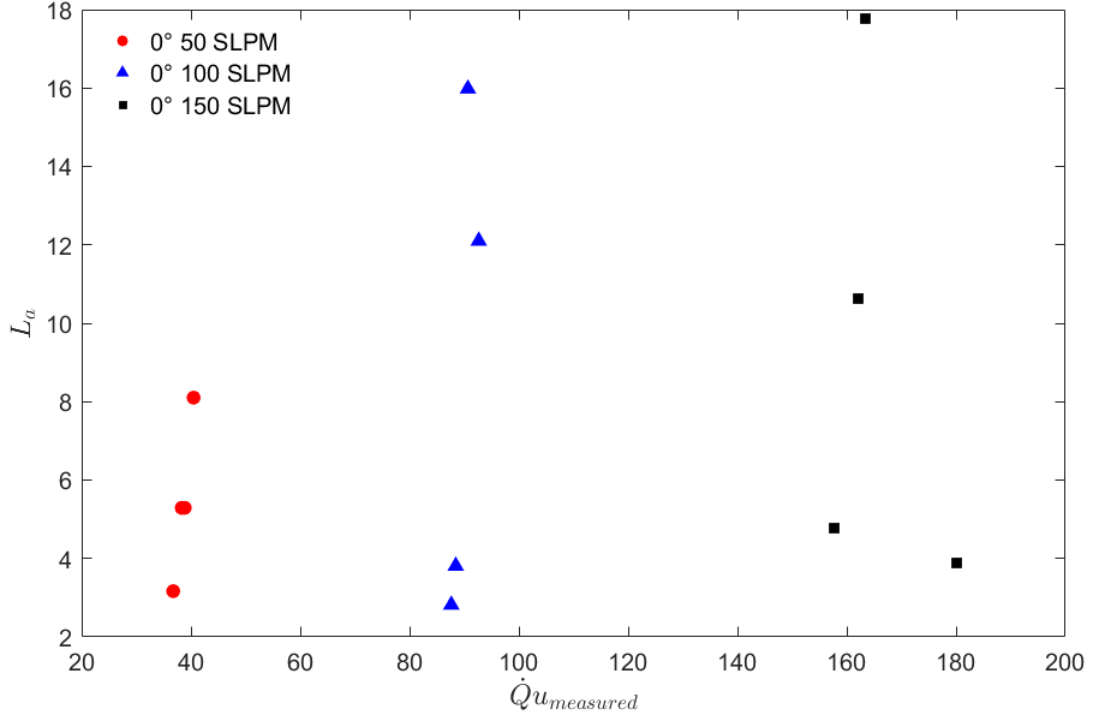


Figure 5.17: $\dot{Q}u_{measured}$ (kW m/s) versus mean attachment length (cm) for a 0.304 m/s forced flow. The legend displays each fire size considered. Each fire size contains four different aspect ratios.

Figure 5.18 shows the average attachment points from the same test as in Figure 5.17, but with the heat-release rate per unit area considered rather than overall heat-release rate. On the x -axis, the heat-release rate per unit area \dot{Q}'' is multiplied by the upstream velocity and plotted against average attachment length L_a . These variables were found to have a linear relationship given by,

$$L_a = 0.02909\dot{Q}''u_{measured} + 2.609, \quad (5.2)$$

which has an R-squared value of 0.78 (with L_a given in cm). The heat-release rate per unit area is varied by altering the burner depth which also changes the aspect ratio of the burning region. As the burner depth becomes smaller the heat-release

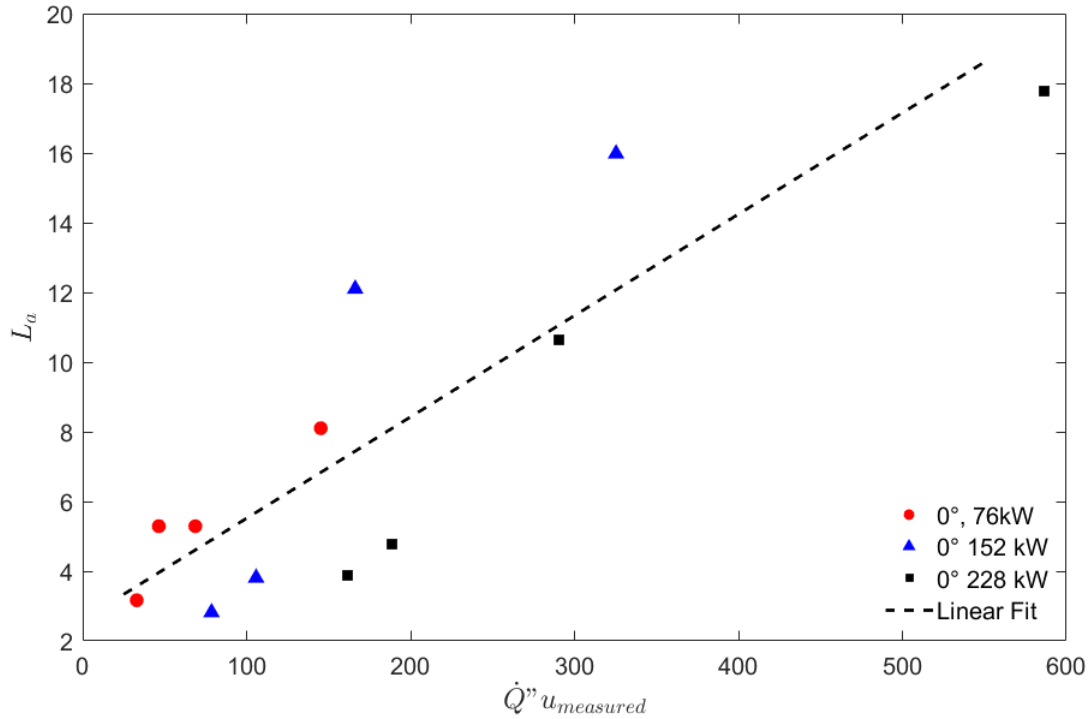


Figure 5.18: $\dot{Q}'' u_{measured}$ (kW/m² m/s) versus mean attachment length (cm) for a 0.304 m/s forced flow. The legend displays each fire size considered Each condition contains four different aspect ratios.

rate per unit area and the aspect ratio increase on the experimental apparatus used in this study.

The 0.762 m/s wind condition is shown in Figure 5.19 and a much different trend is observed between the average attachment length and heat-release rate. There is a linear relationship between the attachment length and heat-release rate given by the equation,

$$L_a = 0.1134\dot{Q}'' u_{measured} + 1.725 \quad (5.3)$$

which has an R - squared value of 0.8956 (with L_a given in cm) This is a significant change from the 0.304 m/s wind speed where no relationship was visible. This

is likely due to the difference in the flame dynamics between the 0.304 m/s and the 0.762 m/s cases. These relationships support observations from the PDFs that indicated the overall heat-release rate has more of an influence under the 0.762 m/s wind speed, while the aspect ratio is a driving factor under the 0.304 m/s wind speed. Variation of the aspect ratio still has an influence in Figure 5.19 but is much less significant than in Figure 5.17 and does not appear to be a key influence on attachment length.

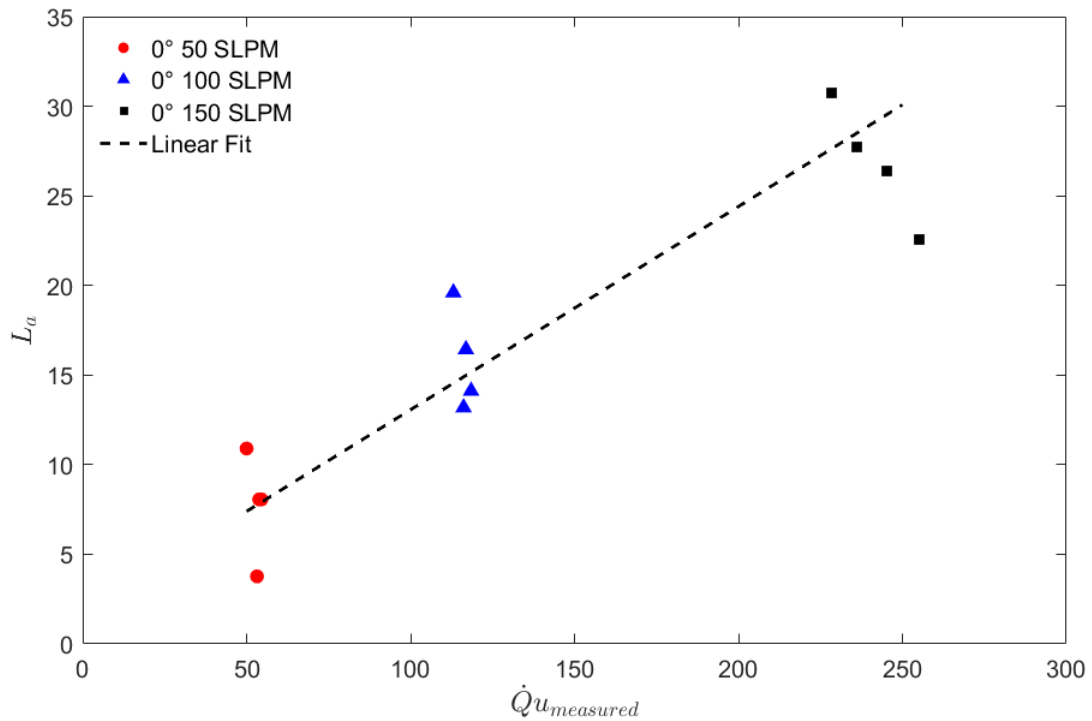


Figure 5.19: $\dot{Q}_{u_{measured}}$ (kW m/s) versus mean attachment length (cm) for a 0.762 m/s forced flow. The legend displays each fire size considered. Each condition contains four different aspect ratios.

The influence of varying aspect ratio of the burner and the heat-release rate per unit area was considered for the 0.762 m/s average attachment length data

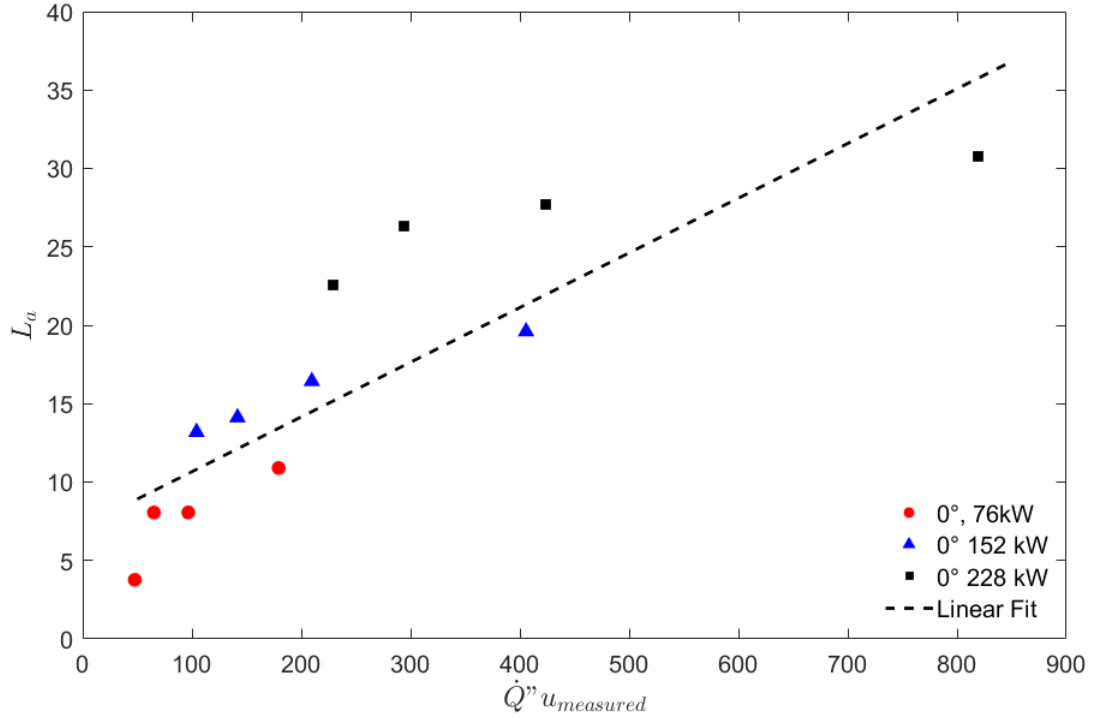


Figure 5.20: $\dot{Q}''u_{measured}$ (kW/m² m/s) versus mean attachment length (cm) for a 0.762 m/s forced flow. The legend displays each fire size considered. Each condition contains four different aspect ratios.

shown in Figure 5.20. Another linear relationship is found, which indicates that for the 0.762 m/s wind speed there is also a relationship between the aspect ratio of the burner and the average attachment length. The linear relationship is given by,

$$L_a = 0.03488\dot{Q}''u_{measured} + 7.173 \quad (5.4)$$

and has an R-squared value of 0.7495 (with L_a given in cm), although the relationship does not seem to follow the same trends as the heat-release rate. While in attached flames the overall heat-release rate is the dominant factor in determining the attachment length, the heat-release rate per unit area also has a relationship.

To summarize the results from the linear fits in this section it seems that for the 0.304 m/s wind speed when the flame is near the threshold for attachment, there is only a linear relationship between the aspect ratio of the burner and the attachment length. While for the 0.762 m/s wind speed, when the flame is attached, there are linear relationships between both aspect ratio and heat-release rate with the attachment length. The combination of forced flow and inclined conditions are then considered in an attempt to determine how these two drivers of flame attachment interact, as they are commonly seen together in wildland fires.

5.3.2 Inclined and Forced Flow

5.3.2.1 Raw Temperature Profile Averages: Combination

To begin the analysis of fires under both wind and inclined conditions downstream average temperature profiles are considered. The only wind speeds considered for angles were the previously used 0.304 m/s and 0.762 m/s tests. Figure 5.21 shows a 72 kW fire with a 15.24 cm \times 183 cm burner and angles ranging from 0° to 30°. This Figure shows a 15.24 cm \times 183 cm burner so it is noted that the 0° case is attached when other burner heat-release rates in this condition would not be. The first observation from this data is the lack of separation depending on angle of incline. It seems that the flame is attached to the surface from the 0° case and has, in comparison to inclined tests alone, insignificant variations downstream. It is also important to note that there appears to be no obvious flame detachment, as the temperature decline is gradual down the length of the thermocouple array.

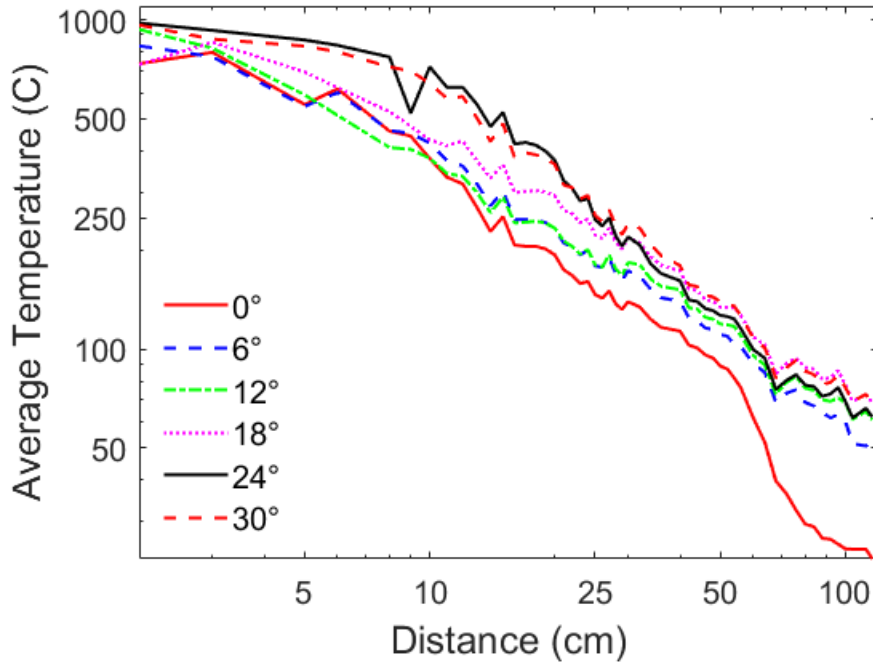


Figure 5.21: Average temperature profiles for a 72 kW fire with a 0.304 m/s forced flow and an aspect ratio of 12

To observe the impact of overall heat-release rate, the average temperature profiles of a 152 kW fire are shown in Figure 5.22. A larger fire size obviously makes a significant difference in the downstream heating measured by the thermocouples for the coupled wind and inclined case. In comparison to the 72 kW fire in Figure 5.21 downstream temperatures in Figure 5.22 temperatures stay near the maximum for most of the array of thermocouples before dropping off rapidly rather than the gradual decline seen down the length of the thermocouple array in Figure 5.21. This indicates a much longer attachment length along the downstream surface. It is also important to note that there is separation between the 0° case and the rest of the angles; this indicates some detachment around 12 cm downstream of the burner. The average temperature profiles from the combined tests show wind and slope and

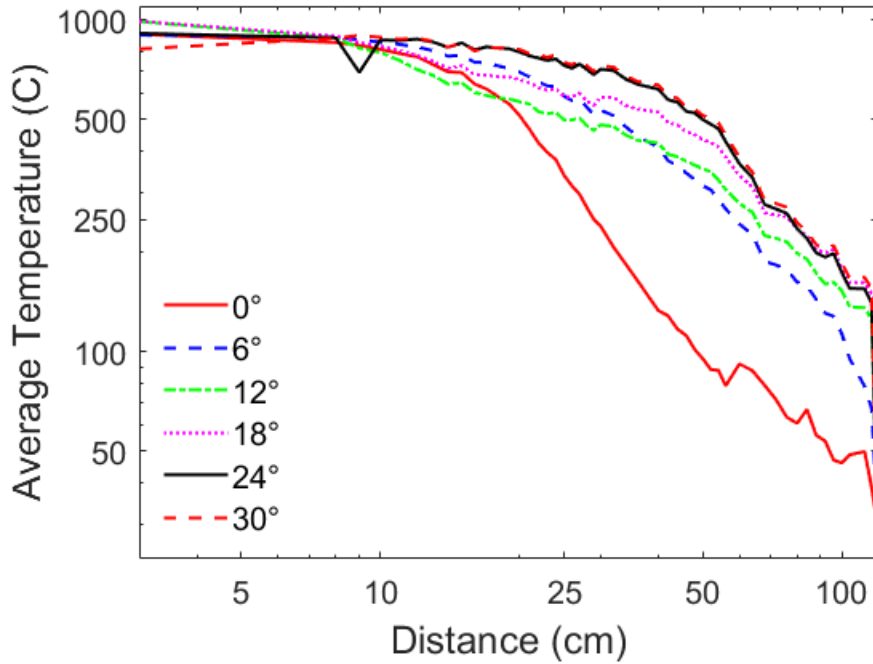


Figure 5.22: Average temperature profiles for a 152 kW fire with a 0.304 m/s forced flow and an aspect ratio of 12

having a compounding effect, causing attachment downstream for all tests, with detachment occurring significantly downstream in the 0 ° case.

5.3.2.2 Instantaneous Temperature Measurements and PDFs: Combination

To observe the impact of a combination of wind and slope on the distribution of attachment lengths, PDFs are compared for the 0.304 m/s wind speed at all fire heat-release rates and a 12 ° incline in Figure 5.23. A different picture of flame behavior comes from the PDFs with the combination of wind and slope. The difference in flame attachment length is obviously dependant upon the overall

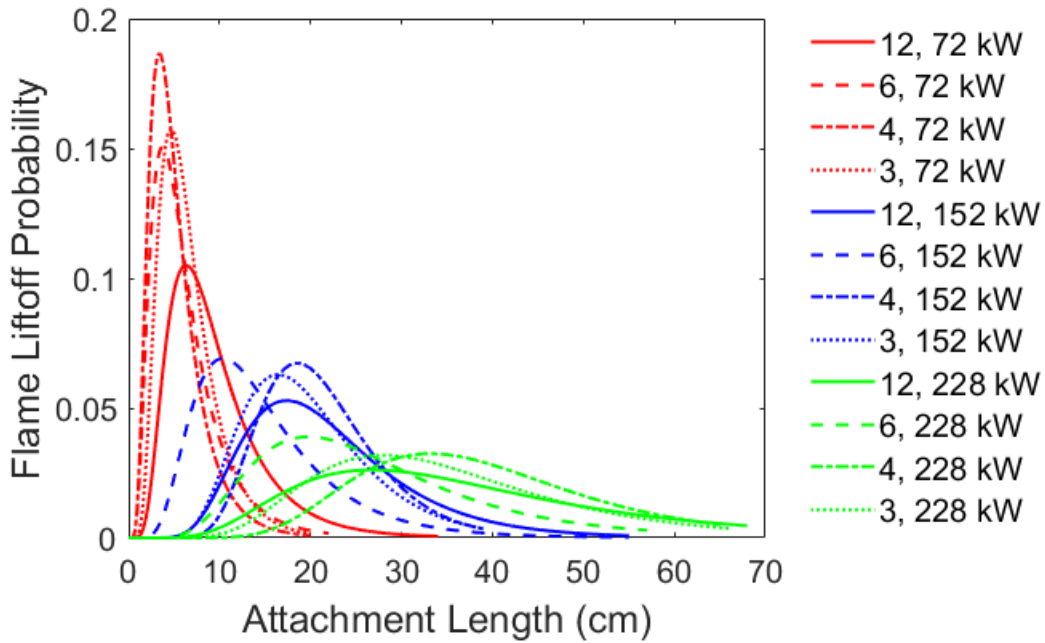


Figure 5.23: PDFs of attachment lengths at 12° for all aspect ratios and heat-release rates with a 0.304 m/s forced flow. Legend displays the aspect ratio and the fire heat-release rate for each test.

fire heat-release rate, indicating an attached flame for the 12° case which was not attached in the ambient inclined scenario. This is not surprising, as it was expected that an additional forced flow would aid in attachment. The average temperature profiles show a very similar relationship for each angle, PDFs are shown for $0^\circ - 30^\circ$ with a 72 kW fire in Figure 5.24.

Figure 5.24 shows an expected result given the temperature profiles in Figure 5.21, it shows that there is less of a difference in flame attachment from varying angles than varying the heat release rates for a fire in a forced flow. This is a significant observation considering that threshold behavior in the inclined case alone

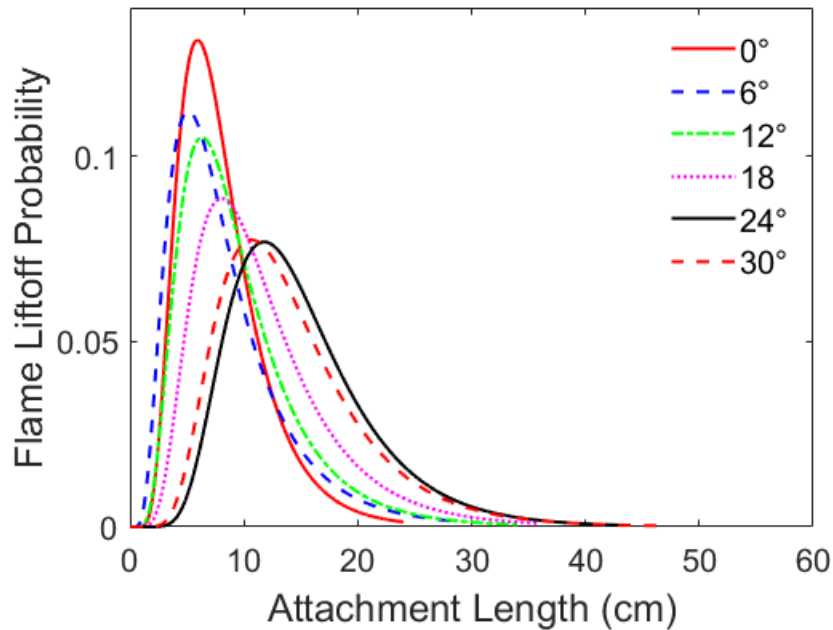


Figure 5.24: PDFs of attachment lengths for a 72 kW fire with an aspect ratio of 12 under a 0.304 m/s forced flow

is strongly dependant upon inclination rather than heat-release rate. This change in behavior is important to note when considering downstream heating.

Figure 5.25 shows again the 0.304 m/s wind speed but at an angle of incline of 18°. The same trend of flow-rate dominating flame attachment is shown as in the 12° case, indicating an attached flame. No significant difference in behavior are observed between the angles of incline in this case, there is a significantly greater attachment length noticed in the 18° case. Although the increase seems to be proportional throughout.

In Figure 5.26 a larger fire heat-release rate of 228 kW is considered again with a 0.304 m/s wind speed at multiple angles of incline. This Figure shows significantly different behavior from Figure 5.24 which has the same wind speed but a different

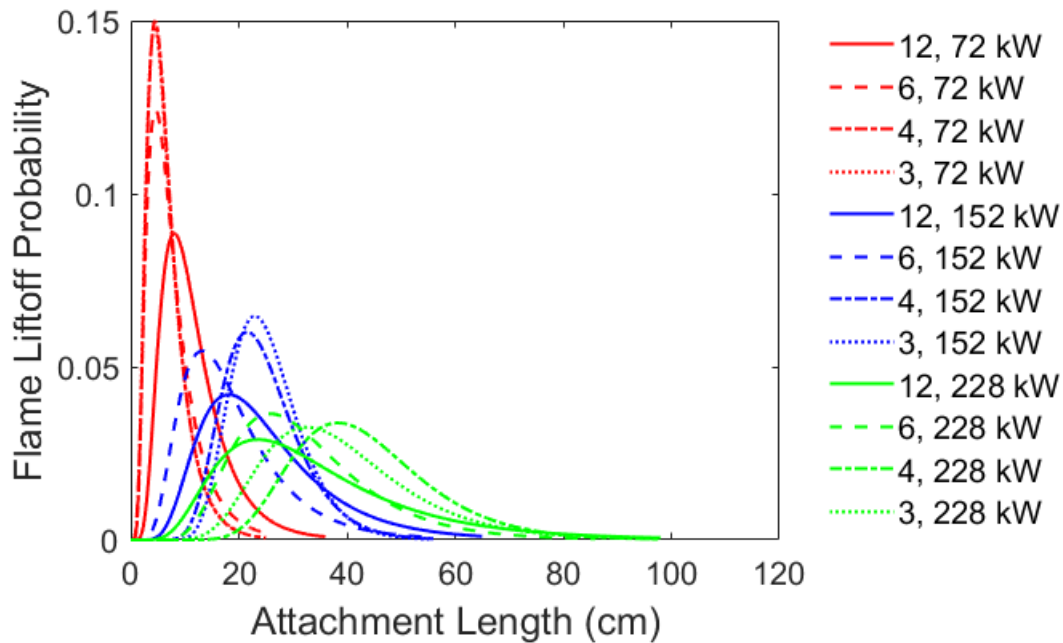


Figure 5.25: PDFs of attachment lengths for all aspect ratios and fire heat-release rates tested under a 0.304 m/s forced flow. Legend displays the aspect ratio and the fire heat-release rate for each test.

flow-rate. Between these two tests, there is significant difference in flame detachment behavior.

The larger fire heat-release rate shows detachment behavior that is not shown with the 72 kW fire. The 0° and 6° cases show transition from a detached flame to an attached flame. An explanation for this detachment behavior in a larger fire heat-release rate rather than a smaller fire heat-release rate is the increased strength of the buoyant plume from the larger heat release coming from a 228 kW fire. The behavior of the the detachment points in Figure 5.27 behave more closely to the detachment points seen in Figure 5.24, as the forced flow momentum overcomes that of the buoyant plume. From these plots there is an obvious relationship between the

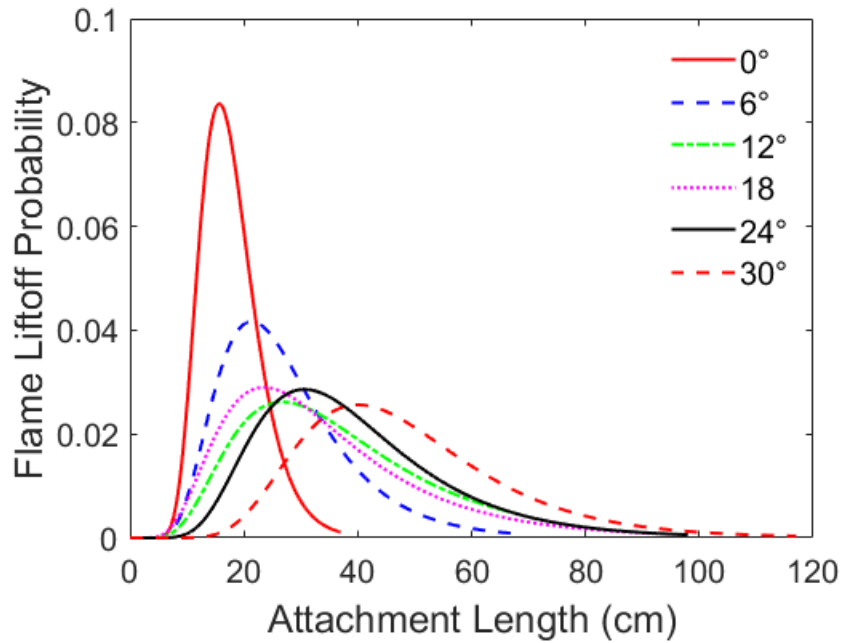


Figure 5.26: PDF of attachment lengths for a 228 kW fire with an aspect ratio of 12 under a 0.304 m/s forced flow

fire heat-release rate and forced flow that determine downstream heating and the location where the flame detaches at multiple angles of incline. This relationship is now explored using average attachment lengths.

Figure 5.27 shows the larger flow rate under a stronger forced flow, with a wind speed of 0.762 m/s.

5.3.3 Average Attachment Length Correlations: Combination

In this section correlations were taken between relevant parameters for combined inclined and forced flow data. To determine the best relationships to correlate data, previous relationships for each individual factor were considered. First the relationship between overall heat-release rate \dot{Q} and the vertical component of buoy-

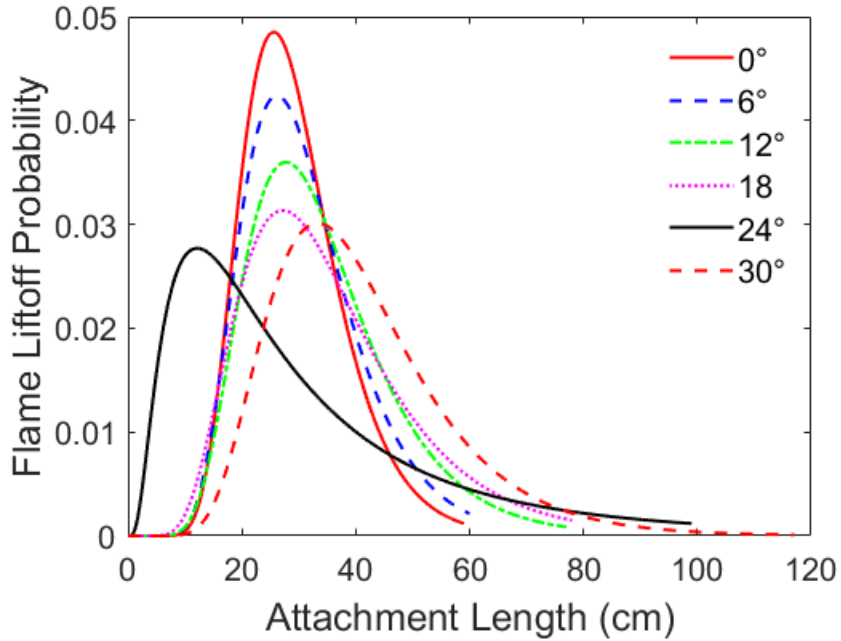


Figure 5.27: PDFs of attachment lengths for a 228 kW fire with a burner aspect ratio of 12 under a forced flow of 0.762 m/s.

ancy $g \sin(\theta)$ were considered as they were the major drivers of flame attachment in the inclined case. For these two parameters, a linear relationship is found,

$$L_a = 0.03565\dot{Q}g \sin(\theta) + 5.078 \quad (5.5)$$

shown in Figure 5.28 (with L_a in cm). This relationship is not as strong as the relationship observed in the inclined case with these parameters; an R-squared value of 0.6813 is found when considering angles of incline from 6° to 30° with a 0.304 m/s forced flow. The influence of the forced flow competing with the buoyant plume has an influence on the downstream attachment length and must be considered in the correlation. The stronger forced flow of 0.726 m/s is also tested to see how the relationship changes. Figure 5.29 shows the same parameters plotted against

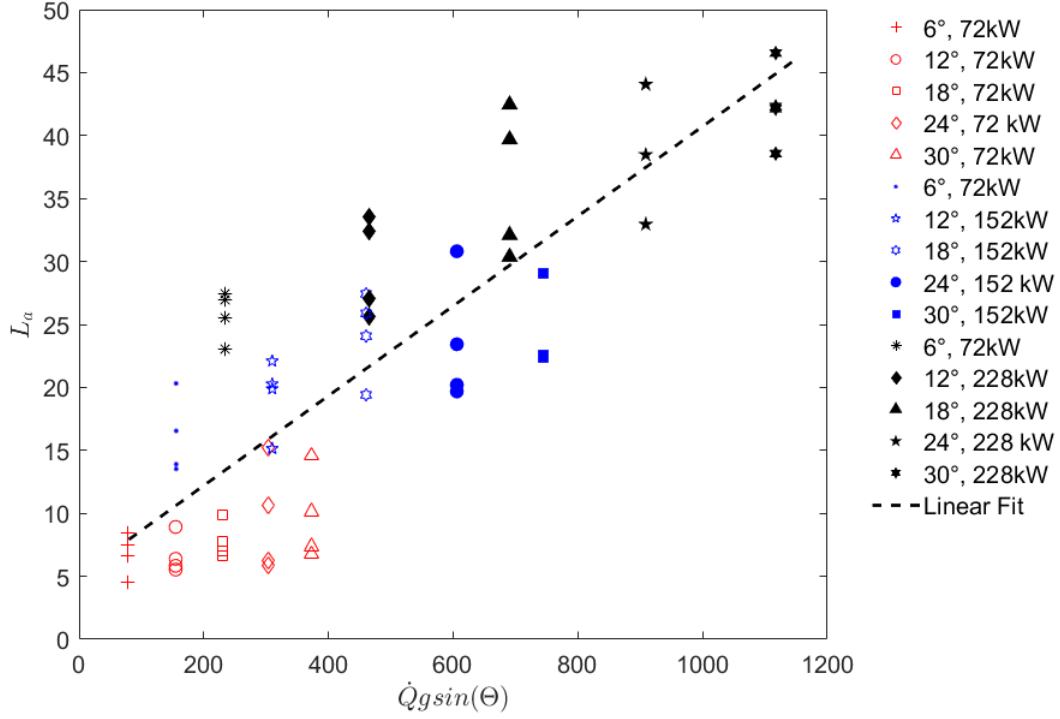


Figure 5.28: $\dot{Q}g \sin(\theta)$ (kW m/s^2) versus mean attachment length (cm) for 0.304 m/s forced flow and inclination from 6° to 30° . The legend displays each angle of incline and fire size considered. Each condition contains four different aspect ratios of attachment length with the 0.726 m/s wind speed. It is shown that the linear relationship of the attachment length to the overall heat release rate \dot{Q} and the vertical component of incline $g \sin(\theta)$ drops further as the force flow velocity is increased with a linear relationship of,

$$L_a = 0.03424\dot{Q}g \sin(\theta) + 6.26 \quad (5.6)$$

shown in figure 5.29, with an R-squared value of 0.617 (with L_a in cm).

The linear relationship observed in the horizontal (0°) cases that included the measured upstream wind speed $u_{measured}$, and the overall heat-release rate \dot{Q} were considered to see if there is a stronger relationship than considering the buoyant

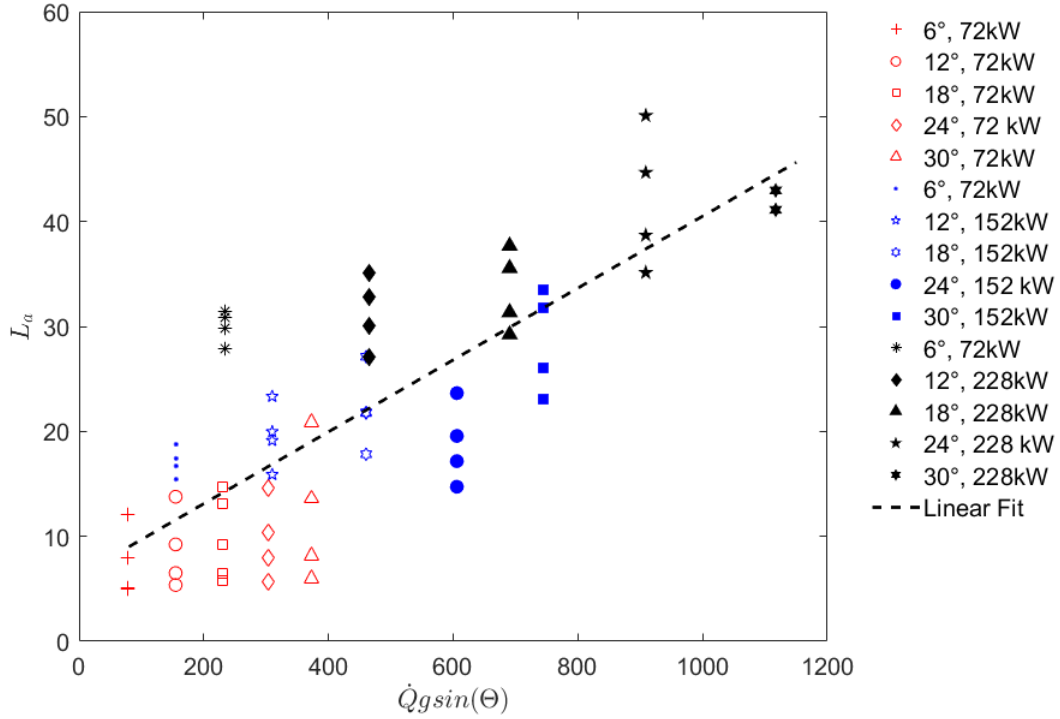


Figure 5.29: $\dot{Q}g \sin(\theta)$ (kW m/s^2) versus mean attachment length (cm) with 0.726 m/s forced flow and inclination from 6° to 30° . The legend displays each angle of incline and fire size considered. Each condition contains four different aspect ratios influence driven by the angle of incline. These parameters are shown in Figure 5.30. There is a drop in the agreement of the measured attachment length and the relationship when the vertical component of gravity is omitted and only the overall heat release rate and measured upstream wind speed are considered. An R-squared value of 0.526 is found for the 0.304 m/s forced flow velocity linear relationship given by,

$$L_a = 0.2229\dot{Q}u_{measured} + 3.98 \quad (5.7)$$

with a slight improvement of the R-squared value for the 0.726 m/s case of 0.566. From these relationships it is obvious that the forced flow velocity plays a role

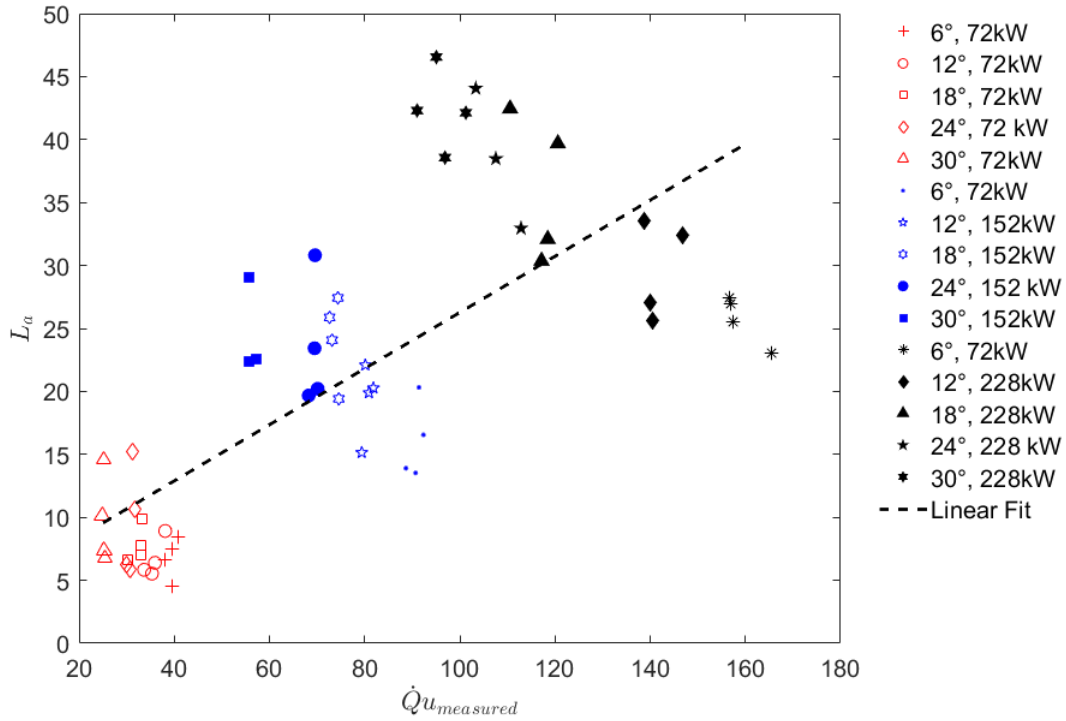


Figure 5.30: $\dot{Q}u_{measured}$ (kW m/s) versus mean attachment length (cm) for 0.304 m/s forced flow and inclination from 6° to 30° . The legend displays each angle of incline and fire size considered. Each condition contains four different aspect ratios in flame attachment, and that role increases as the forced flow velocity increases. Although the drop in agreement from the previous linear relationships indicate the importance of considering the buoyant influence for attachment length.

Next the measured upstream velocity $u_{measured}$, overall heat-release rate \dot{Q} , and the vertical component of gravity $g \sin(\theta)$ are combined in an attempt to account for both the buoyant effects of the plume and the momentum from the forced flow. These parameters and the resulting average attachment lengths are shown in Figure 5.31. There is stronger correlation for these parameters and the attachment length for the combination of inclined and forced flow conditions. A linear relationship

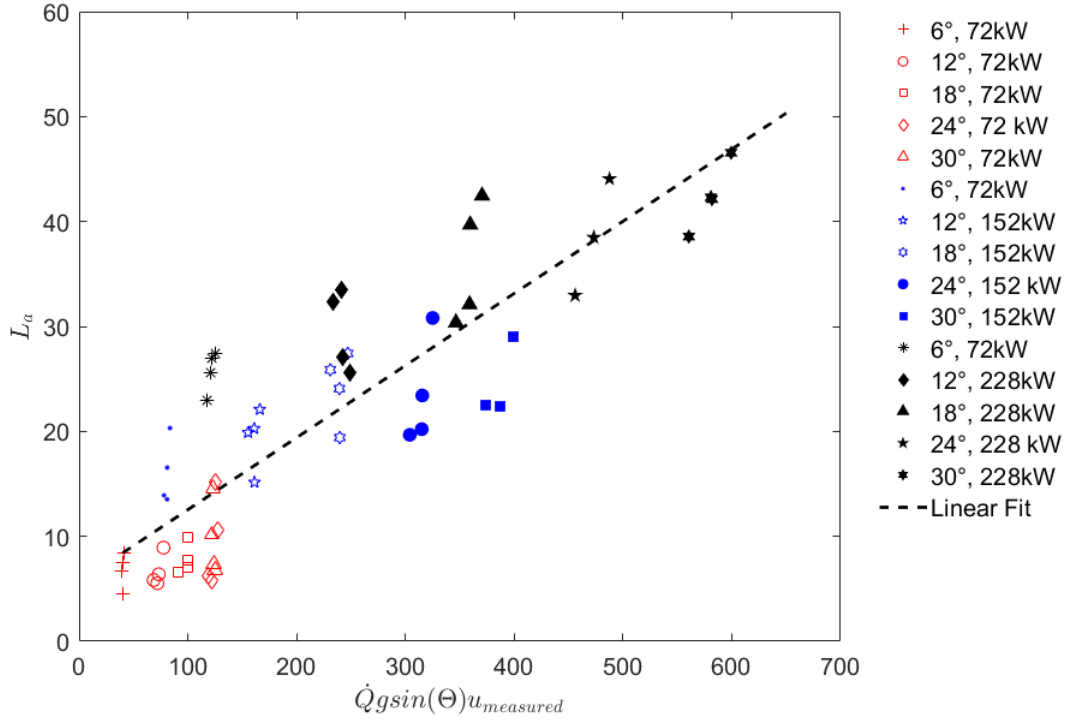


Figure 5.31: $\dot{Q}g \sin(\theta)u_{measured}$ ($\text{kW m}^2/\text{s}^3$) versus mean attachment length (cm) for 0.304 m/s forced flow, inclined from 6° to 30°. The legend displays each angle of incline and fire size considered. Each condition contains four different aspect ratios given by,

$$L_a = 0.0687\dot{Q}g \sin(\theta)u_{measured} + 5.668 \quad (5.8)$$

an R-squared value of 0.7499 (with L_a given in cm) is found for this relationship indicating a stronger correlation. The same relationship is plotted for the 0.762 m/s wind speed and is shown in Figure 5.32. As the wind speed is increased the correlation gets worse with an R-squared value of 0.667 and an equation,

$$L_a = 0.04372\dot{Q}g \sin(\theta)u_{measured} + 6.66 \quad (5.9)$$

although a stronger correlation is shown from the previous attempt a correlating the 0.762 m/s wind speed with the buoyancy component omitted.

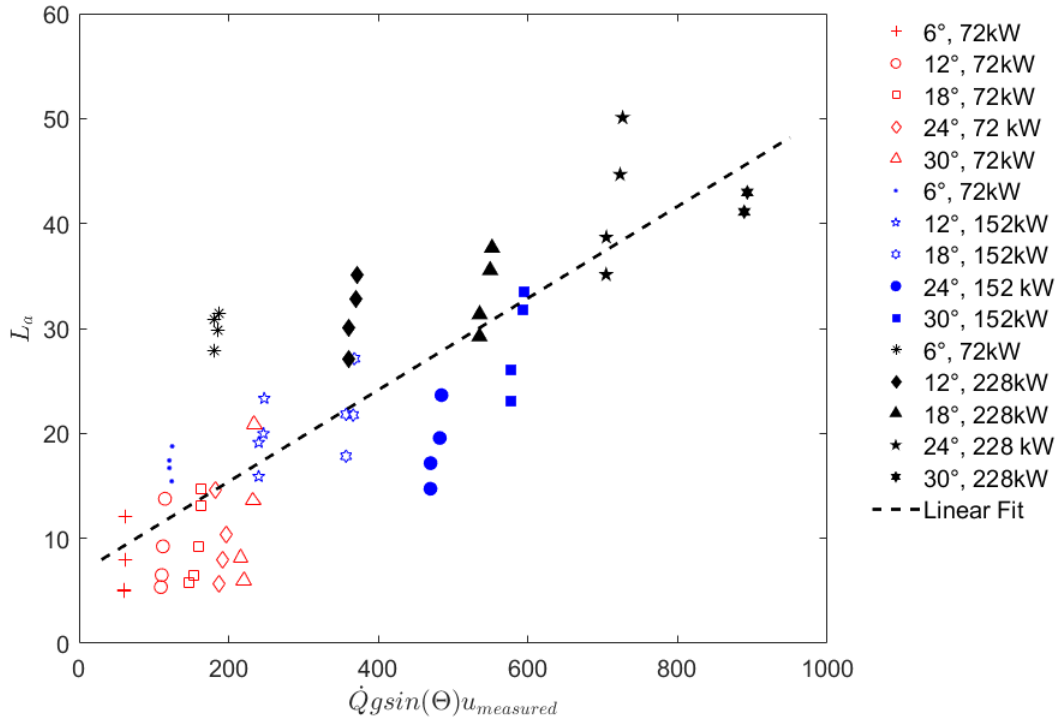


Figure 5.32: $\dot{Q}g\sin(\theta)u_{measured}$ (kW m²/s³) versus mean attachment length (cm) for 0.762 m/s forced flow and inclination from 6° to 30°. The legend displays each angle of incline and fire size considered. Each condition contains four different aspect ratios.

In order to further investigate the impact of varying the aspect ratio of the burner, individual aspect ratios were considered for the $\dot{Q}g\sin(\theta)u_{measured}$ relationship. An aspect ratio of 12 is considered first in Figure 5.33. Considering only a single aspect ratio significantly improves the linear relationship in the correlation between mean attachment length, heat-release rate, incline, and measured tunnel velocity. When a linear fit is applied an R-squared value of 0.8365 (with L_a given in cm) is found as opposed to 0.6813 when all aspect ratios are considered. The linear

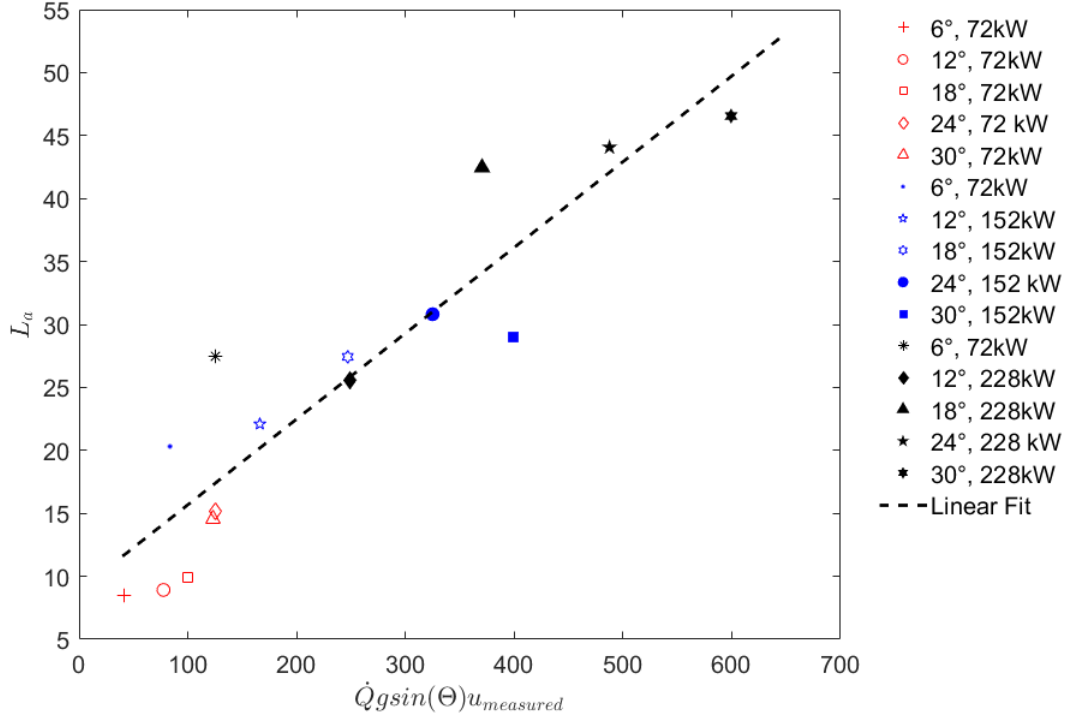


Figure 5.33: $\dot{Q}g\sin(\theta)u_{measured}$ ($\text{kW m}^2/\text{s}^3$) versus mean attachment length (cm) for a burner aspect ratio of 12, 0.304 m/s forced flow and inclination from 6° to 30°. The legend displays each angle of incline and fire size considered.

fit is given by the equation,

$$L_a = 0.0681\dot{Q}g\sin(\theta)u_{measured} + 8.87 \quad (5.10)$$

To further investigate the impact of aspect ratio, each aspect ratio was fit individually. It was observed that as the aspect ratio was decreased by increasing the burner width, the linear relationship between mean attachment length and heat-release rate, incline, and measured tunnel velocity dropped. Figure 5.34 shows the relationship for an aspect ratio of 3. The linear fit is given by the equation,

$$L_a = 0.06005\dot{Q}g\sin(\theta)u_{measured} + 6.256 \quad (5.11)$$

and has a R-squared value of 0.7063 (with L_a given in cm). This trend indicates

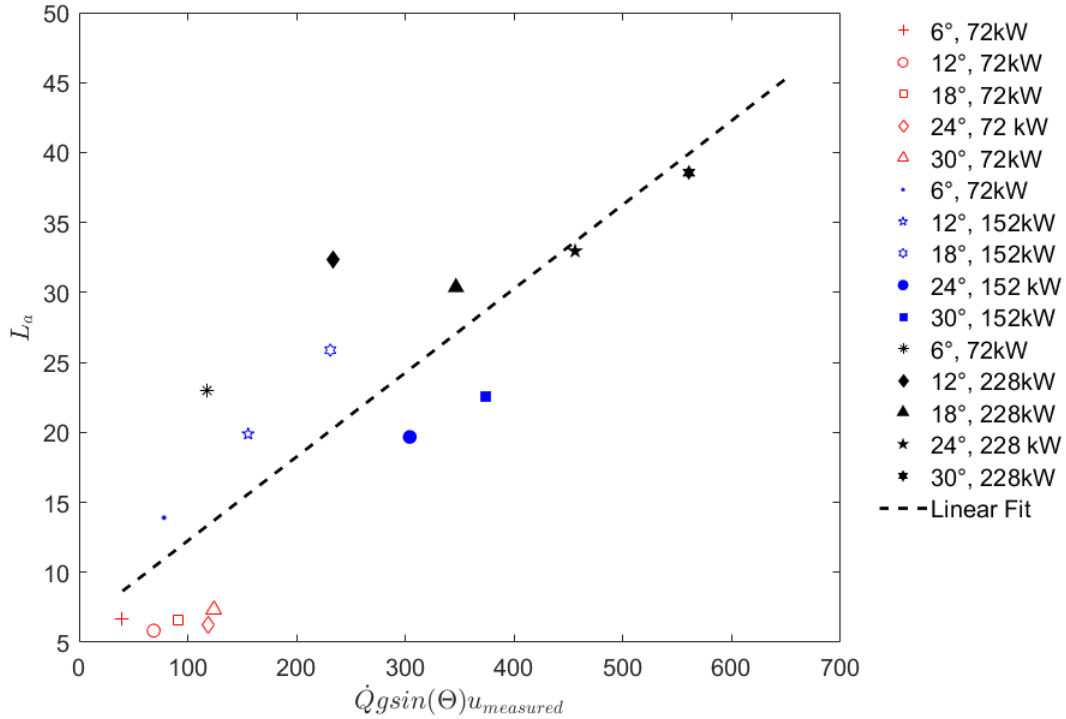


Figure 5.34: $\dot{Q}g\sin(\theta)u_{measured}$ ($\text{kW m}^2/\text{s}^3$) versus mean attachment length (cm) for a burner aspect ratio of 3, 0.304 m/s forced flow and inclination from 6° to 30°. The legend displays each angle of incline and fire size considered.

that as burner depth increases, the relationship between attachment length and heat-release rate, incline, and measured tunnel velocity decreases as aspect ratio decreases. This could be due to the fact that the lower aspect ratios represent flames that are no longer linear, approaching a point or area source as the width of the burner is increased.

Methods have been used in previous studies to relate attachment length to the competition between the buoyant force of the flame and the momentum force of a forced flow. The Richardson number utilized by Tang et al. and shown in

Equation 2.3 [7], a mixed convection relationship from Mao et al. [32], and the Froude number used by Tang et al. [8] were used to attempt to fit a combination of the inclined and forced flow data. None of these dimensionless quantities formed a visible relationship with the measured attachment length in this study. Byram's convective number was also considered for cases with forced flow and no incline, as there is no representation for inclination in the existing formulation. Measured upstream velocities and average tunnel velocities were both considered as U_∞ but no relationship with attachment length was observed. It is interesting to observe that the Richardson number results in a $1/U^2$ and Byram's number 2.4 a $1/U^3$ relationship with velocity, while a linear relationship with velocity is ultimately shown to best fit with flame attachment length later.

Although the desire to use a dimensionless quantity to describe the linear relationships seen with attachment length did inspire the creation of a modified Reynolds number. The Reynolds number is a dimensionless number that relates inertial forces to viscous forces and is classically used in fluid mechanics to predict flow patterns, and indicate whether a flow is laminar or turbulent. The Reynolds number is defined as

$$Re = \frac{vl}{\nu}, \quad (5.12)$$

where v is the velocity of the flow, l is a characteristic length, and ν is the kinematic viscosity of the fluid. In order to account for both the external wind-driven flow and fire-induced buoyant flow, the velocity term will be modified. The velocity of the incoming flow, measured upstream of the burner is first used. Because this flow mostly

represents the oncoming flow and not that generated by the buoyancy of the flame, an additional term was added. The characteristic center-line velocity generated by a buoyant point-source presented in *Scaling Applications in Fire Research* [40],

$$V = \sqrt{g} \left(\frac{\dot{Q}}{\rho_0 \sqrt{g} c_p T_0} \right)^{1/5} \quad (5.13)$$

This equation was then modified further by the addition of a $\tan(\theta)$ to the gravity term to account for the flow generated in plane with in inclined surface. If the two velocities are combined, a modified Reynolds number equation is formed that accounts for both in-plane flows generated by the buoyant plume and the forced flow,

$$Re^* = \frac{(u_{measured} + \sqrt{g \tan(\theta)} \left(\frac{\dot{Q}}{\rho_0 \sqrt{g \tan(\theta)} c_p T_0} \right)^{1/5}) l}{\nu}. \quad (5.14)$$

this modified Reynolds Re^* number plotted against measured attachment length L_a is shown in figure 5.35. When all the combined forced flow and inclined data are correlated with the modified Reynolds number,

$$L_a = 6.25 \times 10^{-6} Re^* - 0.3091 \quad (5.15)$$

an R-squared value of 0.739 is found (with L_a in m). Attachment lengths for inclined and the combination of inclined and forced flow cases are represented well by the relationship presented in the modified Reynolds number. In the modified Reynolds number, the heat-release rate, measured incoming velocity, angle of inclination, and the plume velocity in plane with the incline are considered.

Previously, attachment length was correlated with heat-release rate, angle of inclination, and measured incoming velocity which worked well for the combination

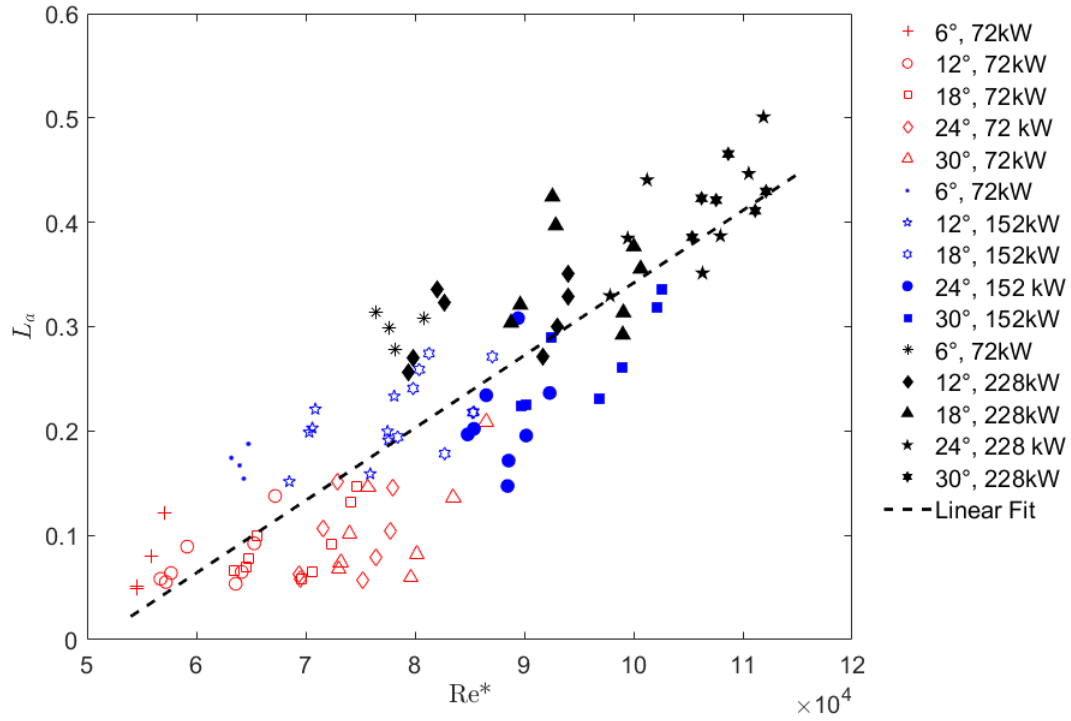


Figure 5.35: Re^* versus mean attachment length (m) for 0.304 m/s and 0.762 m/s forced flow with inclinations from 6° to 30°. The legend displays each angle of incline and fire size considered, each condition contains four different aspect ratios.

of incline and forced flow and produced linear correlations with R-squared values of 0.667, and 0.7499 for the 0.762 m/s and 0.304 m/s cases. The modified Reynolds number can combine these two wind speeds and still produce a linear relationship with a comparable R-squared value of 0.739. The intention with the development of this modified Reynolds number was the creation of a single variable that has a linear relationship with attachment length for a variety of inclines and wind speeds that can be used to predict downstream fire behavior and therefore heating. The applicability of this modified Reynolds number is tested with the addition of incline data in the absence of a forced flow shown in Figure 5.36. It is found that the linear

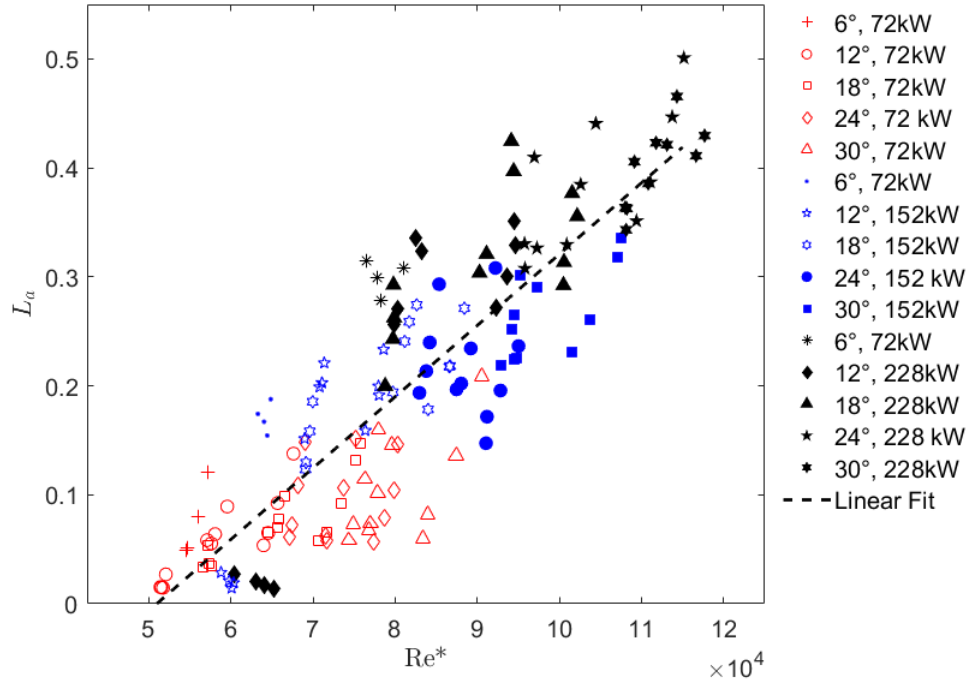


Figure 5.36: Re^* versus mean attachment length (m) correlation for 0 m/s, 0.304 m/s and 0.762 m/s forced flow with inclinations from 6° to 30° . The legend displays each angle of incline and fire size considered. Each condition contains four different aspect ratios.

relationship still exists given by the equation,

$$L_a = 6.545 \times 10^{-6} Re^* - 0.3337 \quad (5.16)$$

with an R-squared value of 0.7625 (with L_a in m). The improvement in the goodness of fit was unexpected with the addition of inclination without forced flow data. This result indicates that this modified Reynolds number may be useful in describing flame attachment under a variety of parameters.

In order to make the correlation non-dimensional and allow for it to be scaled to larger fires, the attachment length is divided by the characteristic length of the

Reynolds number, which is the length of the leading edge L_{LE} plus the attachment length L_a shown in Figure 5.37. A linear trend is shown given by the equation,

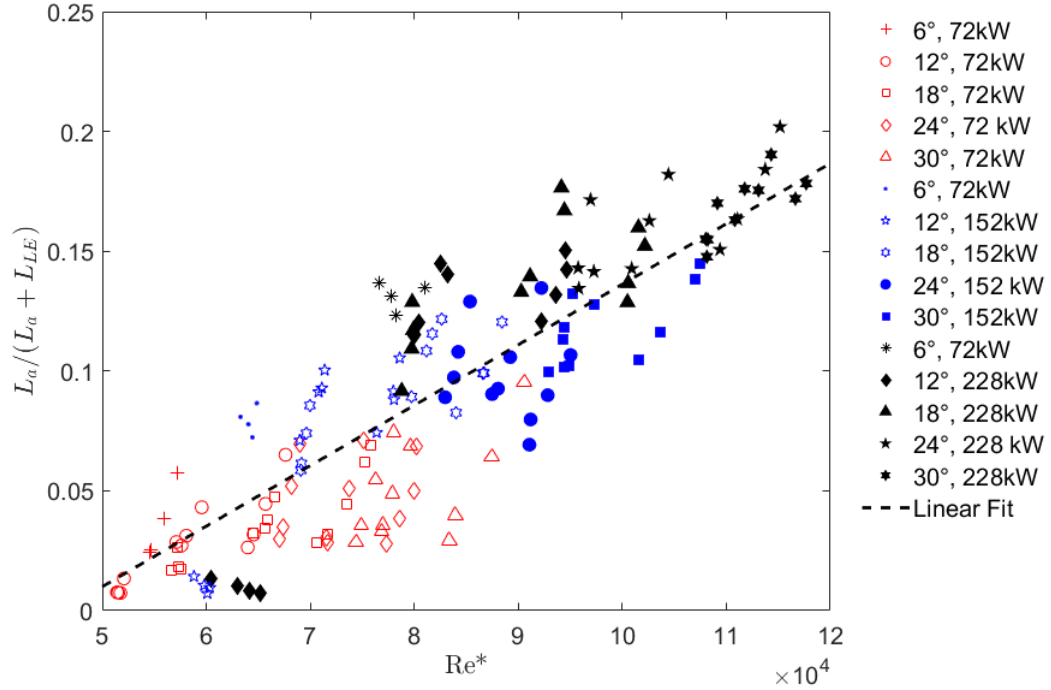


Figure 5.37: Re^* versus mean attachment length normalized by the length of the leading edge plus the mean attachment length. Correlation for 0 m/s, 0.304 m/s and 0.762 m/s forced flow with inclinations from 6° to 30°. The legend displays each angle of incline and fire size considered, each condition contains four different aspect ratios.

$$L_a/(L_a - L_{LE}) = 2.699 \times 10^{-6} Re^* - 0.1314 \quad (5.17)$$

with an R-squared value of 0.76.

This relationship now is non-dimensional but does not have the ability to predict flame attachment lengths for given conditions due to the modified Reynolds number dependence of the measured attachment length. In order to overcome this,

the characteristic length of the modified Reynolds number is modified to the length of the leading edge, from the tip of the experimental apparatus to the beginning of the burner (1.37 m). The attachment length is also normalized by the leading edge to make the relationship non-dimensional. The correlation is shown in Figure 5.38.

The linear trend is shown given by the equation,

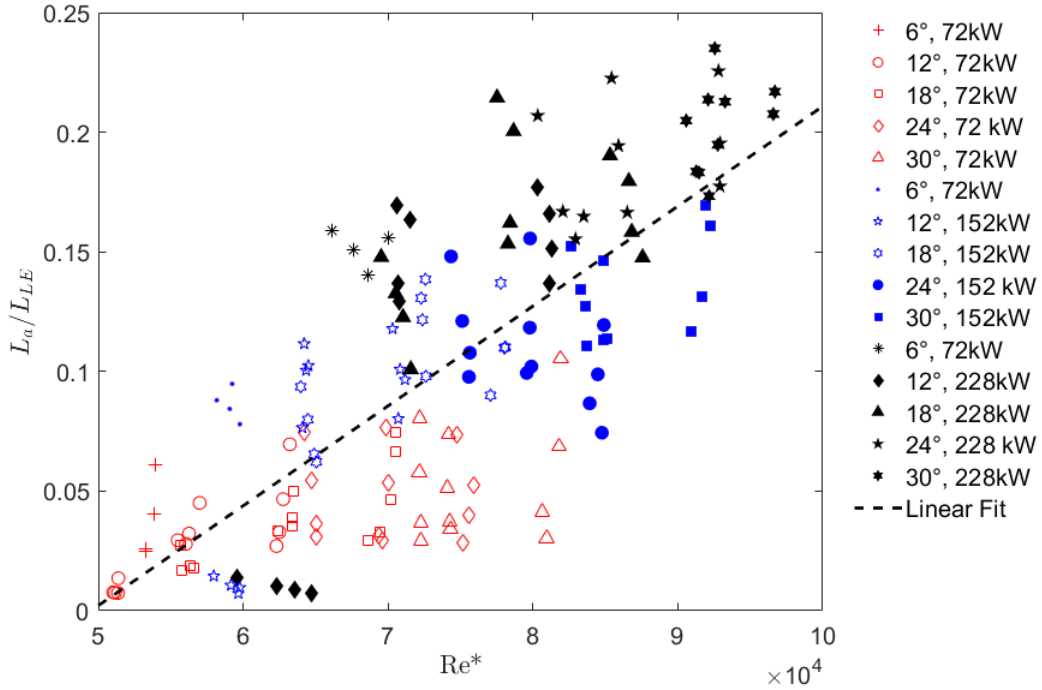


Figure 5.38: Re^* versus mean attachment length (m) correlation for 0 m/s, 0.304 m/s and 0.762 m/s forced flow with inclinations from 6° to 30°. The legend displays each angle of incline and fire size considered, each condition contains four different aspect ratios.

$$L_a/L_E = 4.173 \times 10^{-6} Re^* - 0.2065 \quad (5.18)$$

with an R-squared value of 0.588. The R-squared value significantly drops for this correlation, this is expected as the mean attachment length is removed from the

characteristic length. Despite the decrease in the R-squared value, this indicates that the modified Reynolds number can be used to predict attachment lengths for flames under the influence of the parameters considered in this study. More work to refine this relationship is necessary but highlights the possibility of a correlation between flames influenced by both forced flows and inclined surfaces.

Chapter 6: Conclusions and Future Work

6.1 Conclusions

First, qualitative observations of fire and plume behavior including average temperature profiles were used to observe the impact of inclination and fire heat-release rate on a relatively small-scale propane burner on an inclined surface. Two regimes with threshold behavior for transition were observed, one where the flame still remained fairly vertical and another where the flame attaches along the surface more akin to a boundary-layer. The transition between these two states, determined via the distance along the surface for which the flame attached, was found to be influenced by both the angle of incline of the test surface and the fire heat-release rate. Shadowgrams were taken perpendicular to the apparatus which revealed the flow structure, indicating a change in entrainment behavior between 10° and 20° . Temperature measurements along the downstream surface confirmed this result, indicating a threshold for flame attachment between 14° and 18° . The threshold angle of attachment was also observed to decrease with an increase in heat-release rate. These results inspired the construction of a relatively large-scale experimental apparatus to investigate a wider variety of influences on these behaviors.

A similar but larger-scale apparatus was then used to further study the relationship between the fire heat-release rate and aspect ratio with the surface inclination and ambient forced flow, made possibly by placing the new apparatus within a large wind tunnel. Here, instantaneous temperature measurements were used to capture the location of the flame close to the downstream surface over time. This provided both time-averaged attachment lengths as well as a probabilistic representation of the flame location over sloped surfaces. PDF fits were used to investigate the variance in the flame attachment location under each condition and showed a significant increase in variation with an increase in flame attachment length. The intermittent heating observed may have an impact on ignition times and therefore spread rates, especially in fine fuels commonly seen in wildland fire. Time-averaged attachment lengths were used to correlate attachment length data with the varied parameters considered in this study.

The threshold for attachment on the larger-scale apparatus was again observed to occur between 12° and 18° , with the heat-release rate drastically increasing the attachment length for the attached flames but having little influence on attachment length for unattached flames. Aspect ratio is similarly shown not to have a large impact on flame attachment unless the flame is near the threshold of attachment. Near this threshold point, the aspect ratio drives the flame attachment length. After flames have attached, the attachment length is dependant only on the heat-release rate. In order to further investigate fire behavior, instantaneous temperature profiles were considered.

Results suggest that future correlations of flame behavior should be separated into attached and unattached regimes because the behavior that is most important for flame spread, downstream heating, is governed by different phenomena in these regimes. For an unattached regime, only a small length downstream of the burner is heated. As the flow starts to attach, the aspect ratio of the burner becomes incredibly important, possibly playing a role in this transition which is not seen in correlations of fully unattached or fully attached regimes. Finally, in the fully-attached regime the heat-release rate governs the length over which heating occurs, necessitating understanding of the burning regime upstream of fire spread.

6.2 Future Work

The angle of incline, and somewhat the external flow, is critical to determine the onset of transition and therefore must be included in any models for fire spread. What underlies all of this work is the need to accurately predict the transition between attached and unattached flames. Unfortunately this was not possible in this apparatus due to a low angle resolution. In the future, tests with more refined angles beyond the 12° - 18° resolution found in this study should be considered. A more universal, non-dimensional approach should also be developed so that these results can be scaled to larger fires in the future.

The trends observed in data from these experiments need further analysis before it can be translated into new physical understanding or a model that can be applied in the prediction of wildland fire behavior. Thermocouple measurements

did not allow for comparison with similar studies that considered downstream heat flux along the fuel surface in forced flow conditions. A comparison of heat flux, thermocouple, and visual measurements should be considered to interrelate various measurements for inclined, forced flow, and combined conditions in order to make comparisons with previous studies. Heat flux measurements would also be useful to compare with measured attachment lengths in order to better identify the location of the flame and the extent of downstream heating. Using high frequency gauges, intermittent heating from the flame could also be more closely analyzed, determining how the frequency of pulsations of the flame are impacted by the inclined, forced flow, and combined conditions as they have been in forced flow conditions in [3, 7, 8]. Video measurements for inclined, forced flow, and the combination of the two are needed to determine flame length and to compare with thermocouple measurements taken with this study. The video comparison is also necessary to carefully identify whether temperature fluctuations experienced in each situation are due to the heated plume or flame contact. Temperature measurements using thermocouples with a larger bead diameter to determine convective versus radiative heating in each configuration would also be useful to understand how components of heat transfer to downstream fuels is affected as flame location changes.

The next step from this work is to conduct similar experiments at a higher resolution of inclination and wind speed to fully understand the observed flame threshold. The threshold was shown to be dependant on a combination of parameters. It is recommended that intermittent angles closer to the observed threshold ($12^\circ - 18^\circ$) with all of the considered burner characteristics, wind speeds, and the

combination of both be studied carefully with a resolution of about 1° . These tests should also be run repeatedly as well, which was not possible in this study due to the time constraints in collecting data. The repeatably of these transitions in attachment are unknown.

A.1 Attachment Length PDFs

In this section, different measured attachment lengths are shown binned alongside PDF fits to show how log-normal fits represented attachment data from the different conditions considered. Figures 1 to 10 show these fits over a series of different burner size and heat-release rates.

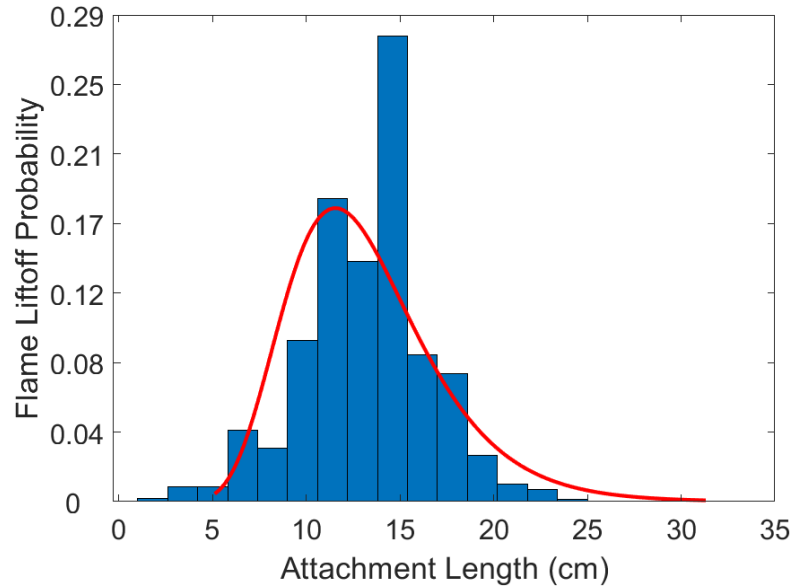


Figure 1: 45 cm \times 183 cm burner (aspect ratio of 4) with a 152 kW fire at 18° and no forced flow

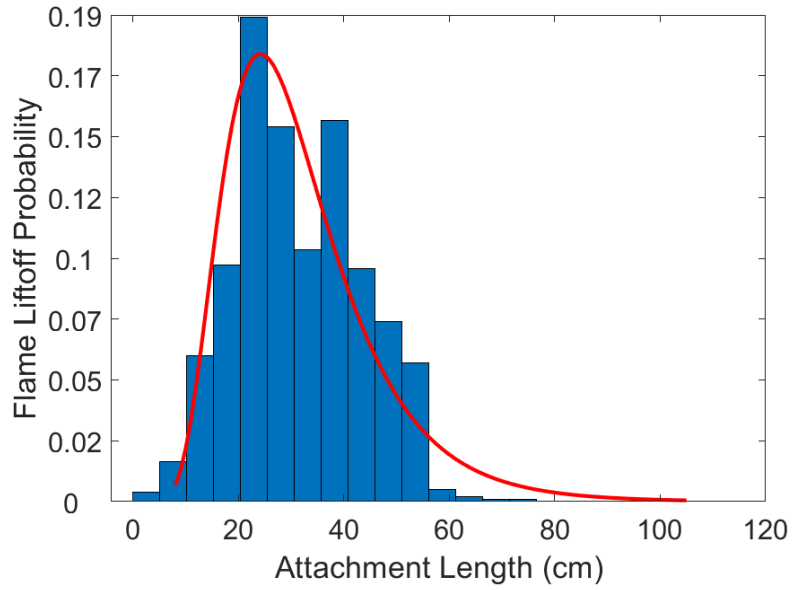


Figure 2: 45 cm × 183 cm burner (aspect ratio of 4) with a 228 kW fire at 24° and no forced flow

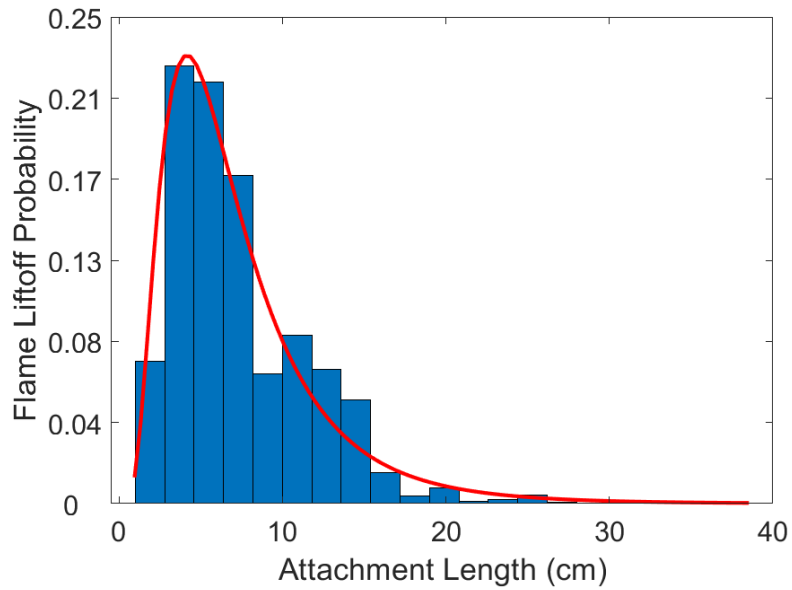


Figure 3: 45 cm × 183 cm burner (aspect ratio of 4) with a 72 kW fire at 30° and no forced flow

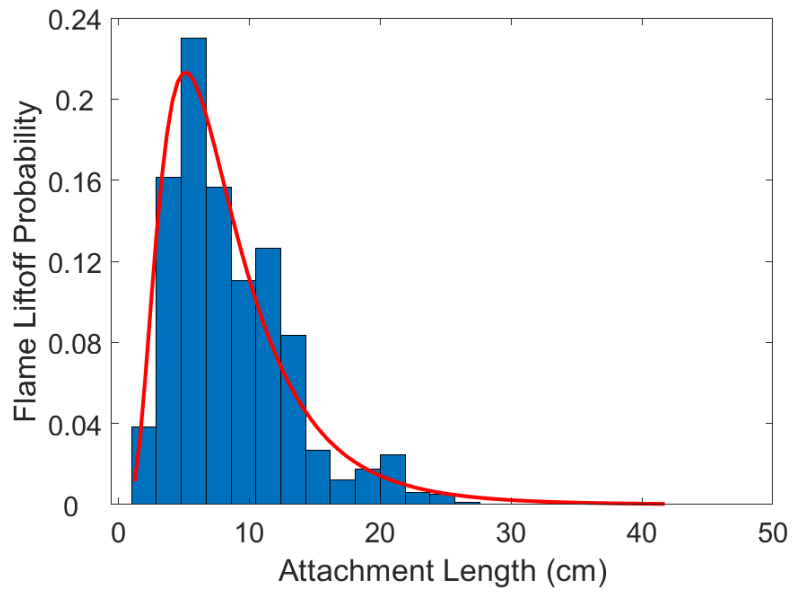


Figure 4: 15 cm \times 183 cm burner (aspect ratio of 12) with a 72 kW fire at 6° and with a 0.304 m/s forced flow

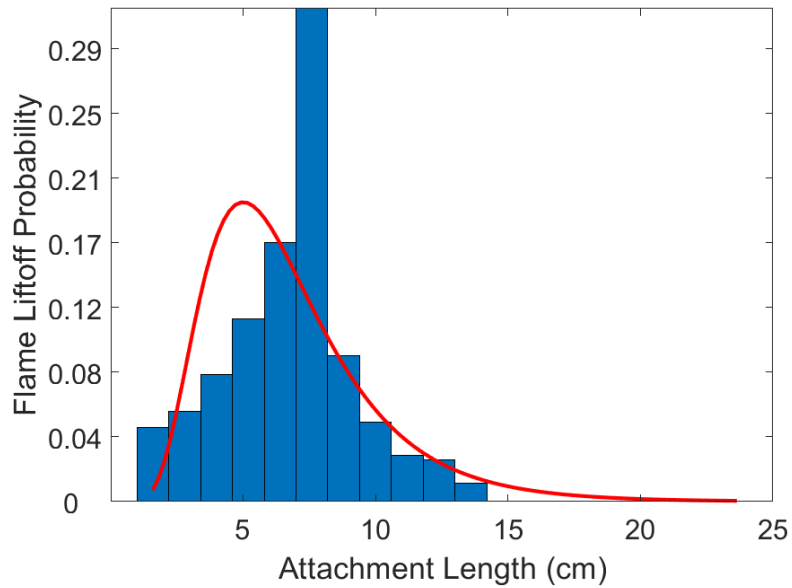


Figure 5: 61 cm \times 183 cm burner (aspect ratio of 3) with a 72 kW fire at 6° and with a 0.304 m/s forced flow

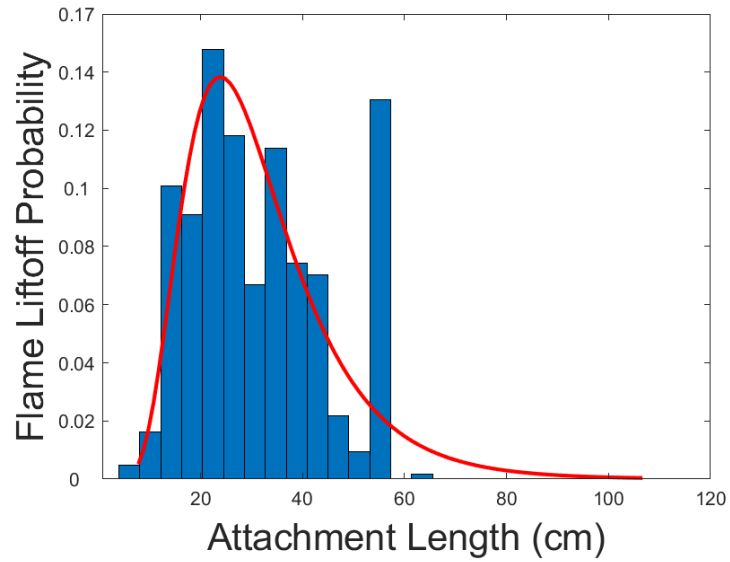


Figure 6: 15 cm × 183 cm burner (aspect ratio of 12) with a 152 kW fire at 30° and with a 0.304 m/s forced flow

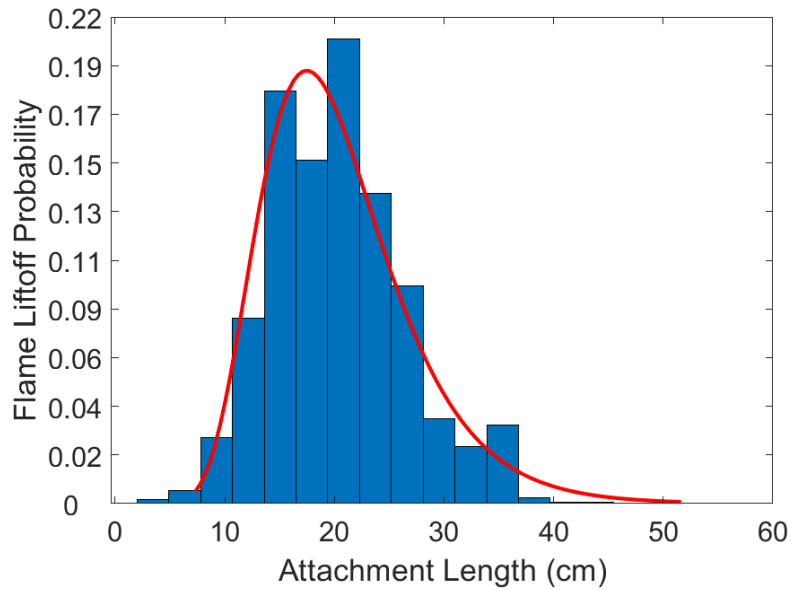


Figure 7: 15 cm × 183 cm burner (aspect ratio of 12) with a 152 kW fire at 0° and with a 0.762 m/s forced flow

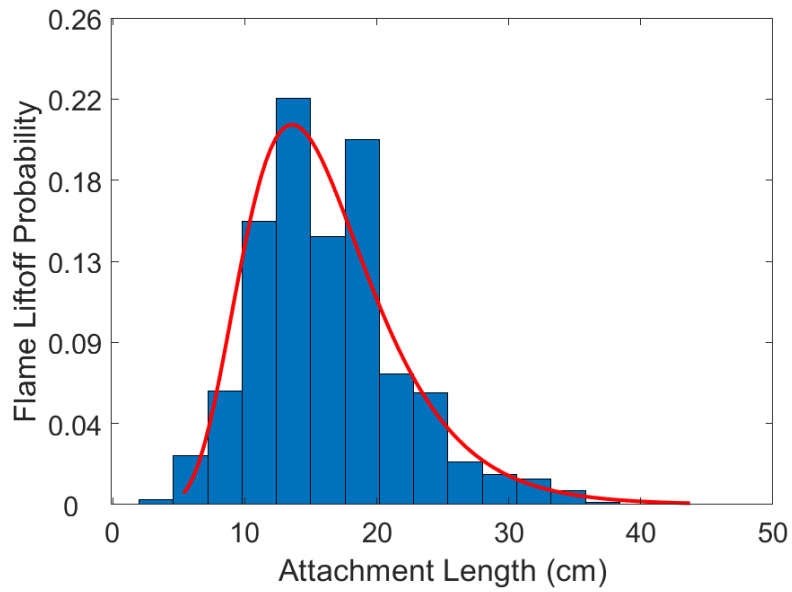


Figure 8: 30 cm × 183 cm burner (aspect ratio of 6) with a 152 kW fire at 0° and with a 0.762 m/s forced flow

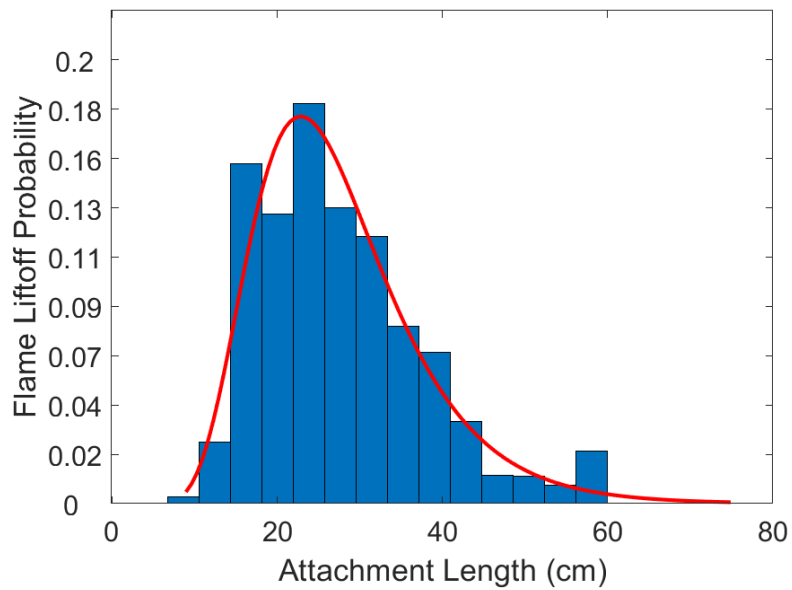


Figure 9: 15 cm × 183 cm burner (aspect ratio of 12) with a 152 kW fire at 18° and with a 0.762 m/s forced flow

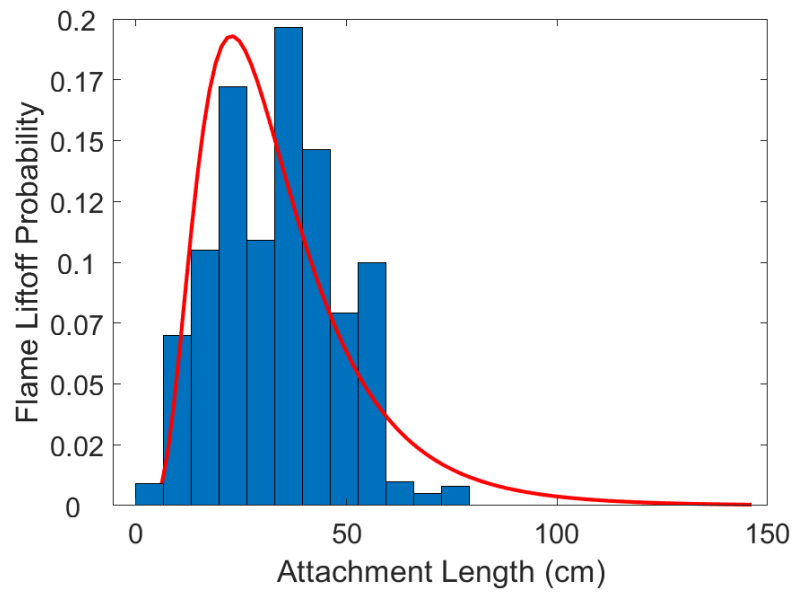


Figure 10: 61 cm \times 183 cm burner (aspect ratio of 3) with a 228 kW fire at 30° and with a 0.762 m/s forced flow

A.2 Small Scale Average Temperature Profiles

In this section, results from the small-scale tilt table measurements are shown that were omitted from the results section due to the use of the log-log scale to demonstrate the location of flame lift off. Figures 11 to 13 contain heat-release rates of 7.6, 9.88 and 12.16 kW and have inclination varying from 12° to 28°.

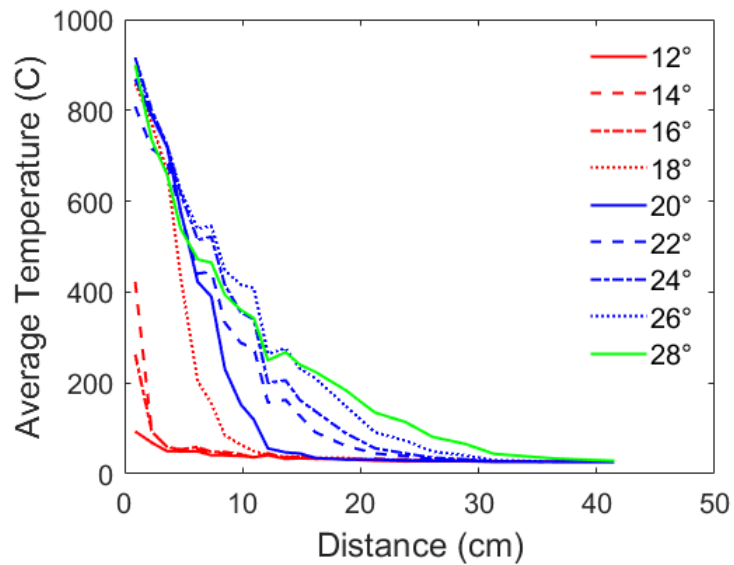


Figure 11: Average temperature profiles recorded downstream of a 7.6 kW fire from 9.2×50.2 cm burner

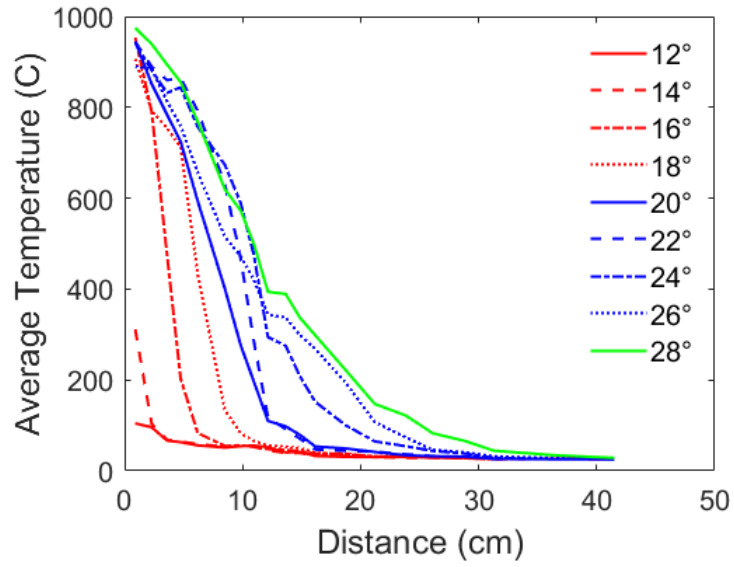


Figure 12: Average temperature profiles recorded downstream of a 9.88 kW fire from 9.2×50.2 cm burner

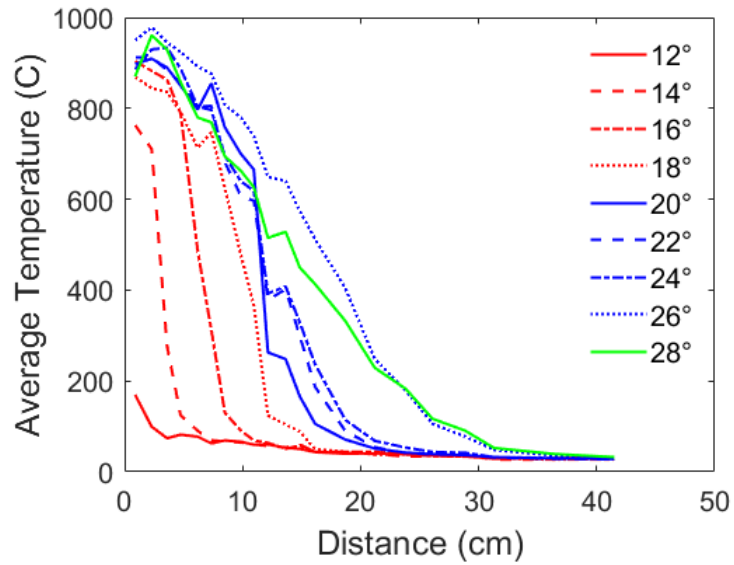


Figure 13: Average temperature profiles recorded downstream of a 12.16 kW fire from 9.2×50.2 cm burner

A.3 Large Scale Average Temperature Profiles: Incline

In this section, figures from the large-scale tilt table under the influence of inclination alone are shown. Figures 14 to 21 contain heat-release rates of 76, 152 and 228 kW and have inclination varying from 12° to 30°.

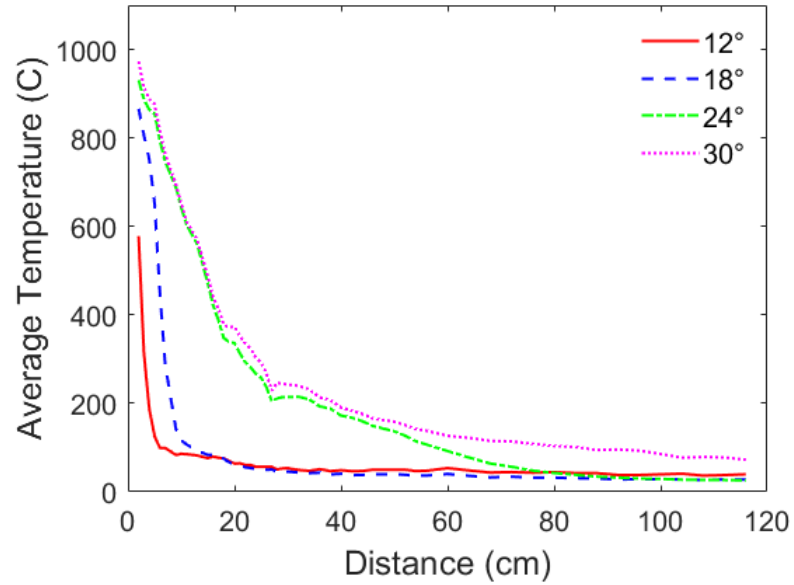


Figure 14: Average temperature profiles recorded downstream of a 76 kW fire from a 15.24 cm × 183 cm burner

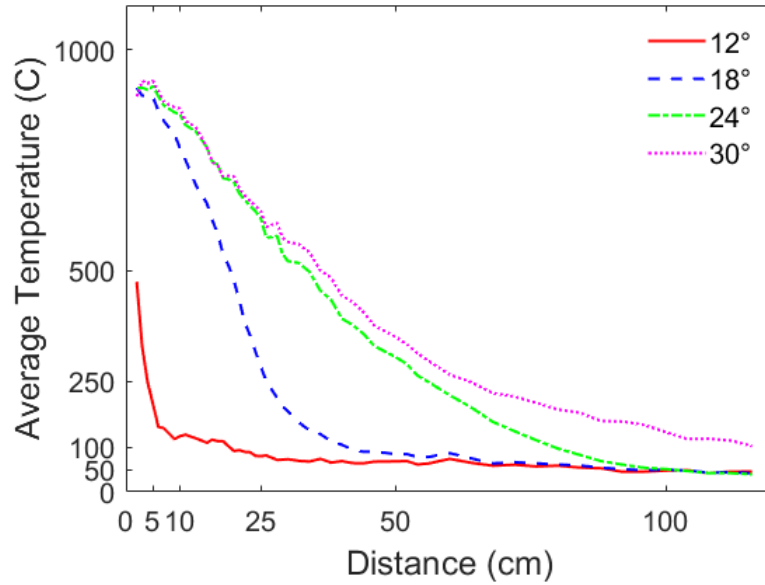


Figure 15: Average temperature Profiles recorded downstream of a 152 kW fire from a 15.24 cm × 183 cm burner

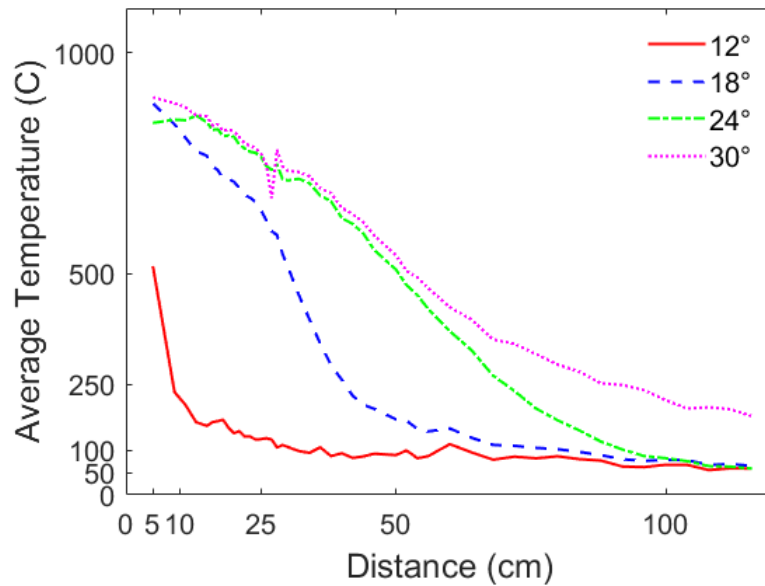


Figure 16: Average temperature Profiles recorded downstream of a 228 kW fire from a 15.24 cm × 183 cm burner

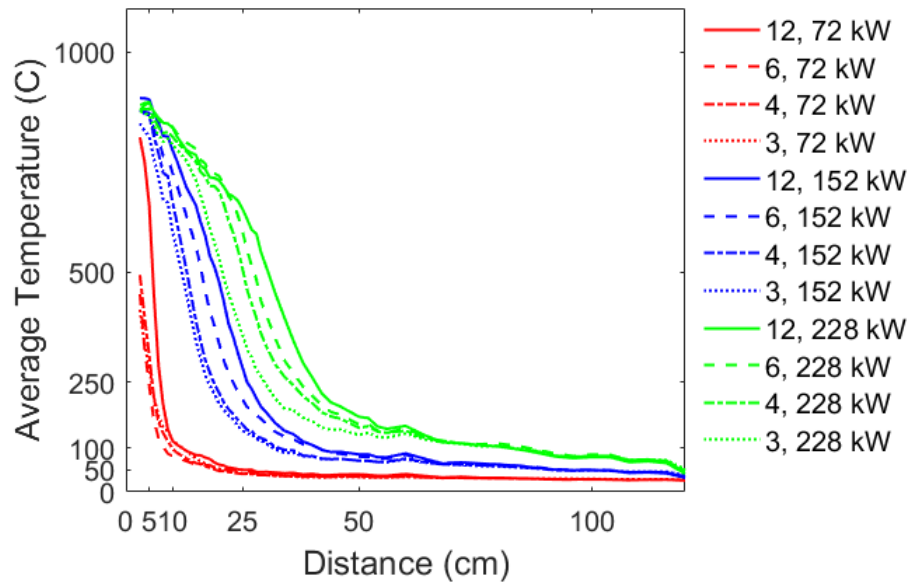


Figure 17: Average temperature profiles recorded downstream of 12 fires with varying heat-release rate per unit area on an 18° incline. Legend displays the aspect ratio, and the fire heat-release rate for each test.

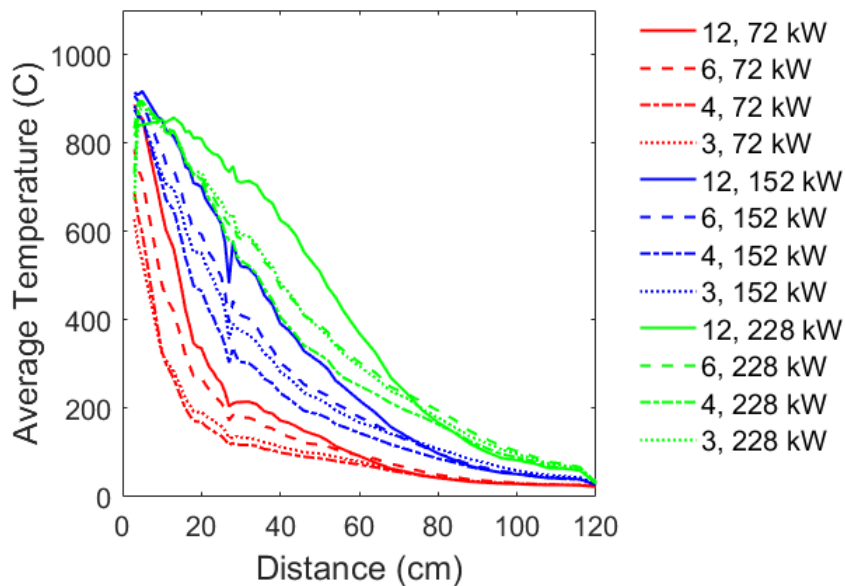


Figure 18: Average temperature profiles recorded downstream of 12 fires with varying heat-release rate per unit area on an 24° incline. Legend displays the aspect ratio, and the fire heat-release rate for each test.

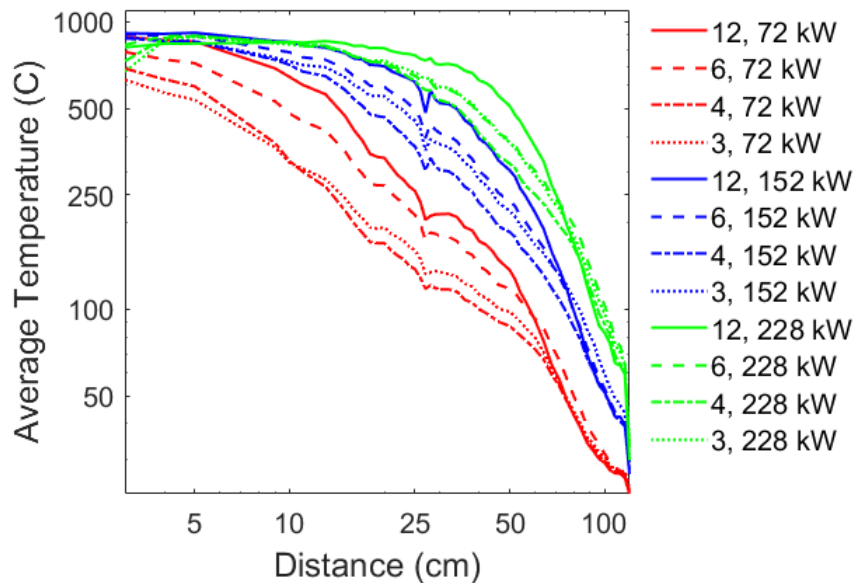


Figure 19: Average temperature profiles recorded downstream of 12 fires with varying heat-release rate per unit area on an 24° incline. Legend displays the aspect ratio, and the fire heat-release rate for each test.

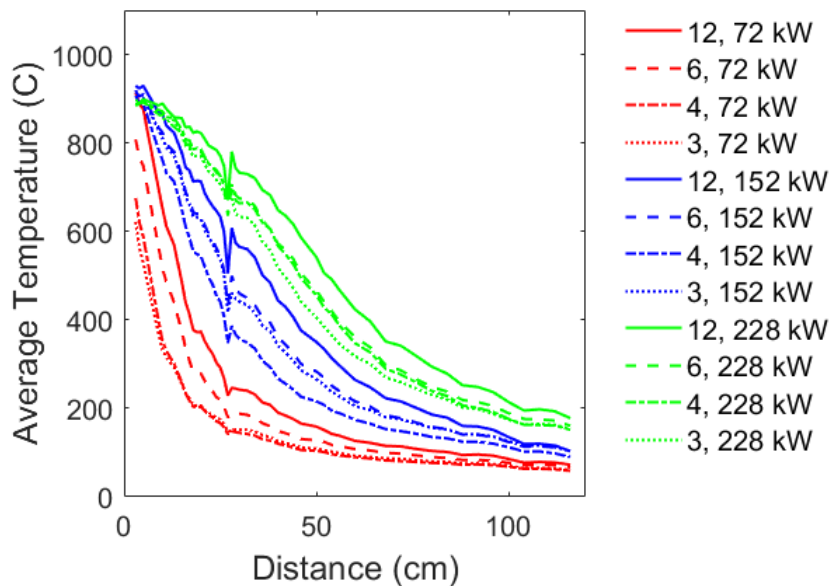


Figure 20: Average temperature profiles recorded downstream of 12 fires with varying heat-release rate per unit area on an 30° incline. Legend displays the aspect ratio, and the fire heat-release rate for each test.

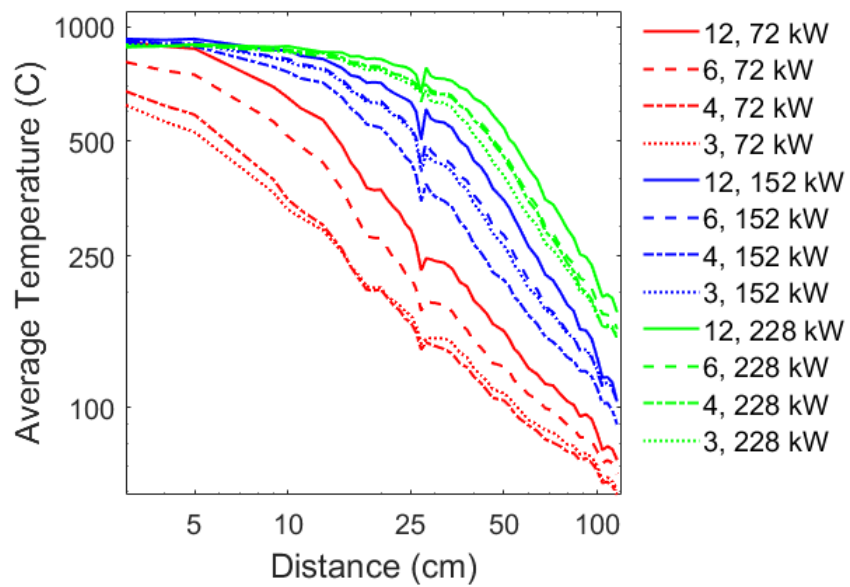


Figure 21: Average temperature profiles recorded downstream of 12 fires with varying heat-release rate per unit area on an 30° incline. Legend displays the aspect ratio, and the fire heat-release rate for each test.

A.4 Large Scale Average Temperature Profiles: Forced Flow

In this section, figures from the large-scale tilt table under the influence of forced flow alone are shown. Figures 22, 23, 24, and 25 contain heat-release rates of 76, 152 and 228 kW, forced flows from 0.304 m/s to 1.26 m/s, and have no inclination (0°).

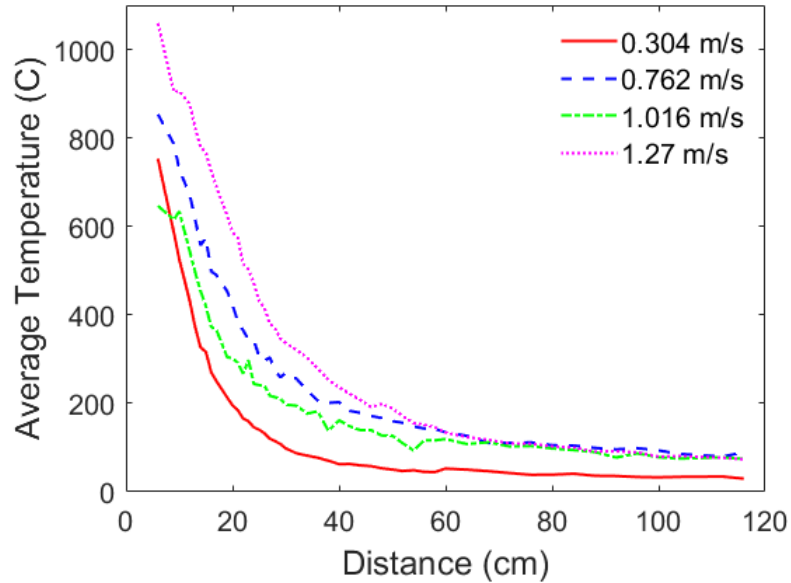


Figure 22: 152 kW fire from a 30.48 cm \times 183 cm burner with varying forced flow while at the horizontal (0°)

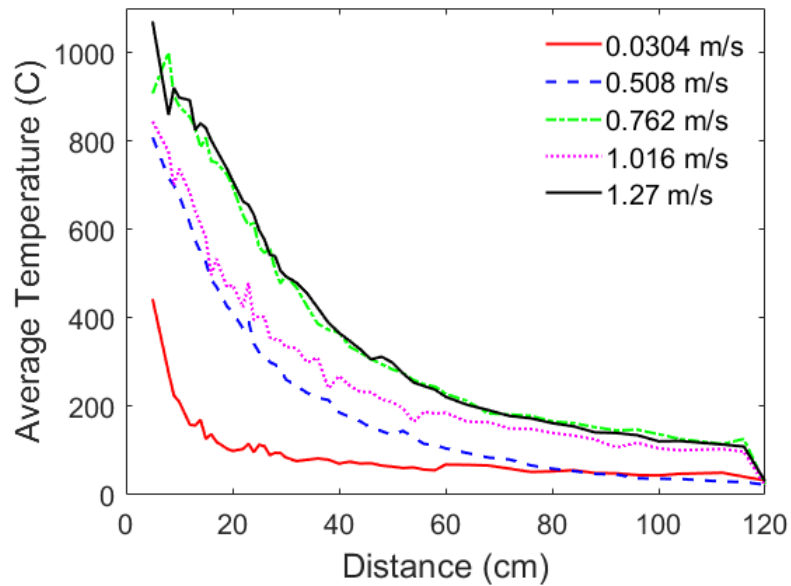


Figure 23: 228 kW fire from a 45.72 cm × 183 cm burner with varying forced flow while at the horizontal (0°)

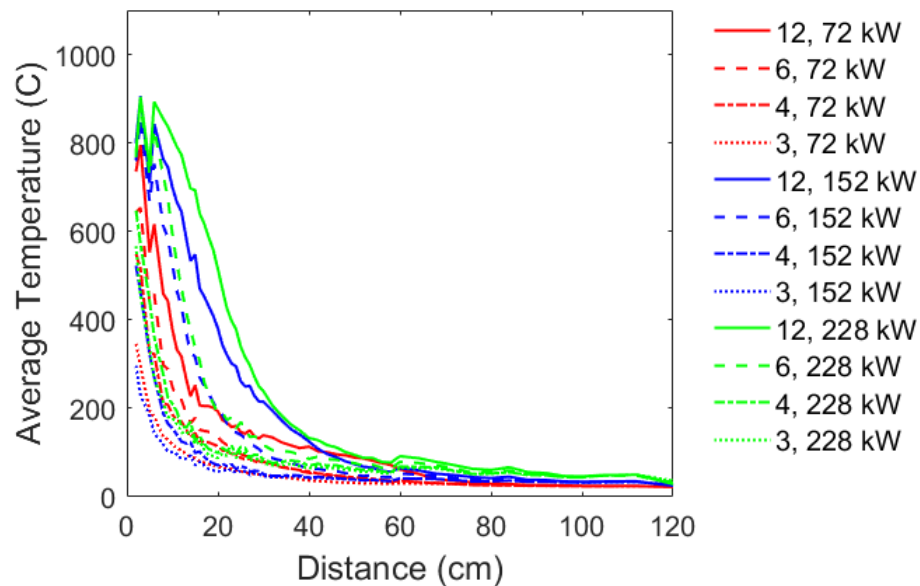


Figure 24: Temperature profiles for all aspect ratios and heat-release rates under the influence of a 0.304 m/s forced flow. Legend displays the aspect ratio, and the fire heat-release rate for each test.

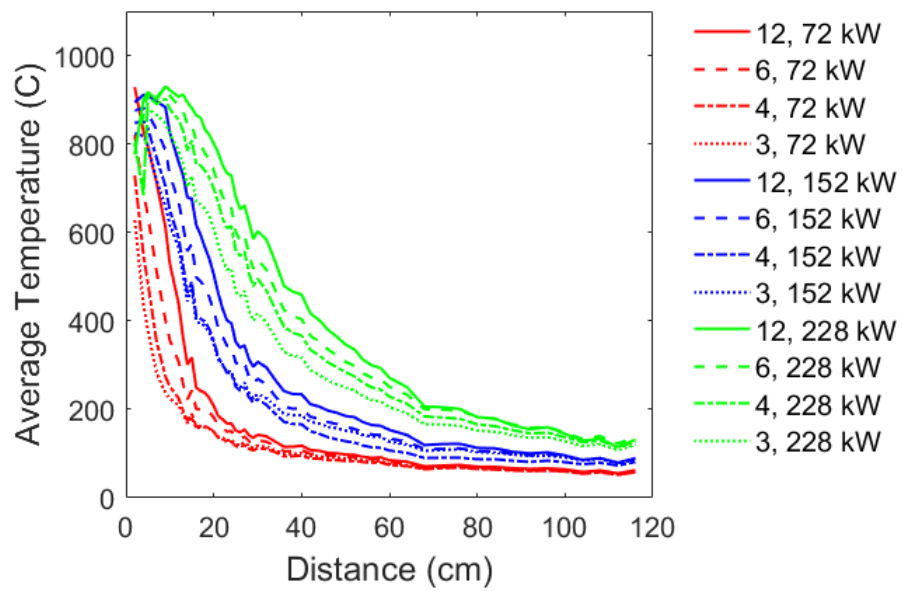


Figure 25: Temperature profiles for all aspect ratios and heat-release rates under the influence of a 0.762 m/s forced flow. Legend displays the aspect ratio, and the fire heat-release rate for each test.

A.5 Large Scale Average Temperature Profiles: Inclined and Forced Flow

In this section, figures from the large-scale tilt table under the influence of inclination and forced flow are shown. Figures 26, 27, 28, 29, 30, and 31 contain heat-release rates of 76, 152 and 228 kW, have inclination varying from 12° to 30° , and forced flows of 0.304 m/s and 0.762 m/s.

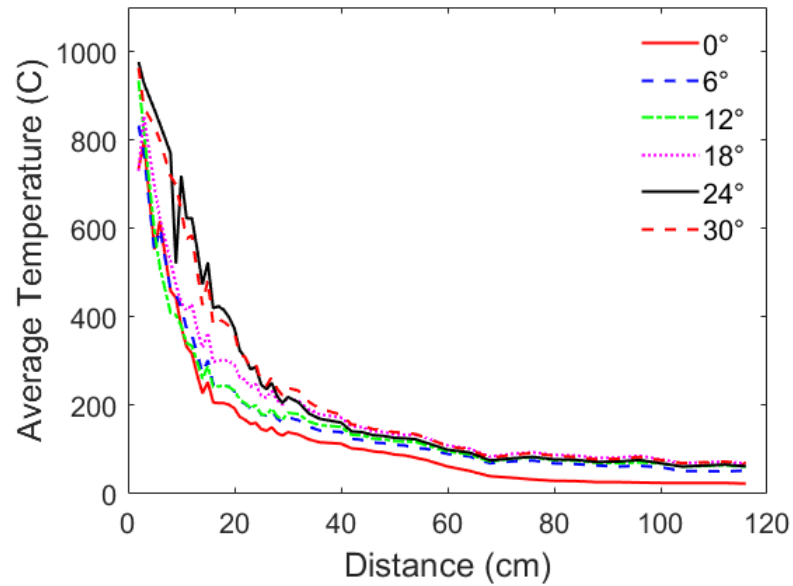


Figure 26: Average temperature profiles for a 72 kW fire with a 0.304 m/s forced flow and an aspect ratio of 12

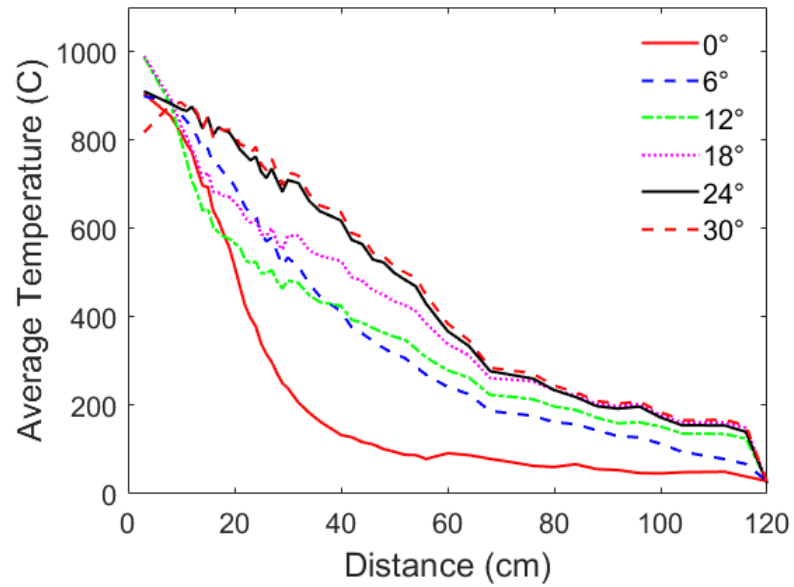


Figure 27: Average temperature profiles for a 228 kW fire with a 0.304 m/s forced flow and an aspect ratio of 12

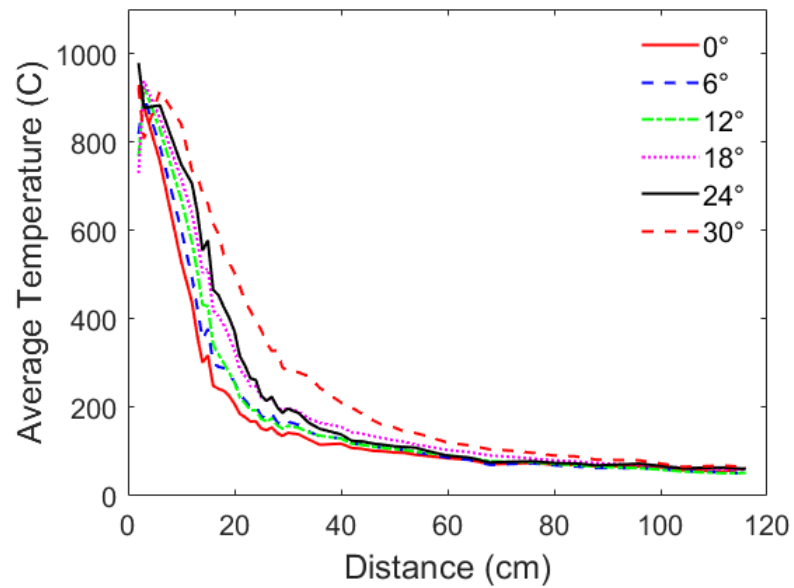


Figure 28: Average temperature profiles for a 72 kW fire with a 0.762 m/s forced flow and an aspect ratio of 12

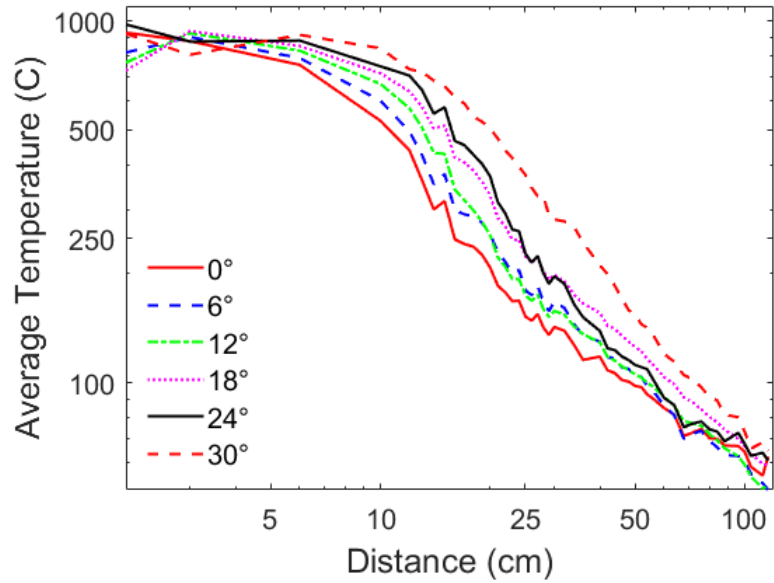


Figure 29: Average temperature profiles for a 72 kW fire with a 0.762 m/s forced flow and an aspect ratio of 12

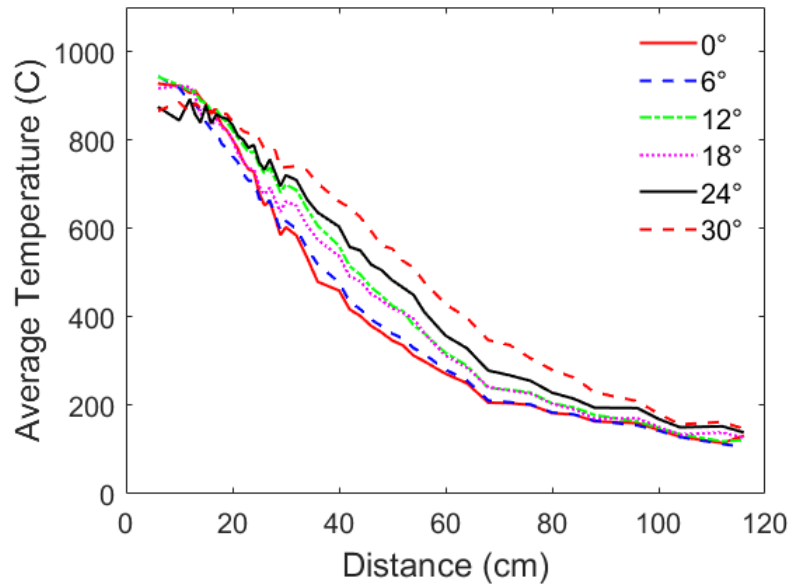


Figure 30: Average temperature profiles for a 228 kW fire with a 0.762 m/s forced flow and an aspect ratio of 12

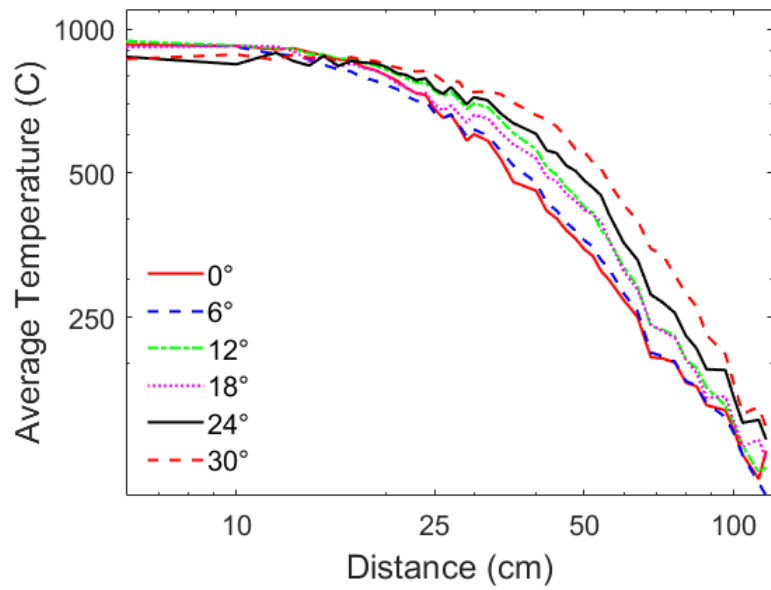


Figure 31: Average temperature profiles for a 228 kW fire with a 0.762 m/s forced flow and an aspect ratio of 12

Bibliography

- [1] National Interagency Coordination Center. Wildland Fire Summary and Statistics Annual Report 2017. National Interagency Coordination Center, Boise, Idaho. 2017.
- [2] United States Forest Service. The Rising Cost of Wildfire Operations, 2015. URL: <https://www.fs.fed.us/sites/default/files/2015-Fire-Budget-Report.pdf>
- [3] Finney, M.A., J. Forthofer, and I. Grenfell. A study of flame spread in engineered cardboard fuelbeds; Part I: Correlations and observations. In: Seventh International Symposium on Scale Modeling, 2013.
- [4] Sullivan, L.A. Wildland surface fire spread modelling, 1990-2007.2: Empirical and quasi-empirical models. *International Journal of Wildland fire*, 18(4) 369-386.
- [5] Finney, M.A., J.D. Cohen, J.M. Forthofer, S.S. McAllister, M.J. Gollner, D.J. Gorham, K. Saito, N.K. Akafuah, B.A. Adam, and J.D. English. Role of buoyant flame dynamics in wildfire spread. *Proceedings of the National Academy of Sciences*, 112(32):9833–9838, 2015.
- [6] Rothmel, R.C. A mathematical model for predicting fire spread in wildland fuels. *Res. Pap. INT-115. Ogden, UT: US Department of Agriculture, Intermountain Forest and Range Experiment Station. 40 p.*, 115, 1972.
- [7] Tang, W., C.H. Miller, M.J. Gollner, Local flame attachment and heat fluxes in wind-driven line fires. *Proceedings of the Combustion Institute*, 36(2):3253–3261, 2017.
- [8] Tang, W., M.A. Finney, S.S. McAllister, M.J. Gollner. An experimental study of intermittent heating frequencies from wind-driven flames. *Frontiers in Mechanical Engineering*, 5:34, 2019.
- [9] Tang, F., Q. He, and J. Wen. Effects of crosswind and burner aspect ratio on flame characteristics and flame base drag length of diffusion flames. *Combustion and Flame*, 200:265–275, 2019.

- [10] Grumstrup, T.P., S.S. McAllister, and M.A. Finney. Qualitative Flow Visualization of Flame Attachment on Slopes. In: 10th U.S. National Combustion Meeting, 2017.
- [11] Grumstrup, T.P., J.M. Forthofer, and M.A. Finney. Temperature Measurements of Attached Fire Plumes on a Slope. In: Eighth International Symposium on Scale Modeling, 2017.
- [12] Wu, Y., H.J. Xing, and G.T. Atkinson, Interaction of fire plume with inclined surface. *Fire Safety Journal*, 35(4): 391–403, 2000.
- [13] Atkinson, G.T., D.D. Drysdale, and Y. Wu. Fire driven flow in an inclined trench. *Fire Safety Journal*, 25(2):141–145, 1995.
- [14] Drysdale, D.D., and A.J.R Macmillan. Flame spread on inclined surfaces. *Fire Safety Journal*, 18(3):245–254, 1992.
- [15] Gollner, M.J., C.H. Miller, W. Tang, and A.V. Singh. The effect of flow and geometry on concurrent flame spread. *Fire Safety Journal*, 91:68–78, 2017.
- [16] Dold, J.W. Flow attachment in eruptive fire growth. In: Proceedings of the 6th International Conference on Forest Fire Research, 2010.
- [17] Viegas, D.X., and A. Simeoni. Eruptive behavior of forest fires. *Fire Technology*, 47(2): 303–320, 2011
- [18] Cohen, J.D., Fuel particle heat exchange during wildland fire spread. PhD Dissertation. University of Idaho. 2015.
- [19] Williams, F.A. Mechanisms of fire spread. In: Symposium (International) on Combustion. 16:1281–1294, 1977.
- [20] Morandini, F., X. Silvani, D. Honore, B. Guillaume, A. Susset, and R. Vernet. Slope effects on the fluid dynamics of a fire spreading across a fuel bed: PIV measurements and OH* chemiluminescence imaging. *Experiments in fluids*, 55(8):1788, 2014.
- [21] Sharples, J.J., M.A. Gill, and J.W. Dold. The trench effect and eruptive wildfires: lessons from the king’s cross underground disaster. In: Proceedings of Australian Fire and Emergency Service Authorities Council Conference, 2010.
- [22] Dold, J.W., and A. Zinoviev. Fire eruption through intensity and spread rate interaction mediated by flow attachment. *Combustion Theory and Modeling*, 13(5):763–793, 2009.
- [23] Viegas, D.X. A mathematical model for forest fires blowup. *Combustion Science and Technology*, 177(1):27–51, 2004.
- [24] Viegas, D.X. and A. Simeoni. Eruptive behavior of forest fires. *Fire Technology*, 47(2):303–320, 2010.

- [25] Gollner, M.J., X. Huang, J. Cobian, A.S. Rangwala, and F.A. Williams. Experimental study of upward spread of an inclined fuel surface. *Proceedings of the Combustion Institute*, 34(2):2531–2538, 2013.
- [26] Pizzo, Y., J.L. Consalvi, and B. Porterie. A transient pyrolysis model based on the b-number for gravity-assisted flame spread over thick pmma slabs. *Combustion and flame*, 156(9):1856–1859, 2009.
- [27] Xie, W. and P. DesJardin. An embedded upward flame spread model using 2D direct numerical simulations. *Combustion and Flame*, 156(2):522–530, 2009.
- [28] Fernandez-Pello, A.C., and T. Hirano. Controlling mechanisms of flame spread. *Combustion Science and Technology*, 32(1-4):1–31, 1983.
- [29] Ahmad, T., G. Faeth, Turbulent wall fires. In: Symposium (International) on Combustion, 17:1149–1160, 1979.
- [30] Delichatsios, M.A. Flame heights in turbulent wall fires with significant flame radiation. *Combustion Science and Technology*, 39(1-6):195–214, 1984.
- [31] Coutin, M., J.M. Most, M.A. Delichatsios, and M.M. Delichatsios. Flame heights in wall fires: effects of width, confinement and pyrolysis length. *Fire Safety Science*, 6:729–740, 2000.
- [32] Mao, C.P., A.C. Fernandez-Pello, and P.J. Pagi. Mixed convective burning of a fuel surface with arbitrary inclination. *Journal of heat transfer*, 106(2):304–309, 1984.
- [33] Singh, A.V., and M.J. Gollner. Local burning rates and heat flux for forced flow boundary-layer diffusion flames. *AIAA Journal*, 54(2):408–418, 2015.
- [34] Singh, A.V., and M.J. Gollner. Steady and transient pyrolysis of a non-charring solid fuel under forced flow. *Proceedings of the Combustion Institute*, 36(2):3157–3165, 2017.
- [35] Hirano, H. and M. Kinoshita. Gas velocity and temperature profiles of a diffusion flame stabilized in the stream over liquid fuel. In: Symposium (International) on Combustion. 15:379–387, 1975.
- [36] Loh, H.T. and A.C. Fernandez-Pello. A study of the controlling mechanisms of flow assisted flame spread. In: Symposium (international) on combustion. 20:1575–1582, 1985.
- [37] Hargather, M.J. and G.S. Settles. Retroreflective shadowgraph technique for large-scale flow visualization. *Applied optics*, 48(22):4449–4457, 2009.
- [38] Omega Engineering. Thermocouple response time, 2019 URL:<https://www.omega.com/en-us/resources/thermocouples-response-time>. Accessed: 2019-06-27.

- [39] Viegas, D.X., A. Simeoni, G. Xanthopoulos, C. Rossa, L.M. Ribeiro, L.P. Pita, D. Stipanicev, A. Zinoviev, R. Weber, and J. Dold et al. Recent forest fire related accidents in Europe. *Office for Official Publications of the European Communities*, 2009.
- [40] Quintiere, J.G. Scaling applications in fire research. *Fire Safety Journal*, 15:3–29, 1989.
- [41] Finney, M.A., J.D. Cohen, S.S. McAllister, and W.M. Jolly. On the need for a theory of wildland fire spread. *International Journal of Wildland Fire*, 22(1):25, 2013.
- [42] Quintiere, J.G. The effects of angular orientation on flame spread over thin materials. *Fire Safety Journal*, 36:291–312, 2001.
- [43] Nelson, R.M. Byram’s Derivation of the Energy Criterion for Forest and Wildland Fires. *International Journal of Wildland Fire*, 3(3):131–138, 1993.
- [44] Rothmel, R.C. Crown fire analysis and interpretation. *Proceedings of the Society of American Foresters National Convention (USA)*, 1991.
- [45] Sullivan, A.L. Convective Froude number and Byram’s energy criterion of Australian experimental grassland fires. *Proceedings of the Combustion Institute*, 31(2):2557–2564, 2007.